Design and construction of a transportable quantum gravimeter and realization of an atom-chip magnetic trap

---

Von der Fakultät für Mathematik und Physik
der Gottfried Wilhelm Leibniz Universität Hannover

zur Erlangung des Grades
Doktor der Naturwissenschaften
- Dr. rer. nat-
genehmigte Dissertation von
M.Sc. Maral Sahelgozin

2019

Referent: Prof. Dr. Ernst M. Rasel

Korreferent: Dr. Dennis Schlippert

Korreferent: Assoc. Prof. Dr. Rainer H. Dumke

Tag der Disputation: 18.06.2019

Abstract

The quantum gravimeter QG-1 is designed to perform local gravity measurements in field with residual uncertainties surpassing state-of-the-art absolute gravimeters. It will use delta-kick collimated Bose-Einstein condensates (BEC) of ^{87}Rb atoms as the source for matter-wave interferometry and aims for an uncertainty level below $3\,\mathrm{nm/s^2}$ with a repetition rate of $0.5\,\mathrm{Hz}$.

In the frame of this thesis, the atom-chip source has been set up and characterized. In order to meet the requirements for transportability, the apparatus needs to be compact and robust. Additionally, a high BEC flux is desired for the targeted statistical uncertainty. To meet these requirements a double magneto-optical trap (MOT) configuration based on a 3-layer atom chip has been implemented. Furthermore, a compact high power fiber-based laser system has been developed to provide the light for atomic manipulation. To power and control this laser system and generate the magnetic fields necessary to trap atoms, a miniaturized electronic system with low power consumption has been utilized and characterized.

The steps towards trapping the atoms inside a magnetic trap on which the evaporation will be implemented have been realized and optimized. A two-dimensional MOT has been employed and an optimized atomic beam flux of $2.2 \times 10^9\,\mathrm{atoms/s}$ with a mean longitudinal velocity of $17.2\,\mathrm{m/s}$ and a narrow longitudinal velocity distribution of $2.2\,\mathrm{m/s}$ has been used to load a 3D-chip MOT. The resulting 3D-MOT has been characterized and a loading rate of $8.1 \times 10^8\,\mathrm{atoms/s}$ has been attained. After loading for $300\,\mathrm{ms}$, 2.4×10^8 atoms are trapped in the 3D-MOT. Applying a subsequent compressed MOT stage, the cloud density has been increased by a factor of 10. This denser atomic ensemble with $2.9 \times 10^{10}\,\mathrm{atoms/cm^3}$ has been further cooled in a polarization gradient cooling (PGC) stage to $5.6\,\mu\mathrm{K}$ in order to increase the mode match with the subsequent magnetic trap. In the initial large volume magnetic trap generated by the wire structures on the mesoscopic and the base layers of the atom-chip assembly, 3.6×10^7 atoms have been captured. This trap features a temperature of $44.3\,\mu\mathrm{K}$, a trapping frequency of $9.1\,\mathrm{Hz}$ in its weak confining axis and a phase-space density of 4.5×10^{-7}. The process of transferring the atoms into the final magnetic trap with higher trapping frequency for an efficient BEC evaporation, which is formed by the wire structures on the base and science chip has been tested. With this, all the necessary functionalities of a high-flux BEC source setup have been demonstrated.

Keywords: gravimetry, Bose-Einstein condensates, atom chip

Contents

CHAPTER 1

Introduction

Absolute measurements of the gravitational acceleration have a variety of applications, including the test of the universality of free fall [1–5] or geophysical applications [6–8]. The interest in understanding the temporal and spatial mass variations of the Earth, demands absolute gravity measurements. Beside satellite-based missions [9], this requires mobile devices, which are able to perform measurements at geophysically interesting sites. Parallel research in different groups has been performed to push the limits of portable gravimeters. The highest sensitivity for gravity measurements, is achieved by a superconducting gravimeter (GWR Instruments) [10]. Its principle of operation is similar to a spring gravimeter [11]. Here, the spring is replaced by a superconducting niobium sphere levitating in the magnetic field of two superconducting coils. The change in the gravitational force is measured from the changes in the coils' current trying to keep the position of the test mass constant. The superconductive gravimeter iGrav SG, which is also transportable, can measure gravity with a noise level of $3\,\mathrm{nm/s^2}$ in 1 s with a drift of less than $5\,\mathrm{nm/s^2}$ per month[1] [10]. This gravimeter is however a relative device[2], which requires to be calibrated in comparison to an absolute gravimeter to know the absolute value of gravitational acceleration. A mobile gravimeter, which can perform absolute gravity measurements is the FG5-X (MicroG Lacoste) and works based on optical interferometry [13]. The position of a falling corner cube is measured by a Mach-Zehnder interferometer formed by this free-falling corner cube, a beam splitter and a stationary corner cube, all positioned inside a vacuum chamber. The lower corner cube acts as the reference mirror for the intereferometer and is isolated against vibrations. This gravimeter can perform absolute gravity measurements with an uncertainty of $20\,\mathrm{nm/s^2}$ and a short-term instability of $150\,\mathrm{nm/s^2}$ in 1 s at a quiet site[3] [14]. However, classical absolute gravimeters, like FG5-X suffer from wear after each drop, since they contain moving mechanical parts.

Rapid development in quantum optics in the last decades paved the way for instruments relying on the principle of matter-wave interferometry [15–17]. A three-pulse atom interferometer analogous to an optical Mach-Zehnder interferometer acting on a sample of cold atoms is used to coherently split, redirect and recombine the atomic cloud. The gravitational acceleration is measured from the phase difference experienced by the two

1 This is specified as a noise level of $0.3\,\mu\mathrm{Gal}/\sqrt{\mathrm{Hz}}$ with a drift below $0.5\,\mu\mathrm{Gal/month}$ by the company [10]. The Gal is a unit of acceleration used widely in the geodetic community and is defined as $1\,\mathrm{Gal} = 1\,\mathrm{cm/s^2}$.

2 Relative gravimeters measure variation of gravity from place to place [12].

3 This is stated as an accuracy of $2\,\mu\mathrm{Gal}$ and a precision of $15\,\mu\mathrm{Gal}/\sqrt{\mathrm{Hz}}$ at a quite site in the datasheet of the apparatus [13].

arms of the intereferometer [15]. Because the mechanical components are eliminated, these gravimeters can operate with higher cycling rates and don't suffer from wear. With this, cold atom gravimeters can perform quasi-continuous drift-free measurements even at noisy sites. The first measurement of tides based on matter-wave interferometry was performed in 1999 in a laboratory setting [18]. Afterwards, further ongoing work in various groups has been performed trying to push the limit in the sensitivity and accuracy of these sensors as well as extending them to use outside of the laboratory. State-of-the-art mobile atom gravimeters include the gravimetric atom interferometer (GAIN) developed at Humboldt Universität zu Berlin [19, 20] and the cold atom gravimeter (CAG) set up at LNE-SYRTE Observatoire de Paris [21]. The former is a transportable fountain gravimeter, which has reported absolute values with systematic uncertainties of $32\,\mathrm{nm/s^2}$ and a long-term instability of $0.5\,\mathrm{nm/s^2}$ in $10^5\,\mathrm{s}$ [19]. The latter has reported an uncertainty level of $43\,\mathrm{nm/s^2}$ [21] and a long-term instability of $0.2\,\mathrm{nm/s^2}$ in less than 2000 s in the quiet site [22]. Another mobile atom gravimeter, which is a simplified system by using only one laser for cooling and manipulation of the atoms [23], is the absolute quantum gravimeter (AQG, Muquans) [24]. The company has stated a short-term instability of $500\,\mathrm{nm/s^2}$ in 1 s and a long-term instability of $10\,\mathrm{nm/s^2}$. The uncertainty of the device has not yet been stated [24].

The accuracy of these atom gravimeters is mainly limited by two sources of systematic effects, namely the Coriolis acceleration and the wavefront distortion of the interferometer light pulse [19, 21, 23]. These effects stem from horizontal velocity components of atoms during the free fall, which is a result of the poor control on the starting properties and the expansion rate of the atomic ensemble due to its finite temperature. A non-zero horizontal component in the initial mean velocity of the atoms, leads to a spatial area in between the interferometer arms, which makes the interferometer sensitive to rotations due to the Sagnac effect. This Coriolis phase shift leads to a bias in the gravity measurement [25, 26]. To mitigate this effect, in CAG, the bias caused by the Coriolis force is estimated by performing two measurements for two orientations of the experiment, which differ by 180° around the vertical axis. The Coriolis acceleration in these two configurations has the same amplitude and opposite signs and therefore can be calculated from half the difference of these signals [25]. In GAIN, the Coriolis effect is compensated by rotating the reference mirror counter to the Earth's rotation [27]. The bias due to wavefront distortion arises due to aberrations in the wavefront of the interferometer light, which are not common in both of the counter-propagating beams. Therefore, this bias is mainly caused as a result of a poor surface quality of the retro-reflecting mirror. In an uneven differential wavefront, the interferometer phase experienced by each atom depends on its position. Atoms in an expanding cloud will sample different parts of the wavefront during each of the three interferometer pulses. This leads to a phase shift inducing systematic errors in the gravity measurement [25, 28]. To mitigate the wavefront bias, in CAG, the reference mirror is placed inside the vacuum chamber. With this, the requirement of a view port in the path of the interferomter beam is eliminated, leading to a better differential wavefront quality [25]. A correction for the residual wavefront distortions is implemented by measuring gravity with different cloud temperatures and extrapolating the measurements to $0\,\mu\mathrm{K}$ using a numerical model [29]. In GAIN, the wavefront distortion is reduced by post-correcting the measured deformation from the optical elements [28].

Nevertheless, the bias due to wavefront aberrations and Coriolis acceleration are yet introducing the largest systematic uncertainty in atom gravimeters. These effects can be reduced using a non-expanding ensemble, such as Bose-Einstein condensates (BEC) as the source for the interferometer [29, 30]. BECs were experimentally observed in 1995 [31–33]. Because of their high degree of coherence, interference experiments with BECs were performed shortly afterwards [34, 35]. By applying delta-kick collimation (DKC), the velocity spread of these atomic samples, and thus their expansion rate, can be further reduced [36, 37]. The very low expansion rate of a delta-kick collimated BEC helps in the reduction of both aforementioned sources of systematics.

The versatile magnetic fields required for the generation of a BEC, often makes BEC machines bulky, which does not suit a mobile device. Transportability of an apparatus demands lowering its weight, size and power consumption. During recent years, several experiments have been performed trying to miniaturize the structures that generate magnetic field gradients. These efforts led to experiments producing BECs on a so-called atom chip [38–40]. In an atom-chip-based BEC machine, the magnetic fields for manipulation of the atoms are produced by current carrying wires microfabricated on a substrate. This considerably reduces the size and power consumption of the experiment. An atom chip can be mounted inside the vacuum chamber in close distance to the atoms and has a lower inductance in comparison to electromagnetic coils due to its smaller structure size. This reduces the switching time of the structures and a faster BEC production rate can be obtained. Additionally, the use of atom-chip-based BECs offers a good control over the initial position and velocity of the atoms before their free fall. Hence employing a delta-kick collimated BEC produced on an atom chip as the source for atom interferometry makes the bias introduced from both the wavefront aberration and the Coriolis acceleration negligible.

This thesis

The focus of this thesis is on the construction of the atomic source for the interferometry in an absolute quantum gravimeter, QG-1, at the Institut für Quantenoptik (IQ) at the Leibniz Universität Hannover (LUH). The goal of this apparatus is to measure the gravitational acceleration in field with an unprecedented uncertainty. It will be used for gravity measurements in geodetic campaigns to study effects arising from the mass transport mechanism in the Earth to refine the Earth's gravity model or to monitor temporal gravity variations and verify dynamic Earth models. One example operation of QG-1 is in the Fennoscandian land uplift area. The amount of the gravity change in this area is $10\,\mathrm{nm/s^2}$ per year [41]. For the observation of the land uplift, a reproducible absolute gravimetry with an inaccuracy below this level is required. QG-1 aims to perform drift-free long-term absolute gravity measurements in field with an uncertainty below $3\,\mathrm{nm/s^2}$ and a repetition rate of 0.5 Hz. The design and setup of the apparatus has been started during the work of this thesis. The focus of this thesis is on the production of a 3-layer atom-chip assembly, the setup of a compact and stable laser system for the cooling and manipulation of the atoms and the experimental realization of trapping the atoms in a magnetic trap generated on the atom chip.

Chapter 2 provides a short introduction on how the gravitational acceleration is mea-

sured using matter-wave interferometry and how to lower the uncertainty level in such measurements using a high-flux BEC source for the interferometer. Afterwards, a brief overview on the requirements for an experimental realization of such a BEC is provided.

The design and development of the experimental apparatus of QG-1 is discussed in chapter 3. The chapter is divided into two parts. The first part deals with the sensor head, in which the cooling and trapping of the atoms have been performed and gravity measurements will be carried out. This part includes the vacuum chamber, the 3-layer atom chip and the magnetic coils. The second part of this chapter covers the laser system and the driving electronics. For each of these components, the design concerns to fulfill the requirements for generation of a high-flux BEC source in an accurate portable gravimeter is discussed and the results of the characterization and optimization of each of these components are presented.

The detection system used in the experiment and its characterizations are presented in chapter 4.

Chapter 5 delineates the experimental realization and optimization of each cooling and trapping step starting with the creation of a high-flux $2D^+$-atomic beam from the background rubidium gas. It further describes the process of cooling and trapping of these atoms in a 3D-chip MOT in the experiment chamber and follows with the compression of the atomic ensemble and it's sub-Doppler cooling in a polarization gradient cooling stage. The chapter ends with the trapped atoms in a magnetic trap generated on the atom-chip assembly. The characterization procedure of each of these steps and the resulting functionalities are discussed.

A short outlook towards quantum degeneracy and future plans for the experiment are provided in chapter 6.

CHAPTER 2

Accurate gravity measurement in a compact setup

2.1 Gravimetry using atom interferometry

Atom gravimeters employ the interferometry based on matter-waves [42, 43]. Light pulses are used to put all atoms in an ensemble into a quantum superposition of two distinct states, which will follow two spatially separated paths and then will be brought back together to interfere. The resulting interference pattern depends on the difference in the phase accumulated along the two paths, which is influenced by forces acting on the atoms during this interrogation time. This makes the interferometer sensitive to accelerations and a proper tool for inertial sensing.

The most common interferometry scheme used for the measurement of the gravitational acceleration is similar to the Mach-Zehnder interferometer in optics. The sequence of this three-pulse, $\pi/2$-π-$\pi/2$[1], interferometer is depicted in fig. 2.1. Initially, the atoms are prepared in a narrow velocity distribution in their ground state, illustrated as $|1>$ in the diagram. The first $\pi/2$-pulse at time t_1 splits the atomic wave packets into an equal superposition of their two internal states, while transferring the photon momentum to one part of the superposition. At time $t_2 = t_1 + \tau/2 + T$ the π-pulse is applied to redirect the trajectory of the atoms. Here, τ is the length of a π-pulse and T is the free evolution time in between of the two subsequent pulses. Finally, at time $t_3 = t_1 + 3\tau/2 + 2T$ the final $\pi/2$-pulse will superimpose both paths. Assuming a uniform gravitational field along the interferometer path and a perfect overlap of the outputs of the two ports, the difference in the accumulated phases along each of the two interferometer paths includes only the laser phase imprinted during the pulses and can be written as

$$\Delta\Phi = \phi(t_1) - 2\phi(t_2) + \phi(t_3) \tag{2.1}$$

where $\phi(t_i), i = 1,2,3$ is the imprinted laser phase to the atomic wave function at each of the pulses [46]. The interferometry beams and therefore the wave vectors of the beams are

1 Considering a simple system of a two-level atom coupled by a near-resonant light field, the Rabi frequency Ω is a measure of the coupling strength in between of the two states. Hence, the interaction time determines the population probability. A pulse with a length of $\tau = \pi/\Omega$ coupled with the atom is called a π-pulse. It acts analogous to a mirror for the atom and flips (reflects) the initial atomic state. A $\pi/2$-pulse is therefore, a pulse with a length of $\tau = \pi/2\Omega$ and will transfer an atom starting in one of the two states into a superposition of the states with an equal amplitude probability, acting analogous to a beam splitter for the atom. For a complete description on the atom-field coupling refer to [44].

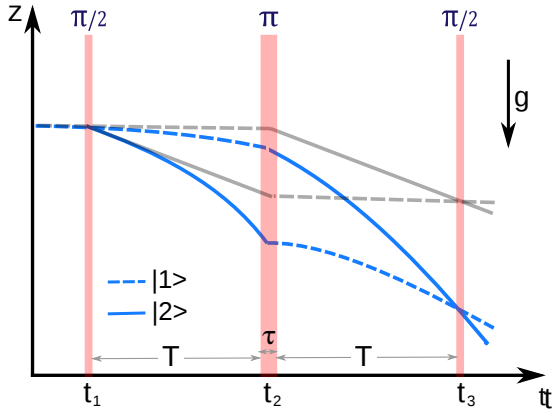

Figure 2.1: Space-time diagram of a Mach-Zehnder atom interferometer in the absence (gray lines) and presence (blue lines) of a uniform gravitational acceleration. A sequence of three pulses $\pi/2$-π-$\pi/2$ at times t_1, t_2 and t_3 with a separation time T in between of the two subsequent pulses are used to split, mirror and recombine the atomic wave functions. The interferometer phase shift can be deduced from the population measurement of the two atomic states at the end of the sequence (eq. (2.3)). τ is the pulse-length of a π-pulse. This image is inspired by [45].

parallel to the gravitational acceleration $\vec{g}$. The interferometer phase induced by a uniform gravitational field is described as

$$\Delta\Phi = -\vec{k}_{eff} \cdot \vec{g} T^2 \tag{2.2}$$

where $\vec{k}_{eff} = \vec{k}_1 - \vec{k}_2$ is the effective wave vector of the light, which is equal to $k_{eff} = k_1 + k_2$ for the counter-propagating beams [46].

This interferometer phase shift can be deduced from a measurement of the number of atoms in each of the two atomic states after the interferometry time. The probability of detecting the atoms in the excited state $|2>$ oscillates with the interferometer phase as

$$P_{|2>}(\Phi) = \frac{1}{2}(1 + C\cos\Delta\Phi) \tag{2.3}$$

where C is the fringe contrast of the interferometer [15]. By introducing a frequency chirp α to the interferometry beams, the interferometer output is modulated as

$$\Delta\Phi = (\vec{k}_{eff} \cdot \vec{g} - \alpha) T^2. \tag{2.4}$$

The chirp rate $\alpha/\vec{k}_{eff}$ can be adjusted to compensate the Doppler shift induced by the gravitational acceleration $\vec{g}$ to ensure the resonance of the interferometry pulses with the

atomic transition. At this point, the interferometry phase $\Delta\Phi = 0$ for all values of the pulse separation time T. From this, the value of $\vec{g}$ can be obtained.

2.2 Gravimetry with low uncertainty in a transportable device

As the input for an atom interferometer, a coherent atomic ensemble is required. Typically, experiments are using molasses cooled atomic clouds [19, 23]. As described in chapter 1, using magnetically lensed BECs as the source for interferometry reduces the bias due to the wavefront aberration and the Coriolis effect, which lowers the systematic uncertainty in the measured gravity signal.

The noise in the measured value of the excitation probability of the atoms (eq. (2.3)) is fundamentally limited by the quantum projection noise (QPN), given by

$$\sigma_{P_{|2>}} = \sqrt{\frac{P_{|2>}(1 - P_{|2>})}{N}} \tag{2.5}$$

where N is the number of particles in the atomic sample [47]. This limits the accuracy that can be reached in the measured value of g. Averaging the measured values in a certain time helps to lower the noise floor. Therefore, besides a low systematic uncertainty, a high stability of the interferometer is also essential to allow long-term and drift-free measurements to reach the anticipated statistical uncertainty within a feasible averaging time. The stability of the interferometer is often described by the Allan standard deviation [48]. Assuming a white noise of the interferometer, it can be derived from eq. (2.3) as

$$\sigma_{\Phi}(T_{ave}) = \frac{1}{C\sqrt{N}k_{eff}T^2}\sqrt{\frac{T_c}{T_{ave}}} \tag{2.6}$$

where T_c is the cycle time and T_{ave} is the total averaging time [49, 50]. During a long measurement time of the gravitational acceleration using an interferometer, the value of $\vec{g}$ itself is varying due to Earth tides, atmospheric and hydrologic conditions or other environmental effects. Therefore, to characterize the stability of a gravimeter, these temporal variations need to be subtracted from the measured gravity signal. For this purpose, a simultaneous measurement and comparison to a superconducting gravimeter can be performed as it is proposed in [19].

Equation 2.6 shows that the statistical uncertainty in the gravity measurement can be reduced by improving the number of atoms in the ensemble, lowering the cycle time, increasing the momentum transfer to the atoms during the atom-light interaction or elongating the time that atoms spend in the interferometer. Atom chips enable robust trapping of high number of atoms and rapid evaporations in a miniaturized setup and thus are suitable tools for portable high-flux BEC machines. In order to increase the momentum transfer during the atomic manipulation in QG-1, higher-order Bragg-type beam splitters will be employed for the interferometry. An interferometry chamber with a total length of 320 mm is chosen to compromise between a long interferometry time and the compact size of the setup. This provides a maximum total interferometry time of 250 ms, which can yet be further elongated using launching mechanism similar to [27, 51].

2.3 Experimental realization of a high-flux BEC in a compact device

During the time it takes to generate a BEC, the atoms need to be shielded from the environment. This requires the experiment to operate under ultra-high vacuum (UHV) conditions to prevent the loss of atoms due to the collisions with any background gas during the cycle time. Once the UHV condition is achieved, the first step involves getting a high flux source of atoms into this chamber. This can be done through several techniques such as using Zeeman slowers [52], direct loading from the background vapor provided by dispensers [45] or using an atomic beam loaded from a two-dimensional magneto-optical trap (MOT) [53]. Zeeman slowers tend to be bulky, while direct loading would reduce the vacuum quality, lowering the final atom number in the BEC. Thus these techniques are inadequate to be adopted in a portable high-flux BEC-machine. Therefore, the 2D-MOT technique is employed in the QG-1 setup, cause it enables loading of a high number of atoms very quickly while keeping the good vacuum quality in the experiment chamber. Furthermore, a 2D-MOT can be designed relatively compact. In the QG-1 experiment, the Rubidium atoms are provided by an ampule connected to the 2D-chamber. To trap and cool the generated high flux atomic beam, a 3D-MOT is utilized. Using an integrated mirror-MOT setup [54] eliminates the need for quadrupole coils and reduces the number of required light beams, helping in the miniaturization of the setup. Such an integrated 3D-MOT can be created using a U-shaped current-carrying wire implemented on an atom chip together with an external homogeneous magnetic field generated by a pair of Helmholtz coils outside the vacuum chamber [55]. Since the capture velocity of such a 3D-chip-MOT is relatively low, the injected atomic beam into the 3D-chamber requires to be additionally pre-cooled in its longitudinal axis. This is implemented by adding a molasses cooling in the axial direction using a pair of laser beams. This extended 2D-MOT setup is referred to as a $2D^+$-MOT [56, 57].

Cooling the atoms inside a MOT is limited by the Doppler limit, which is typically in the range of several hundred μK. The density of the atomic cloud is limited by the radiation pressure from the rescattered photons and does not suffice for the generation of a BEC [58]. Therefore, these cooled atoms are afterwards loaded into a magnetic trap, which can trap the atoms in the absence of light fields, breaking the limit on density imposed by light assisted collisions. High transfer efficiencies of the atoms from the laser cooled atomic cloud to the subsequent magnetic trap requires a good mode match, meaning that a well spatial and energy overlap should be realized. The size of the atomic cloud in the 3D-MOT is large and its temperature is high, leading to a poor mode match to the small volume of the magnetic trap generated from the wire structures on an atom chip. To overcome this problem, first the density of the atomic cloud is raised in a compressed MOT (cMOT) stage [59]. The temperature of the cloud is subsequently reduced to sub-Doppler temperatures by polarization gradient cooling (PGC) in the absence of magnetic fields[60]. Afterwards, this cold atomic cloud is transferred to the magnetic trap.

Confinement of neutral atoms in a magnetic trap is possible as a consequence of the interaction of their magnetic dipole moment $\vec{\mu}_{atom}$ with an inhomogeneous external magnetic field $\vec{B}$, which causes the atoms to experience a force with the strength of $\vec{F} = \vec{\nabla}(\vec{\mu}_{atom} \cdot \vec{B})$ [58]. In the presence of an external magnetic field, the degeneracy of the atomic energy

levels with a non-zero total angular momentum breaks due to the Zeeman effect. In a weak magnetic field, the energy shift can be written as $\Delta E_{|\mathrm{F},m_F>} = m_F g_F \mu_B B$. Here, m_F is the magnetic quantum number, g_F is the Lande-g-factor, equal to $+1/2$ for the $5^2\mathrm{S}_{1/2}, \mathrm{F} = 2$ level of ^{87}Rb and μ_B is the Bohr magneton. Since magnetic field's maxima are forbidden by Gauss's law [61, 62], only atoms in the low-field seeking states, $m_F g_F > 0$, can be trapped in a local minimum of an inhomogeneous magnetic field. However, after the PGC stage, the atoms are spread in different spin states. Hence, before trapping the atoms in a magnetic trap, they are pumped into a single trappable Zeeman sub-state by an optical state preparation.

A simple configuration that can provide a local magnetic field minimum is a quadrupole-type trap, which can be produced by a pair of anti-Helmholtz coils [63]. Such trap features steep magnetic gradients and hence tight confinements. However, due to the axial symmetry, the magnetic field at the center of this trap is zero. This leads to a significant loss of atoms at this point due to Majorana spin-flip [59, 64]. This loss happens if the magnetic field gradient experienced by an atom changes faster than the precession frequency of its magnetic moment, known as the Larmor frequency. In this case, the magnetic moment of the atom can not adiabatically follow the direction of the magnetic field and will undergo a nonadiabatic transition to untrappable states and leave the trap. The loss rate increases at lower temperatures, since the atoms get closer to the bottom of the trap. The loss happens within an ellipsoid of radius $r_0 \sim (v\hbar/\mu_{atom} B'_r)^{1/2}$, where v is the velocity of the atom and $B'_r = \partial B_r/\partial r$ is the radial gradient of the magnetic field [59]. As the temperature drops, the thermal velocity of the atoms reduces and therefore the size of this ellipsoid shrinks. However, the cloud density raises as well and hence the atoms get closer to the bottom of the trap. This results in a T^{-2} dependence of the atomic loss rate, making quadrupole traps unsuitable for evaporative cooling. To overcome this problem, several schemes have been realized to lift the zero at the center of the trap, such as time-averaged-orbiting-potential (TOP) traps [59], Ioffe-Pritchard traps [65, 66], quadrupole-Ioffe-configuration (QUIC) traps [67] and optically plugged magnetic quadrupole traps [68]. The magnetic field of a Ioffe-Pritchard trap can be generated by a single current carrying wire on an atom chip together with an external homogeneous magnetic field and therefore is a proper choice for compact devices. The magnetic potential at the center of this trap can be well approximated by a three-dimensional anisotropic harmonic oscillator potential with eingenfrequencies $\omega_i, i = x, y, z$ [54]. A higher trap frequency leads to a higher density of the atomic cloud and hence a faster collision rate, which will lead to a faster rethermalization of the remained atoms in the trap after removing the atoms with higher energies via rf-induced evaporation. Thus, a higher frequency magnetic trap is preferable as the final trap on which the evaporative cooling will be implemented. The 3-layer atom chip of QG-1 on which versatile wire structures are fabricated made it possible to generate magnetic traps with different volumes and frequencies. This enables the increase of the density of the trapped atoms by sequential compression to the evaporation. The experimental apparatus of QG-1 with the considerations in the design that meets these requirements is described in the following chapter.

CHAPTER 3

Compact and robust apparatus for field applications

The transportable Quantum Gravimeter QG-1 aims to bring the compact BEC setup realized in QUANTUS-2 [69] to applications in geodesy. A gravity measurement will be carried out based on atom interferometry on these atomic sources [51]. Since QUANTUS-2 is designed for microgravity operations, modifications were required to qualify the device for long term drift-free gravimetry in field. This includes additional operational simplicity along with the long term stability. Besides, further efforts on lowering the systematic uncertainties were inevitable to reach to the anticipated unprecedented accuracy in the gravity measurements. A high-flux atomic source permitting a fast cycle time helps to reach the intended statistical uncertainty in shorter integration times [70]. Further considerations in the size, weight and power consumption of the device are required for field applications. The BEC source in QG-1 is prepared on a 3-layer atom-chip assembly in a dual vacuum chamber design. With this, the simplified telecom fiber-based laser system (section 3.8) and the compact electronics (section 3.9) placed in a temperature stabilized mobile rack (3.7), this device will suite for geodetic studies in field.

In this chapter the experimental apparatus, including detailed physical specifications and qualifications of each component is presented. The chapter is divided into two sections. The first section covers up the components of the sensor head in which the BEC is generated and the gravity measurement is carried out. The second section describes the laser system and the driving electronics which are mounted in a temperature stabilized, transportable rack. The control rack can be positioned up to 10 m apart from the sensor head. This suppresses additional noise on the measured signal. The connection in between of the two is realized via low-loss electrical cables and polarization maintaining (PM) optical fibers.

I - Physics package

In this section the physics package is described. This includes the experiment chamber in which the BEC is generated and the interferometry chamber in which the gravity measurement is performed (fig. 3.1). The BEC is produced in a double-MOT design on an atom chip [71]. To perform measurements in the presence of the gravitational field, a long enough falling distance for the atoms is provided in order to increase the time that the atoms spend in the interferometer. The sensor head has a height of 141 cm, a diameter of 56 cm and a total weight of about 140 kg. The vacuum chamber is constructed from a non-magnetic titanium alloy and will be placed inside a 3-layer Mu-metal shield. This is to prevent any disturbance from the background magnetic field or from the magnetization of the components (section 3.6). The overall chamber is maintained at UHV condition and the setup is placed on a vibration isolation platform to decouple the sensor from the environmental vibrations (section 3.7). Further details on each component including the considerations in the design and the characterization of the performance are provided in the following.

3.1 Vacuum system

For the performance of experiments with ultra-cold atoms, a UHV environment is required. This reduces the interactions of atoms with the background gas and increases the lifetime of the atomic ensemble. The vacuum chamber is machined from a non-magnetic titanium alloy Ti-6Al-4V (Grade 5) in the mechanical workshop of the institute. The conflat flanges (CF) are sealed with copper gaskets. The windows and the chip flange are indium sealed using 0.5 mm and 1 mm indium wires (Sigma Aldricht). This keeps the integrated leaking rate under 10^{-11} mbar l/s [72, 73].

The vacuum is initially generated by a turbomolecular pump with a speed of 200 l/s (Pfeiffer TSU 261). This pump was attached to the chamber at three different points via UHV bellows. The connection to the $2D^+$-MOT chamber and the interferometry chamber was established through copper pinch-off tubes (Huntington CPT-133-050) and (Huntington CPT-275-075) for single use. The third pumping point was through a flange equipped with a UHV valve with the size of DN40 (VAT series 541). This valve is connected to one of the three CF connections (DN40) on the pumping section and provides an access for venting and re-evacuation via a large diameter. The pumping section is a spherical tube with an outer diameter of 50 mm, which is placed on top of the sensor head outside of the magnetic shield (see fig. 3.1). With the turbomolecular pump, the background pressure could be decreased to 10^{-8} mbar. At this level, the UHV pumps are activated to attain and sustain ultra-high vacuum environment below 10^{-10} mbar. This is established by a compact pump combining a non evaporable getter (NEG) with an ion getter pump (IGP) (NEXTorr

D200-5) together with a titanium sublimation pump (TSP) (VG Scienta ZST22 110mm). The NEXTorr pump is connected to the second CF connection of the pumping section and the TSP is placed inside a CF tube (DN40) attached to the middle of the interferometry chamber. The NEG pump with a speed of up to 200 l/s sorbs the residual particles through a chemical reaction with the titanium getter. The IGP is required, because noble gases and methane are not pumped by the NEG element. Since the IGP incorporates strong magnetic elements for its principle of operation, it is placed outside of the magnetic shield on top of the sensor head. It provides a pumping speed of 5 l/s and a pressure reading. The design of the TSP in QG-1 is similar to the one in MAIUS-A [72]. It consists of three filaments of titanium-molybdenum (TiMo) alloy, which sublimate titanium on the inside wall of the chamber when heated through electric current. Each filament is activated once after the installation to be cleaned. The activation is done through a 48 A current flowing in each filament for one minute. When the titanium layer on the walls inside the chamber is covered with the residual gases, a reactivation will be necessary. The tube mount of the TSP is attached under an angle of 10° upwards to prevent the fall of titanium flakes on the retro-reflective mirror.

Due to the strong initial outgassing rate of the in-vacuum components and the low vacuum conductance through the chip mount (section 3.3), the NEXTorr pump alone did not suffice in the first place. To encounter this problem a second IGP (Valcon 919-1124) is attached to the middle of the interferometry tube (see fig. 3.1). The vacuum chamber is baked at a temperature of 80°C for a few weeks in order to accelerate the evaporation process of the contaminants. With this, a vacuum pressure of 1×10^{-11}mbar is attained. Afterwards, the pumping valve is closed, the copper tubes are pinched off and the Turbopump is detached. The vacuum chamber is pumped with both IGPs for a few weeks. The second IGP is then switched off and the UHV condition has been maintained. After the demonstration of atom interferometry, this pump will be detached from the experiment. For the readout of the vacuum pressure, an active cold cathode sensor (Pfeiffer IKR 270) mounted to the third CF connection of the pumping sphere is used. The control unit of the vacuum sensor as well as the IGP controller will be placed inside the electronic and laser rack (section 3.7).

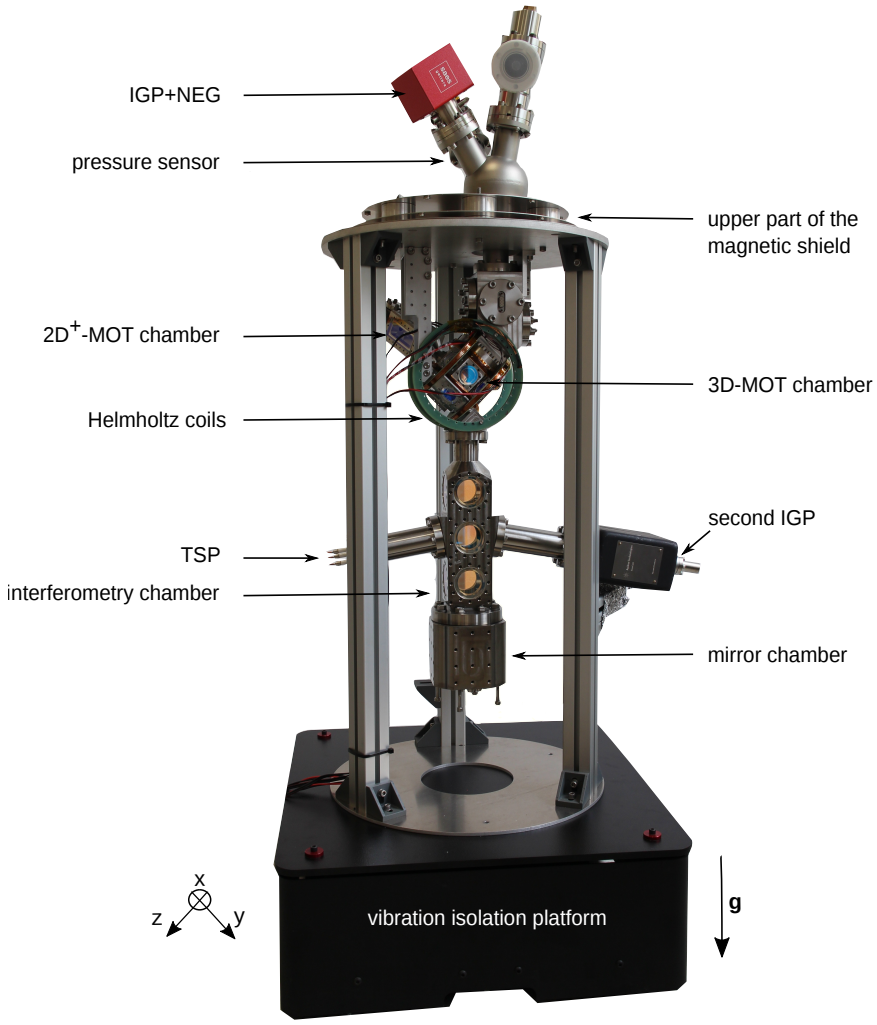

Figure 3.1: Sensor head setup standing on a passive vibration isolation platform. Only the upper part of the magnetic shield is depicted, which sits on three aluminum rods providing the support structure for the Mu-metal shield. The 2D-, 3D-, interferometry and mirror chambers so as the pumping setups are illustrated. The pumping section is placed on top of the sensor head and outside of the magnetic shield. This consist of an ion getter pump (IGP) together with a non evaporable getter (NEG) and a vacuum sensor. The titanium sublimation pump and the second IGP are mounted to the center of the interferometry chamber. This IGP will be disassembled in the near future.

3.2 Vacuum design

The vacuum chamber consists of three parts: 1- A double-MOT chamber in which rubidium BECs are created (section 3.2.1 to 3.2.4). 2- An interferometry chamber in which gravity measurements based on the principle of atom interferometry using Bragg diffraction are performed (section 3.2.5). 3- A chamber containing a high quality 2 inch mirror mounted in a piezo actuated cage and used as the inertial reference for the interferometer (section 3.2.6).

The two parts of the source chamber are connected through a 1.5 mm diameter hole inside a differential pumping stage (fig. 3.2). This double MOT configuration enables keeping a high vapor pressure of rubidium gas in the $2D^+$-MOT chamber while meeting the UHV condition in the 3D-MOT chamber. A high number of rubidium atoms can be pre-cooled inside the $2D^+$-MOT chamber. The cold atomic beam will be loaded in the 3D-MOT chamber, where the sequential cooling to the quantum degeneracy by an atom-chip setup will be performed [69]. The prepared ultra-cold ensemble is let into free fall inside the interferometry chamber. Additionally, the atom chip in QG-1 is mounted at an angle of 45° with respect to **g**. With this, the interferometry beam will enter the chamber and propagate parallel to **g** after a reflection from the chip surface (see fig. 3.2). Atom interferometry is used for the measurement of the gravitational acceleration. In the following sections the construction and characterization of each of these components are discussed in detail. The working principle will be discussed in chapter 5.

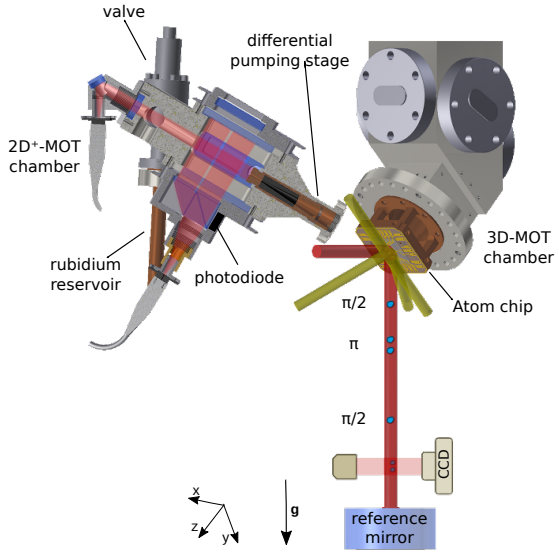

Figure 3.2: A schematic of the source chamber and the interferometry setup in the sensor head. On the left side, a sectional view of the CAD drawing of the $2D^+$-MOT chamber is shown. The differential pumping stage connects this chamber to the 3D-MOT chamber. The atom-chip setup inside the 3D-MOT chamber is illustrated on the right side of the image. The 3D-MOT beams for the mirror-MOT setup are shown in yellow. The interferometry beam (red) is also reflected from the chip surface to enter the interferometry chamber parallel to $\vec{g}$. The retro-reflecting mirror with respect to which the acceleration of the atoms is measured and the detection unit are presented as well.

3.2.1 2D$^+$-MOT chamber

The design of the 2D$^+$-MOT chamber of QG-1 is originated from the one in the QUANTUS-2 experiment [71]. For the operation of a 2D$^+$-MOT a two-dimensional quadrupole trap is required [56]. This is generated from two pairs of coils in a racetrack configuration. The required light fields include two orthogonal beams for the transverse cooling and two counter-propagating beams in the axial direction, the so-called pusher and retarder beams, which provide optical molasses cooling (section 5.2.1). The computer-aided design (CAD) drawing[1] of the 2D$^+$-MOT chamber is illustrated in fig. 3.2. It is a cuboid shape chamber with the inner dimension of 56 mm × 41 mm × 41 mm. The lateral sides of the chamber provide the optical access for the cooling laser beams. On the side facing towards the 3D-MOT chamber, a 10 mm view port provides the access for the pushing beam. All optical view ports are made of glass substrates (N-BK7), which are anti-reflective (AR) coated for 780 nm and 1560 nm light on the outside (Newport). These windows are indium sealed to the titanium chamber using 0.5 mm diameter indium wires. Four electromagnetic coils are mounted on the lateral sides of the chamber. The optics for the collimation of the cooling and the pusher lights are illustrated in fig. 3.2 and will be described in section 3.5.1. The connection of the 2D$^+$- to the 3D-MOT chamber is provided via a DN16 CF flange in which the differential pumping stage (section 3.2.3) is set up.

3.2.2 Rubidium source

A breakseal ampule (ChemPur) containing one gram of rubidium metal in its natural isotope distribution is used as the rubidium reservoir providing the required atoms for the experiment. This reservoir is placed inside a copper tube connected to the 2D$^+$-MOT chamber through a UHV valve (see fig. 3.2). This ampule is broken by pressing the copper tube after reaching the UHV condition in the system. The vapor pressure of rubidium inside the 2D$^+$-MOT chamber can be controlled through the temperature of this tube. The heating is done using an electric current passing through a pair of wires twisted against each other and winded around the copper tube. A 10 m long copper wire with a diameter of 0.2 mm (ETCOM Cul-0,2V180) is used for this purpose. The currents in this pair of wires flow in opposite directions in order to prevent any magnetic induction introduced. A Thermostat (AIRPAX 67L040) in series to the heating wire switches the heating off when the temperature rises above 40°C. The current in these wires is controlled via a commercial TEC controller (miniature precision peltier temperature contoller TEC-1091 Meerstetter Engineering), which additionally provides a readout of the temperature. The UHV valve is heated to 1°C above the reservoir temperature to prevent the condensation of the rubidium atoms on the inner wall of the valve. Here, a 1.8 m long resistance wire (10 Ω/m) winded in the same manner is used to flow the heating current. A similar TEC controller controls and monitors the current in this wire. The vapor pressure of rubidium inside the 2D$^+$-MOT chamber is measured using doppler-free saturation absorption spectroscopy and is described in section 5.1.

1 Autodesk inventor software is used.

3.2.3 Differential pumping stage

The differential pumping stage is a 58 mm long copper rod with a hole inside connecting the two chambers. Along the first 10 mm, the hole is straight with a diameter of 1.5 mm. Afterwards, it becomes conical and widens with an angle of 8° over 40 mm (see fig. 3.2). A segment of the pumping stage is made of a 30 mm long graphite tube to absorb the non-collimated rubidium atoms and improve the differential pumping efficiency [72, 74]. The surface on the side inside the $2D^+$-MOT chamber forms a 45° angle with respect to the axial axis. This surface is polished to serve as the mirror for the pusher and retarder beams. The optical adjustment of the pumping stage is permitted by its threaded outer ring. After the alignment, the pumping stage is fixed in place via a retaining screw.

3.2.4 3D-MOT chamber and chip flange

For the operation of the 3D-chip-MOT, only four cooling light beams are required. Two of these four beams are reflected at the surface of the atom chip, creating a mirror-MOT configuration [75]. The required magnetic field is generated by the atom chip and three pair of Helmholtz coils. The 3D-MOT chamber is an octagonal shaped chamber with an inner diameter of 64 mm and an outer diameter of 89 mm (fig. 3.9). One of the eight lateral sides is for the connection to the $2D^+$-MOT chamber and the other seven provide optical access with an aperture of 20 mm. All the view ports are indium sealed with glass substrate (N-BK7), which are AR coated for 780 nm and 1560 nm on both sides. Two of these lateral view ports are for the access of the cooling beams and two others are for the assembly of the absorption detection collimator and the charge-coupled device (CCD) camera (section 4.1). The chip flange is mounted to one of the perpendicular axes and holds the atom chip inside the 3D-MOT chamber under a 45° angle with respect to $\mathbf{g}$ (fig. 3.2). It is hanging under the magnetic shield and is connected to the pumping stage through a CF flange (DN40). This flange is indium sealed to the 3D-MOT chamber using a 1 mm thick indium wire (Sigma Aldericht). For the connection of the chip wires, four titanium feedthroughs are included on the chip flange (section 3.4.1). The wall opposite to the chip has a view port with an aperture of 38 mm and provides access for the fluorescence imaging (section 4.3). Three additional optical axes with view ports of 20 mm are forming a 45° angle to the plane of this window. These provide the access for two additional required MOT-beams and the interferometry beam. These three beams will reflect from the chip surface at an angle of 45°. Titanium grade 5 screws are used to mount the collimators, the absorption detection camera and the fluorescence detection telescope on the view ports.

Three pairs of Helmholtz coils are assembled around the 3D-MOT chamber to generate the bias fields, which together with the atom chip provide the required magnetic fields to cool and trap the atoms.

3.2.5 Interferometry chamber

The 297.5 mm long interferometry tube with an inner diameter of 38 mm and an outer diameter of 70 mm is copper sealed to the bottom of the 3D-MOT chamber with a DN40 CF flange (fig. 3.1). With ten view ports of aperture 38 mm, this chamber provides manifold access for light beams to manipulate and detect atoms. Double sided AR coated N-BK7 glass substrates with 50 mm diameter are indium sealed on all of the view ports. A CCD

camera and a detection collimator will be attached to the lower view ports to detect the atomic states after the interferometry. With this, a maximum free-fall distance of 320 mm is provided. Two CF flanges (DN40) are attached to the middle of the interferometry chamber. A 126 mm long vacuum tube is connected to each of them under an angle of 10°. One of these tubes provides the housing for the titanium sublimation pump (section 3.1). A copper pinch-off tube was connected to the opposite tube for the initial pumping, which is currently replaced by a second IGP as described in section 3.1. A blind flange (DN40) will cover this port after disassembling this IGP.

3.2.6 Retro-reflection unit

The retro-reflection unit with respect to which the acceleration of the atoms is measured is a titanium chamber with a height of 100 mm and an outer diameter of 116 mm. This unit is copper sealed (DN63) to the bottom of the interferometry chamber (see fig. 3.1). A 2 inch mirror with a thickness of 30 mm and a high surface quality (Laseroptik Garbsen) is placed inside this chamber. The interferometry beam is retro-reflected from this mirror to provide the required counter-propagating beams for the atom interferometry. In this configuration, all other optical elements and their introduced phase noise are common for both of the interferometry beams. Therefore, the retro-reflective mirror acts as the inertial reference and special consideration in its surface quality and its vertical displacements should be taken into account. The mirror substrate is made from fused silica with near zero thermal expansion coefficient and has a surface form tolerance of 3/0.1, which corresponds to a surface flatness of $\lambda/24$ at 780 nm. With this in-vacuum mirror, the requirement of an additional optical element in the path of the intereferometry beam is eliminated, which leads to a lower wavefront abberation.

The reference mirror is mounted inside a tip-tilt stage, which enables its three-dimensional positioning to correct for the Earth's rotation providing a Coriolis effect compensation. The CAD design of this mount is depicted in fig. 3.3. The mirror cage is glued (Epotek H77) on three piezoelectric actuator stacks with a displacement range of maximum 38 μm (PI Ceramic PICMA PIC252). This enables a tilt up to ± 1.4 mrad, which is sufficient for the compensation of the Earth's rotation. The mirror is held inside the cage on three titanium spheres with 3 mm diameter and fastened in place with titanium screwing rings and retaining rings plus a karlez-o-ring.

To prevent the occurrence of Etalon effect inside the reference mirror, its top surface is high-reflective (HR) coated for 780 nm light and the bottom surface is AR coated. A view port with a diameter of 38 mm provides an optical access for mirror orientation with respect to $\mathbf{g}$. A N-BK7 glass substrate is indium sealed to this view port. Etalon effect which could occur from the reflection of the aligning beam in between of the mirror and the view port glass, is canceled by AR coating both sides of the glass substrate as well as mounting this glass with a 3° tilt (fig. 3.3).

For the electrical connection of the piezoelectric actuator stacks, UHV compatible Kapton isolated wires (Allectra 311-KAPM-075) with a core diameter of 0.75 mm are glued to one of their electrical terminals. The other side of these wires are crimped to six pins of a non-magnetic UHV compatible sub-D 9 connector (Allectra 211-MS09-UHV). The connector is screwed on a titanium sub-D feedthrough (SRI SRISD5001-9s). Another

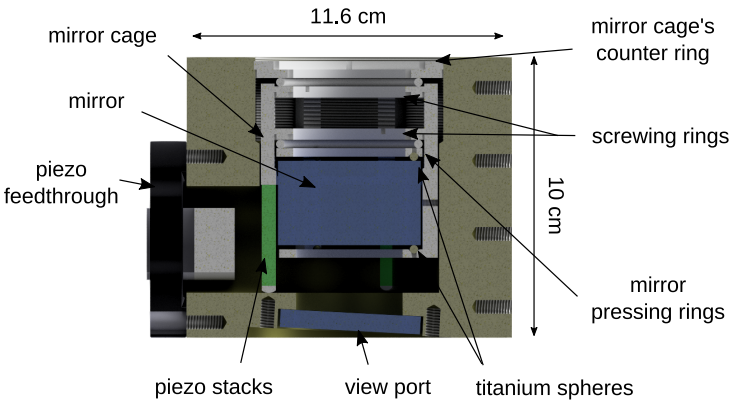

Figure 3.3: CAD drawing of the mirror mount stage. A high quality retro-reflective mirror provides the inertial reference for the gravimeter. The mirror is mounted inside the vacuum chamber in a tip-tilt stage, which enables the three-dimensional orientation of the mirror to compensate the Coriolis effect. The wavefront distortion in the gravity measurement is reduced by placing this mirror inside the vacuum chamber and excluding an additional optical view port in the path of the interferometry beams.

sub-D 9 connector is made for the connection outside of the vacuum to the piezo driver. The performance is tested at 150 V provided by a 3-channel piezo controller (Thorlabs MDT693A) and a total tilt up to ±1.3 mrad is demonstrated, which is sufficient for the Coriolis effect compensation.

3.3 Pumping speed

A pressure sensor is assembled on the pumping section on top of the sensor head (fig. 3.1). To analyze if the single NEXTorr pump attached to the pumping section is sufficient to keep the UHV condition in the 3D- and the interferometry chamber, the pumping speed and the vacuum pressure at each of these chambers are estimated. The pumping speed at each point of a chamber can be calculated from [76]

$$S = \left(\frac{1}{C} + \frac{1}{S_P} \right)^{-1} \tag{3.1}$$

where C is the conductance from the pump to this point in liter per second and S_P is the pump capacity. The readout pressure at the Pfeiffer sensor in the experiment is equal to 1.1×10^{-11} mbar. The calculated pumping speed and pressure at each part of the vacuum chamber for this case are presented +in table 3.1, which shows that a low enough vacuum pressure is provided with this single pump.

Table 3.1: The pumping speed and the vacuum pressure in each chamber are calculated from the conductance at this point to the vacuum pump. This calculation is done for the case in which the readout pressure at the Pfeiffer sensor is equal to 1.1×10^{-11} mbar.

Chamber	Pumping speed (l/s)	Vacuum pressure (mbar)
3D-MOT chamber	4.20	1.2×10^{-11}
Mirror chamber / lower part of the interferometry chamber	3.53	1.4×10^{-11}
$2D^{+}$-MOT chamber	0.06	8.6×10^{-10}

3.4 Magnetic field source

In all the steps of generation of the source for atom interferometry, well controlled magnetic fields are required [54]. These fields are generated by current carrying wires on the atom-chip assembly in combination with homogeneous bias fields from the Helmholtz coils. In this section these two elements will be discussed. Further details on the production procedure of the atom chip are described in appendix A.

3.4.1 Atom chip

The atom chip is mounted at the center of the 3D-MOT chamber. Since it is placed very close to the atoms and inside the vacuum chamber, special care is taken in choosing all the components from non-magnetic materials with a low outgassing rate. The design of the atom chip in QG-1 stems from MAIUS-A chip [72] with the modifications required to fit for applications in the presence of the gravity. Figure 3.4 shows the QG-1 atom chip assembly. It consists of three layers of wire structures glued on top of each other. The lowest one, the so-called mesoscopic structure, is made of layers of winded copper wires. The two other layers, the base chip and the science chip, are made of micro-wire structures grown on aluminum nitride substrates via lithography. The three layers are mounted on a holder with 58 mm diameter and 70 mm height. This mount is made of oxygen-free copper (Luvata Cu-OFE OFHC) with a low outgassing rate. It additionally has a high thermal conductivity, which makes it suitable as a heat sink to dissipate the heat generated from the current carrying structures. The holder is screwed to the titanium flange with eight titanium screws. Each layer of the atom chip is described in the following.

Mesoscopic structure

The lowest layer of the atom chip is a 42 mm × 42 mm copper block depicted in fig. 3.5(a). This mesoscopic structure consists of copper wires (Allectra 311-KAP2) with an inner diameter of 0.6 mm. These wires are electrically isolated with Kapton insulation and form an outer diameter of 0.9 mm. The mesoscopic layer consists of three structures. The lowest layer is the U-structure, which in combination with a bias field provides the quadrapole field for the 3D-chip-MOT (chapter 5). In order to generate the required magnetic field strength with less current, it is winded such that seven parallel wires form the U-structure. The middle section of the U-structure has a length of 27 mm. The wires are placed in a 2 mm deep inlet cut on the surface of the copper mount. On top of this, two parallel

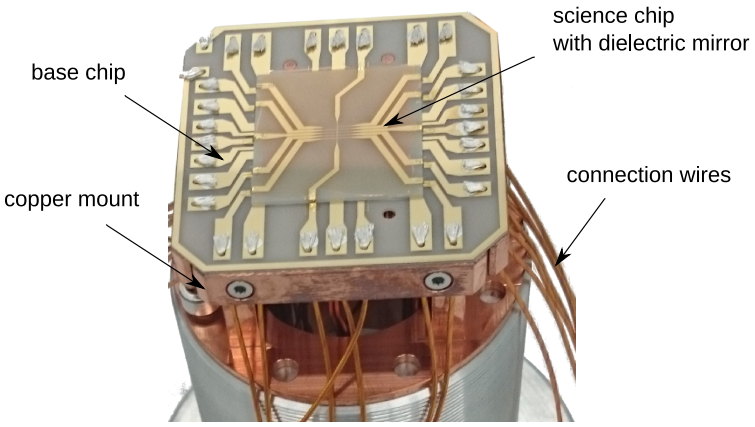

Figure 3.4: A photograph of the atom-chip assembly with its three layers of wire structure. The mesoscopic wires are winded in the inlets of the copper chip mount. The glued base and science layers as well as the transferred dielectric mirror coating can be seen in the picture.

wire-structures with a distance of 12 mm, each consists of three winded wires with a length of 35 mm are placed. Afterwards, is the I-structure consisting of three winded wires. These together form the mesoscopic-H and are placed inside 1 mm deep inlets on the surface of the copper mount above the U-wires. Mesoscopic H together with the Z-wire of the base chip and the bias coils provides the magnetic field for the initial magnetic trap. The I and the two side wire structures of H are winded independently and are connected to three separated pin pairs of a sub-D connector. With this, it is possible to apply independent currents in each of the three. The mesoscopic wires can handle a maximum current of 10 A for a few milliseconds. Thermally conductive UHV-compatible epoxy (Epotek H77) is used to provide the adhesion plus high thermal conductivity between wires and the copper mount. Hereby, the heat generated due to the large currents can be dissipated.

Base chip

On top of the mesoscopic structure, the so-called base chip is glued using a layer of thermal conductive epoxy (Epotek H77). This provides the adhesion and high heat dissipation from the base chip to the copper mount. The substrate is pressed before and during the cure of the epoxy to reach the thinnest possible layer and avoid any remained air bubble. Since the maximum particle size of the epoxy based on the datasheet is equal to 50 μm, this is estimated as the distance between the mesoscopic and the base chip. The base chip substrate is chosen from aluminum nitride (AlN) as it provides a high heat conductivity of 170 W/mK and is electrically isolated (HEBO spezialglas). This substrate is 635 μm thick and the base chip is a 48 mm $\times$ 48 mm square cut from it. The wire structure of 11.2 μm height from gold is grown on the substrate in an electroplating process (appendix A). Gold is chosen because of its high electrical and thermal conductivity, $\sigma = 4.10 \times 10^7\, \Omega^{-1}\mathrm{m}^{-1}$ and 314 W/mK respectively, in addition to its convenience in microfabrication. The base chip structure contains a middle wire with the width of 500 μm (fig. 3.5(b)). Perpendicular

to this are four parallel wires with the width of 500 μm and the distance of 2 mm to each other. Each of these wires are 14 mm long. With this, different sizes of Z-structure are provided for the generation of harmonic traps with different frequencies. In QG-1, the outer Z-structure in combination with the mesoscopic H and the bias field is used to trap atoms in the initial magnetic trap (section 5.4.2). At the middle of the base chip lays two small U-structures with a width of 50 μm and a distance of 25 μm to the middle wire. These wires are used for the generation of the radio frequency (rf) for the evaporation or for the adiabatic rapid passage (ARP) to transfer the atoms to a non-magnetic state before the interferometry step to eliminate the linear Zeeman effect [58]. Additionally, a loop wire, the so-called O-structure, with a width of 1 mm is placed around the edge of the base chip as an alternative for the generation of the radio frequency. The base chip structure can conduct currents up to 6.5 A for a few milliseconds.

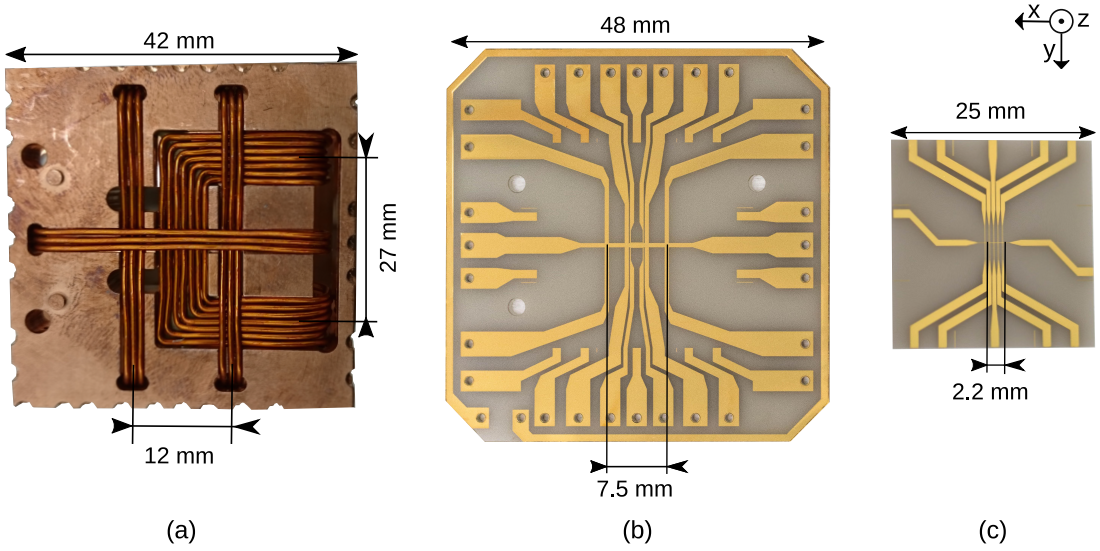

Figure 3.5: The three layers of the atom chip and their wire topologies are illustrated. a) The mesoscopic structure provides the quadrapole field in the 3D-chip MOT and part of the initial magnetic trap. b) The base chip generates the field for the initial magnetic trap and the radio frequency for the evaporation and the adiabatic rapid passage. c) The science chip is used for the final magnetic trap and the evaporative cooling.

Science chip

On top of the base chip, the so-called science chip, which is a 25 mm × 25 mm square from a similar substrate is glued. Using the same recipe (appendix A), smaller wire structures with a height of 13.2 μm are fabricated. With a 50 μm wide middle wire and five 4 mm long wires perpendicular to it, several sizes of smaller Z-structures in comparison to the base chip can be formed (fig. 3.5(c)). Each of the middle wires are 50 μm wide and are placed at 500 μm distance from each other. In QG-1, the outer Z-structure of the science chip together with the Z-wire of the base chip and the proper bias field is used to trap atoms in the final magnetic trap (section 5.4.3) and evaporatively cool them to BEC [69].

This structure can conduct up to 2.5 A of current for a few milliseconds.

Dielectric mirror

In a mirror-MOT setup, two of the MOT beams are reflected from the surface of the atom chip at a 45° angle. In QG-1, the interferometry beam as well reflects from the chip surface. Hence, a dielectric mirror with a high reflectivity of above 99.5% at 45° angle for 780 nm light (OIB Jena) is transferred on the surface of the science chip. The dielectric mirror is 2 μm tick and consists of alternating layers of titanium oxide (TiO_2) and silicon oxide (SiO_2) grown on a substrate from quartz. This mirror is transferred on the surface of the science chip with UHV-compatible optical epoxy (Epotek 353ND). Since the goal in QG-1 is to reach an unprecedented inaccuracy in the gravity measurement and the interferometry beam reflects from the chip surface, its wavefront distortion can be minimized by improving the surface quality of this mirror. Therefore, variety of tests have been performed to achieve a better surface quality in comparison to the previous generations of the atom chip [71, 72]. One limiting factor in the older versions was caused due to the existing gaps in the dielectric layers, which are formed because of the dust particles on the quartz substrate before their growth. After the transfer on the atom chip, the penetrated epoxy through these gaps causes a lens shape on the chip surface. This effect can be seen in fig. 3.6(a). In QG-1, the viscosity of epoxy is increased by pre-heating it to 75°C before the transfer process (appendix A.3). This viscous glue can not penetrate the gaps in the dielectric layers. Furthermore, as a result of using a more viscous epoxy, a thicker layer of it is applied under the mirror surface. This reduces the seen topography of the wire structure on the reflected light. A comparison of the surface quality of the QG-1 mirror to the previous generations of atom chips is shown in fig. 3.6. This measurement is performed using a 3D-measuring microscope (Leica DCM 3D[1]).

The height of the glue and the surface homogeneity of the reflective coating is measured afterwards with a profilometer (Dektak 6M[2]). Since the assembled chip setup is not fitting under the profilometer stylus, the measurement is performed on a test science chip on which the dielectric mirror is transferred with an identical recipe. The result of this measurement is shown in fig. 3.7. The total height of the glue under the dielectric mirror layer is measured at 16.5 μm (fig. 3.7(a)). The peak-to-valley of the surface roughness over the wire structure is 30 nm, which corresponds to $\lambda/26$ at 780 nm (fig. 3.7(b)).

The reflectivity of the mirror at 45° is specified as more than 99.5% by the manufacturer. This is tested using a 780 nm laser beam. Figure 3.8 shows an image taken with this light by a CCD camera (PCO AG pco.1400). The pattern of the science chip is visible because of the small percentage of the light transmitted through the dielectric layers. This affects the wavefront quality of the interferometry beam reflecting from the chip surface. This problem will be resolved using a BEC source, due to its negligible expansion rate and an accurate control on its initial position and velocity with the atom chip. The BEC will start the free fall in an area of the wavefront, which is not distorted due to the chip pattern.

1 facilitated by LNQE
2 facilitated by PTB

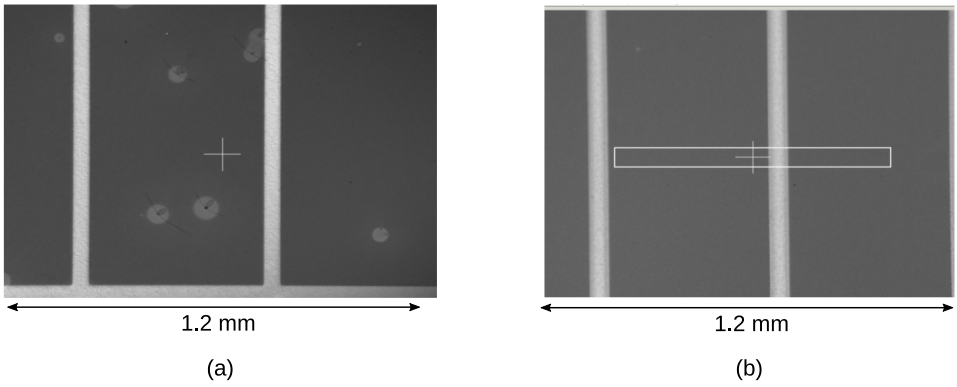

Figure 3.6: A comparison of the surface quality of the reflective layer on the atom chip in the previous generation (a) to the QG-1 experiment (b). The bubble structure caused by the penetration of epoxy through the gaps of the dielectric mirror can be seen in image (a). These gaps are caused by the dust particles on the quartz substrate before growing the dielectric layers.

Electrical connections

The electrical contact of the science chip is provided through the connections to the base chip structure. Two thin gold ribbons with a thickness of 25.4 μm and a width of 381 μm (Materion) are welded (Miyachi Unitek[1]) between the science and base chip wires (appendix A.4). The electrical contacts of the base chip is provided by copper wires with a core diameter of 0.75 mm (Allectra 311-KAPM-075). These wires are glued to the base chip structure with electrical conductive UHV-compatible epoxy (Epotek H21D) and are Kapton insulated with the final diameter of 0.81 mm. They are clamped in place by four 3 mm thick copper straps, which are screwed on the sides of the copper mount using titanium screws (fig. 3.4). The other end of these wires are crimped to the pins of a sub-D 15 plug (Allectra 211-MS15-UHV) in the case of the science chip and can carry a maximum current of 5 A per pin. Since the current in the base chip and the mesoscopic structure is above this limit, two sub-D 9 plugs (Allectra 211-MS09-UHV) are used for the electrical connection of these wires. In this case, the maximum current in each pin can rise up to 10 A. For the three rf structures, the Kapton wires are crimped to coaxial cables, which are connected to three subminiature version A (SMA) connectors (Allectra 380-SMA-MX-500). These SMA plugs are connected to a titanium SMA feedthrough (SRI SRIXX CF40). All the components including the cables, plugs, crimp pin connectors and screws are chosen from non-magnetic and UHV compatible materials. After the assembly, the resistance of each structure is measured to confirm the quality of bonding.

Outside of the vacuum, the connections from the feedthroughs are established via sub-D and SMA plugs. For the connection of the mesoscopic structure to the electronic rack,

1 facilitated by LNQE

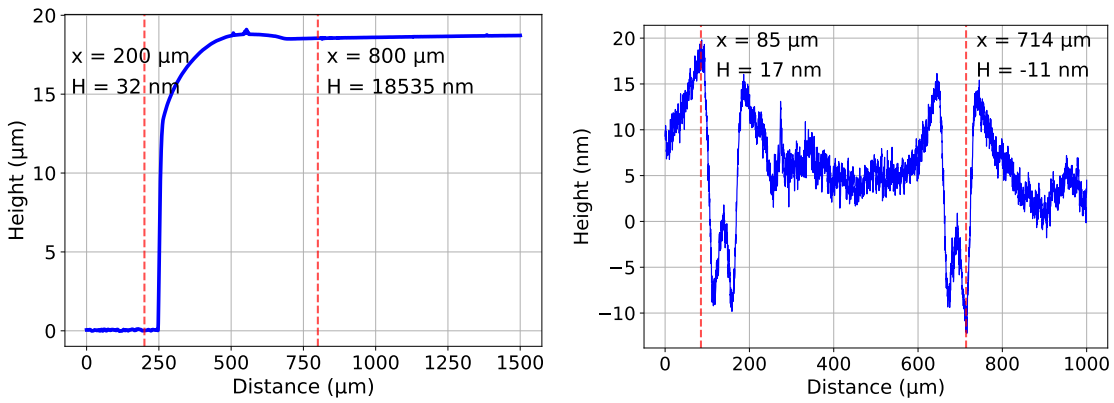

(a) **(b)**

Figure 3.7: a) Surface measurement of the dielectric layer on the atom chip with a profilometer. The height of the epoxy is measured at the edge of the transferred mirror. The total height from the surface of the coating layer to the science chip is measured as 18.5 μm. This includes the 2 μm of the dielectric mirror plus 16.5 μm of epoxy. b) Measurement of the surface quality of the reflective coating above the middle wire structure of the science chip. A 13 μm high gold wire causes a height difference of only 30 nm on the mirror surface.

Figure 3.8: An image of the surface of the mirror coated science chip taken by a 780 nm laser beam at a 45° angle. The wire structure is visible due to the small percentage of the transmitted light through the dielectric mirror. In this setup, the reflectivity of the mirror is measured as 94.2% at 45°.

cables with 0.75 mm^2 surface area and a maximum current of 12 A are adopted. In the case of the base and science structures, thinner cables with 0.5 mm^2 surface area and a maximum carrying current of 9 A are used.

Orientation of the atom chip

For the measurement of the Earth's gravity field, the interferometry beam has to be parallel to **g**. For this, the beam enters the chamber horizontally to be parallel to **g** after the reflection from the chip surface. Therefore, the atom chip is mounted under an angle of 45° with respect to **g** and the MOT collimators could not be mounted on the horizontal axes. Consequently, the U-structure had to be rotated and be placed in a C form in order to

generate a quadrupole field with its axis oriented along the cooling beams for the operation of a U-MOT (section 5.2.2). If the H- and Z-structures were rotated correspondingly to keep the weak confining axes of the 3D-MOT and the magnetic trap parallel to each other, the weak confining axis of the harmonic potential would be in the direction of **g** and the atoms would not be held in the trap against the gravity[1]. Despite the fact that this configuration makes finding the proper mode match in between of the laser cooled atoms and the followed up magnetic trap more difficult for an efficient loading of the atoms, this is the only possible geometry for the measurement of the Earth's gravity field.

Definition of the coordinate system

The origin of the coordinate system in QG-1 is defined at the center point of the science chip and on the surface of the dielectric mirror coating. The z-axis is defined as the normal axis to the chip surface pointing towards the atoms (fig. 3.9). The y-axis is perpendicular to the horizontal wire of the science chip and points downwards under a 45° angle with respect to **g**. The x-axis is parallel to the horizontal wire of the science chip and the direction is such that it forms a right-handed orthogonal coordinate system. Herewith, the **g** vector is pointing in +y-+z direction. The positive direction of the current in the chip structures and in the coil wires are defined such that they generate a magnetic field pointing towards the positive direction of the coordinate system at the position of the atoms.

3.4.2 Coils

For the generation of a two-dimensional quadrapole trap with a line of zero magnetic field along the center of the $2D^+$-MOT chamber, four rectangular shaped coils placed around the chamber are required. The 2D-coils are winded on machined titanium holders. Titanium is chosen, because of its rigidity since the 2D optics are assembled on them. In order to prevent short circuits, the surface of these holders is anodized. Each coil has the dimension of 81 mm × 45 mm and is placed at a distance of 62 mm from its pair. Each of the coils consists of 64 windings. The 2D-coils together generate a magnetic field gradient of 6.73 G/(cm.A) at the center of the $2D^+$-MOT chamber.

Three pairs of coils in Helmholtz configuration are mounted on the 3D-MOT chamber. These coils provide the homogeneous magnetic fields, which are required together with the magnetic fields of the atom chip for cooling and trapping of the atoms. They are named after the direction in which they are providing the field (fig. 3.9). The x- and y-coils are winded on glass fiber rings (ROTEK GFK-HGW2372.4). Glass fiber is chosen as it is nonconductive and rigid. The conductivity of these rings would increase the switching time of the coils due to Eddy currents. For a rapid generation of the BEC, fast switching of the coils is necessary. However, the switching time of these coils are slow due to their

1 The strong (weak) axis of a 3D-MOT or a magnetic trap refers to the axis along which the confinement is the strongest (weakest). In the magnetic field generated from the U- or Z-structure on an atom chip, the strongest confinement is along the axes perpendicular to the center wire structure and the weakest confinement is along this wire added through the bent sides of the wire structure. The confinement in a U-MOT is described in section 5.2.2 and in a harmonic trap of the Z-structure is described in section 5.4.2.

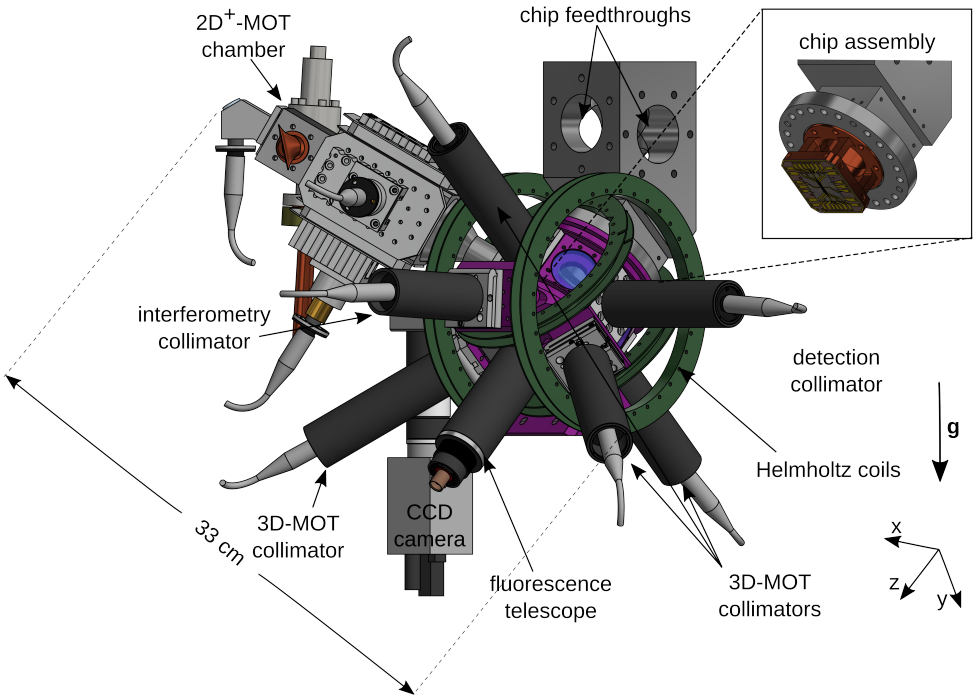

Figure 3.9: CAD model of the double-MOT chamber and the chip setup. The $2D^+$-MOT chamber (section 3.2.1), the 3D-MOT chamber (section 3.2.4), the beam collimators (section 3.5.1) and the detection setup (chapter 4) are presented. The chip coordinate system (section 3.4.1) and the direction of the Earth's gravity are illustrated. The Helmholtz coils are named based on the direction in which they generate the magnetic field. The inset shows the atom-chip assembly mounted in the chip flange.

large size and high inductance. To confront this, the x- and y-coils are divided into two coil pairs connected to each other in series. In such a configuration, the bigger coil pair, which generate a larger bias field can be used for the operation of the 3D-MOT. For the evaporation, where a faster switching is required, the smaller pairs can be used. The smaller coils are 14 times lower in inductance and 3 times lower in resistance in comparison to the larger coils. The measured values are presented in table 3.2. The z-coils are winded directly on the 3D-MOT chamber. In this way, they are closer to the atoms and require less windings to generate the same magnetic field. This helps in the miniaturization and lowers the power consumption. The z-coils are therefore the smallest pair with a radius of 49 mm and 35 windings. Copper wires with 1 mm core diameters are used (Menting Mikroeletronics Cul-1.00). The z-coils generate a bias field of 6.42 G/A in the z-axis. For the other two coil pairs, copper wire with a core diameter of 0.8 mm (ETCOM Cul-0,8 V180) is used. The y-coils, are slightly larger with a radius of 68 mm. First the inner 15 windings are done, which together with another 45 windings will form the big y-coils. Herewith, the big y-coils contain 60 windings and can generate a magnetic field of 8.56 G/A at the position of the atoms, while the small y-coils with 15 windings can provide 2.23 G/A.

The largest pair of the coils, the x-coils, are winded in the same way. This pair with a diameter of 80 mm consists of 17 windings for the small x- and 68 windings for the big x-coils. The big x-coils can generate a 7.64 G/A bias field, while the small x-coils provide only 2.01 G/A. Using safety electronics (section 3.9.3), the maximum current in each coil is limited to 7 A. In the table 3.2 the properties of the QG-1 coils are summarized.

Table 3.2: For each coil on the 3D-MOT chamber, physical properties, measured resistance and inductance and the calculated bias fields are presented. Resistances are measured for each pair of coils. Inductances are measured in the Helmholtz configuration. The resistance of the connection cables are as well included in the presented values.

Coil	Radius (mm)	Number of windings	Measured resistance (Ω)	Measured inductance (μH)	Simulated bias field (G/A)
X	80	68	2.5	2601	7.64
X-small	80	17	0.9	184	2.01
Y	63	60	1.8	1379	8.56
Y-small	63	15	0.6	98	2.23
Z	49	35	1	214	6.42

For a better understanding and improvement of the experiment, the generated magnetic field from the QG-1 coils and chip structure is simulated in the work of a master thesis [77]. This simulation is originated from the Biot-Savart simulation for QUANTUS-2 [71] and is modified and optimized for QG-1. The details on this simulation and a comparison to the experimental results are provided in [77]. This can aid in the optimization process and improvement of the experiment.

3.5 Optical appartus

3.5.1 Collimators

The light from the PM optical fibers enters the $2D^+$- and 3D-MOT chambers after collimation. The optical system of the 2D-transverse cooling beams is illustrated in fig. 3.10(a). The light from the fiber is first collimated with a two lens system. Two best form lenses are used for this purpose, a divergence lens with a focal point of -10 mm (Bernhard Halle OBF0.010) and a convergence lens with a focal point of $+20$ mm (Bernhard Halle OBF020). These lenses are AR coated on both sides. The optical fiber is connected to the input of the collimator via a fiber adapter made of titanium (Schäfter+Kirchhoff 10AF-4-FC+PP1020-Ti). The diverging lens is placed at 24.7 mm distance from the fiber tip and the converging lens is placed another 12.9 mm away from the first lens. The light after this collimator is a 17 mm linear polarized collimated beam. In order to provide a larger cooling region for the atoms, this beam is then divided into two parallel beams with equal powers and its polarization is transferred to the circular polarization for the operation of the $2D^+$-MOT. This is done by the optics depicted in fig. 3.10(a) (Foctek). This is a 50:50 beam splitter cemented to a prism with HR coating on the inside face. A quarter waveplate with a size of 40 mm $\times$ 20 mm is then cemented to the front of this

optic, which changes the polarization of the light from linear to circular before it enters the $2D^+$-MOT chamber. One of the two 2D-collimators provides a right-circular polarized light and the other one provides a left-circular polarized light. With this, the correct helicity is produced. Additionally, the counter-propagating beams require opposite circular polarization with respect to each other. Therefore, at the opposite side of the chamber, a $40\,\text{mm} \times 20\,\text{mm}$ quarter waveplate with AR coating on the inner surface and HR coating on the outer surface is mounted on the coil holder (see fig. 3.2). With this, the helicity of the beams flips after the reflection. The mechanical hosing of the collimators is machined from titanium and brass and the inner faces are anodized to prevent stray light. The diameter of the beam from the collimator is reduced to 16 mm before entering the 2D-optics by a teflon ring placed in between of the optical elements and the mechanical hosing. For the purpose of monitoring the light power in the transverse beam and for spectroscopy in the $2D^+$-MOT chamber, a photodiode (Hamamatsu S5106) is mounted on the housing (fig. 3.2). The transverse beam is collected on this photodiode after passing through the length of the chamber twice, and reflecting from the 50:50 beam splitter. This photodiode is mounted on a transimpedance amplification circuit board designed in the institute [78].

With the above optics, the transverse cooling beams for the function of a 2D-MOT are provided. In order to enhance the system to a $2D^+$-MOT, two other beams, the pusher and retarder, are additionally required (section 5.2.1). The pusher collimator is depicted in fig. 3.10(b). This is a one lens collimator for which a plano-convex lens with a focal point of 40 mm (Thorlabs LA1304-B) is adopted. In order to fit inside the magnetic shield, the collimator is bent under a 90° angle and a half-inch mirror (Thorlabs BB05-E03) is used to reflect the beam. From this, a linear polarized collimated beam with a diameter of 9 mm is produced. A neutral-density (ND) filter with 40% transmission (Thorlabs NE504B-B) is glued in front of the lens to lower the light intensity (For the characterization of the optimal light intensity in the pusher beam refer to section 5.2.1). Afterwards, the beam diameter is reduced to 6 mm by an anodized metal aperture, which is screwed to the front of the collimator. This is to prevent stray light caused by reflections from inside the chamber. The pusher collimator is mounted with three screws on the vacuum chamber. This permits fine adjustment of the direction of the beam. The collimator is fixed in its aligned position using three retaining screws for long term stability. To monitor the pusher beam's power, a photodiode (Farnell SLSD-71N100) is glued between the aperture plate and the collimator.

Instead of building another collimator, the reflection of the pusher beam from a 0° mirror (Thorlabs) is used as the retarder beam (see fig. 5.3). This grants further simplification and miniaturization of the setup. The pusher beam is reflected by the polished surface of the differential pumping stage under a 45° angle. The reflected light passes through a 50% transmitting ND filter (Thorlabs NE503B) and retro-reflects from a one inch broadband dielectric mirror mounted in a flexure mirror mount (Siskiyou IXF1.0a). This reflected beam counter-propagates the pusher beam and has 25% of its intensity since it has passed through the ND filter twice. The polarization of these two lights are parallel to each other. Because of the 1.5 mm diameter hole at the middle of the differential pumping stage there is a hollow in the retarder beam, which is required for the operation of the $2D^+$-MOT (section 5.2.1).

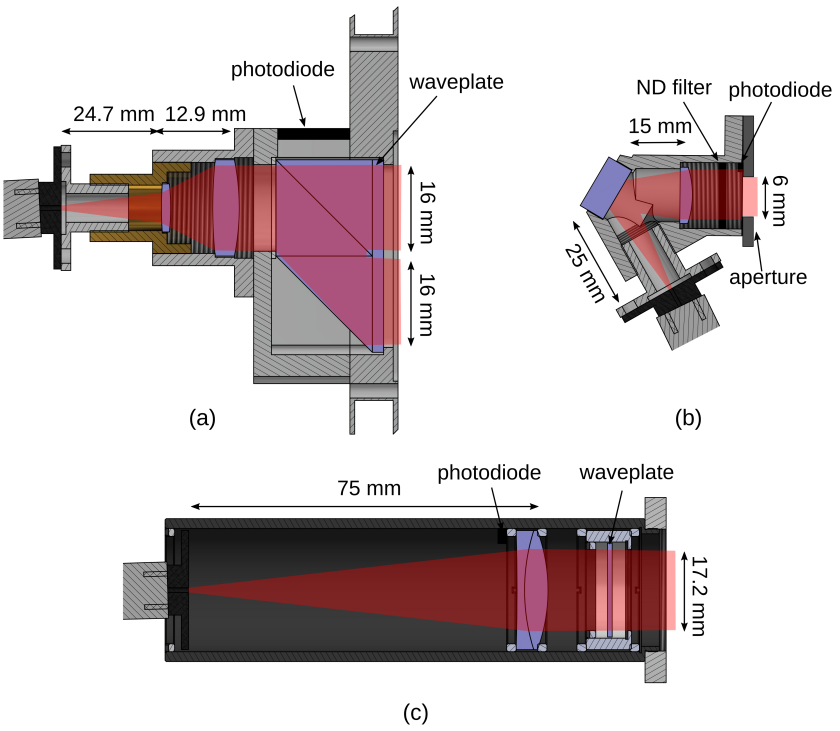

Figure 3.10: CAD drawings of the a) $2D^+$-MOT transverse beam optics, b) $2D^+$-MOT pusher beam collimator and c) 3D-MOT cooling light and imaging collimators.

For the 3D-MOT beams one lens systems are implemented to attain a better wavefront quality (fig. 3.10(c)). The beam from the fiber is collimated with an one inch achromatic doublet with a focal length of 75 mm (Thorlabs AC254-075-B). To mount the optics, a one inch lens tube (Thorlabs SM1L40) is used. The lens is placed at 75 mm distance from the fiber adapter (Schäfter+Kirchhoff 10AF-4-FC+PP1020-Ti) and a collimated beam with a diameter of 18.1 mm is produced. Afterwards, the polarization of the beam is transfered to a circular one by passing through a quarter waveplate. The helicity of one of the collimators is adjusted opposite to the other three for the operation of a 3D-chip MOT (section 5.2.2). The fiber adapter, the lens and the waveplate are mounted in place inside the lens tube using retaining rings and glue. The diameter of the beam is reduced to 17.2 mm because of the retaining rings of the waveplate. Since an alignment of the two cooling beams which reflect from the chip surface is crucial for an optimum operation of the chip-MOT, these two collimators are installed on flexure mirror mounts (Siskiyou IXF1.0a). The two others are directly connected to the view ports of the 3D-MOT chamber with titanium screws. The part of these two beams, which shine on the atom-chip mount is blocked in front of the collimator to prevent stray light in the 3D-MOT chamber. Inside each collimator, a photodiode (Farnell SLSD-71N100) is placed for power monitoring. For the imaging system, two collimators similar to the 3D-collimators are constructed.

3.6 Magnetic shield

The experiment is shielded from the background magnetic field by a three-layer mu-metal shield (Magnetic shields Ltd MG8392). External magnetic fields affect the preparation process of the ultra-cold atomic ensemble by changing the center position and frequency of the magnetic traps. These fields can be compensated with the magnetic fields from the bias coils. For a transportable experiment, shielding the sensor head, saves the time required for the characterization and compensation of the environmental fields. This compensation is also necessary to obtain high accuracy in absolute gravity measurements, although the influence of the magnetic fields during the interferometry is minimized by selecting the magnetic insensitive $m_F = 0$ state.

The magnetic shield consists of three-layers cylindrical mu-metal with 1 mm thickness (fig. 3.11). The diameters of these cylinders are 474, 506 and 558 mm with heights of 853, 886 and 939 mm respectively. The shield layers sit inside a large mu-metal end cap mounted on three aluminum rods. In order to prevent the fringing effect[1], the shields are overlapped with the end cap for 100 mm. Each layer is sealed on top with a bolted plate and an access port with a 71 mm diameter provides the connection to the vacuum pump system (fig. 3.1). The weight of the three layers plus the aluminum support structure is equal to 61.2 kg. A shielding factor of 210 on the center axis of the cylinders and 820 on the radial axis is measured by the manufacturer. This is comparable with the values presented by QUANTUS-2 as a shielding factor of 117^+ on the center axis and 658^+ on the radial axis [79].

All the elements inside the magnetic shield are chosen from non-magnetic materials. The vacuum pump and sensor generate strong magnetic fields and hence are placed outside of the shield. They are connected to the vacuum chamber with a CF-connection through the top access port of the mu-metal shield. Their magnetic fields are additionally suppressed via soft-iron shields.

3.7 Vibration isolation

The retro-reflective mirror acts as the reference for the free-fall measurement of the atoms. Since all other optics are common for both interferometry beams, any phase shift due to their vibration is similar for the two beams and is canceled out. In contrast, vertical displacements of the reference mirror introduce phase noise between the two interferometry pulses. Hence, in order to achieve lower inaccuracy in gravity measurements, the reference mirror needs to be shielded from the environmental vibrations. At the current stage, the sensor head is placed on a commercially available passive vibration isolation platform with a low resonance frequency of 0.5 Hz (Minus K Technology 250BM-1). Under the mirror chamber, enough space is reserved for an additional accelerometer (fig. 3.11) to monitor the residual vibrations of the platform, which can then be post-corrected [80, 81] or actively compensated [6, 82].

1 An opening in the shield breaks the continuity of the magnetic flux path and allows magnetic fields to penetrated inside the shield. This is known as the fringing effect.

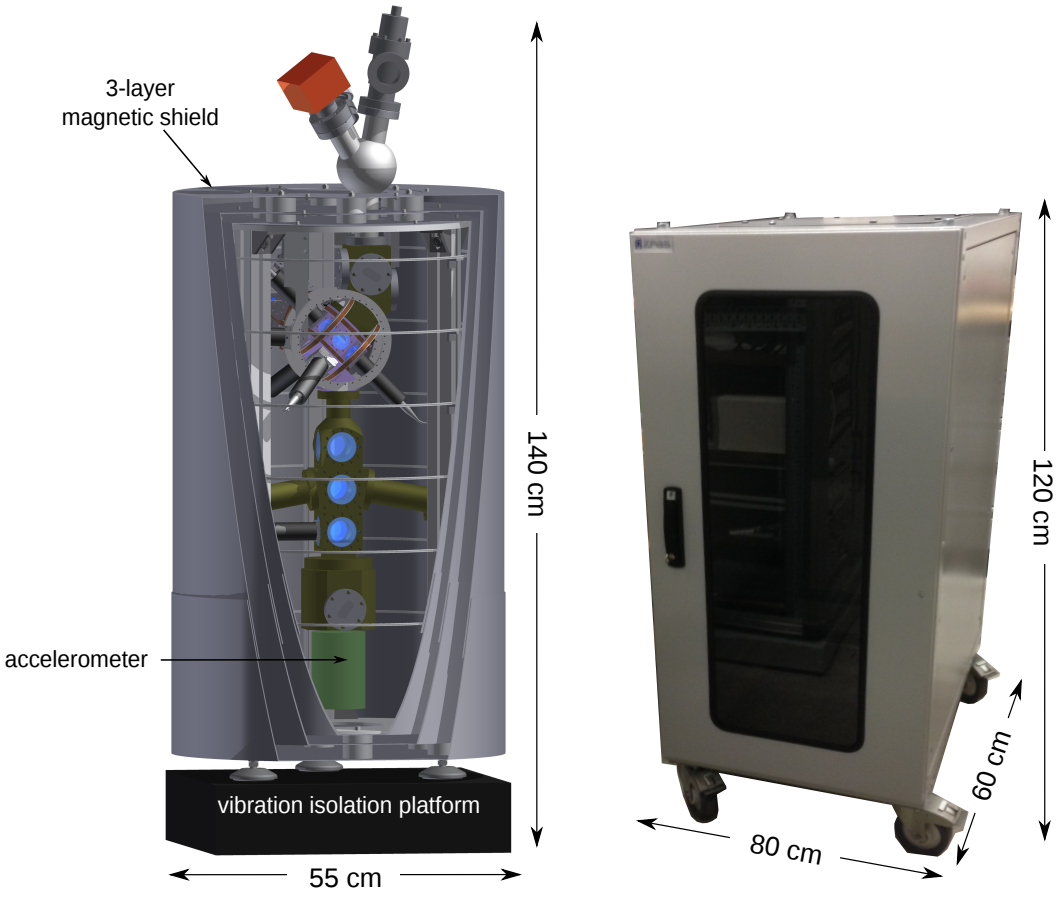

Figure 3.11: A CAD drawing of the QG-1 sensor head setup and a picture of the laser and electronic rack. The vibration isolation platform and the 3-layer magnetic shield are illustrated. The connection between the laser system and the electronics to the sensor head is provided by 10 m long PM fibers and low-loss electrical cables.

II -Laser and electronics rack

As the experiment is set up for field applications, the laser system and the electronics need to be compact, robust and easy to transport. Therefore, a compact fiber-based laser system (section 3.8) and miniaturized electronics (section 3.9) are utilized and will be mounted inside a portable rack enclosed in a robust hermetically sealed housing on wheels (ZETBOX SZE2s-127). The control rack is 19 inches wide, which corresponds to a size of 60 cm × 80 cm and includes 24 height units[1]. The rack consists of profile rails on the front and back, which are adjustable in height. The enclosure can be easily accessed from both front and back through two doors. The rack fulfills IP64 protection level of the EN60529 / IEC 529 standard. The temperature of the enclosure is stabilized via peltier cooling. For this, four peltier element cooling stages (Dr. Neumann Peltier-Technik FR-416-AC) are installed on the sides of the housing (two on each sides). The total power consumption of these four peltier elements is about 1 kW. 10 m long low-loss electrical cables and polarization maintaining low-loss fibers provide the connections from the rack to the sensor head (fig. 3.11).

3.8 Compact high power fiber-based laser system

The QG-1 laser system must provide all the required frequencies for the experiment. This includes the frequencies for the cooling of the atoms, optical molasses, optical pumping, detection and Bragg pulses. These frequencies are depicted in fig. 3.12. For an efficient cooling of the atoms, the spectral laser linewidth should be narrower than the natural linewidth of the atomic transition. This is 6.065 MHz in the case of the ^{87}Rb D_2 transition [83]. The narrow linewidth of the laser is more decisive for the case of atom interferometry using Bragg diffraction, since the laser linewidth should be narrow enough to interact with the atoms in only one momentum state. The laser system must provide a high enough light power for the cooling and manipulation of the atoms, while keeping the electrical power consumption low to be suitable for field applications. It needs to be compact and long-term stable for transportability. Free-space optics are sensitive to mechanical vibrations and temperature fluctuations, which makes them inapplicable in field. Hence, a frequency doubled fiber-based laser system is chosen in QG-1 and the amount of the free-space optics is reduced as far as possible. Fiber-based laser systems are more robust against mechanical and thermal perturbations and suffer less from misalignments in comparison to the free-space optics. They are as well more compact and require less maintenance. Furthermore, the telecommunication C-band technology at the wavelength of 1560 nm is well established and many fiber-based narrow linewidth laser diodes, high power amplifiers

1 1 height unit = 4.445 cm

and optical components in this wavelenght are commercially available [84, 85]. All these components can be interconnected with single mode PM optical fibers.

To further miniaturize and simplify the experiment, in QG-1 only one laser generates all the necessary light after a frequency doubling [86]. This laser is a pigtailed distributed feedback (DFB) diode at 1560 nm (Toptica #LD-1550-0080-DFB-1). At the current stage, the frequency of this laser is stabilized by an offset lock to a reference laser at 1560 nm. The reference laser is a pigtailed single-frequency external cavity diode laser (ECDL) at 1560 nm in a butterfly housing (Thorlabs SFL-19388). The frequency of this laser is stabilized in reference to a rubidium atomic transition by a modulation transfer spectroscopy (MTS) scheme [87] after a frequency doubling (section 3.8.1). The offset lock allows a tunability of the laser frequency from a few MHz up to 2 GHz after doubling by changing the offset frequency. With this, the DFB laser frequency is stabilized close to the $5^2S_{1/2}, F = 2 \rightarrow 5^2P_{3/2}, F' = 3$ transition of ^{87}Rb and is tuned to provide the required frequencies for the cooling, optical pumping, detection and blow-away (see fig. 3.12). The repumping light frequency is provided from the sidebands of the phase modulation of this laser light by a fiber-based electro optic modulator (EOM) (EOspace PM-0K5-10-PFA-PFA-UL) (section 3.8.2). This fiber-coupled EOM allows modulation of up to 10 GHz with less than 3 dB loss. The required repumping frequency has to be calculated with respect to the cooling transition. This gives a frequency difference of about 6.5 GHz, which depends on the cooling light detuning. The frequency and amplitude of the sidebands can be tuned by the frequency and power of the input signal to this EOM. This input signal is provided by a phase-locked loop circuit described in section 3.9.2. The light frequencies for the interferometry are generated by an acousto optic modulator (AOM) as it is described in section 3.8.2.

After a reliable operation of the laser system is demonstrated, the frequency stabilization will be performed with sideband modulation technique with an EOM [89]. For this purpose, a branch of the light from the DFB laser will be referenced to the rubidium transition. This light will be modulated with a high bandwidth fiber-coupled EOM (iXBlue Photonics MPZ-LN-40), which can generate up to 40 GHz sidebands. When one of the higher-order sidebands is stabilized on the atomic transition, the carrier frequency can be tuned by changing the modulation frequency. Employing the carrier as the Bragg beam splitters, their frequency detuning from the atomic transition can be increased to several GHz. This is an advantage, since it lowers the rate of residual spontaneous decays. Furthermore, higher-order-Bragg diffraction is desirable in QG-1, because the sensitivity of an interferometer is proportional to the momentum transfer during the atom-light interaction [51, 90]. To increase the transition probability to higher orders, higher light intensities are required [45], which as well increases the probability of spontaneous emissions. Hence, larger detuning from the atomic transition is more crucial in this case. In this method, the requirement of an additional laser as the reference laser is excluded, which helps in further simplification and miniaturization.

Detailed descriptions on the development and frequency stabilization of the laser system, as well as the tests on the high bandwidth EOM for the single laser operation scheme can be found in [91]. Therefore, in this document only a brief summary of the architecture and current state of the experiment is presented. A schematic of the laser system is illustrated

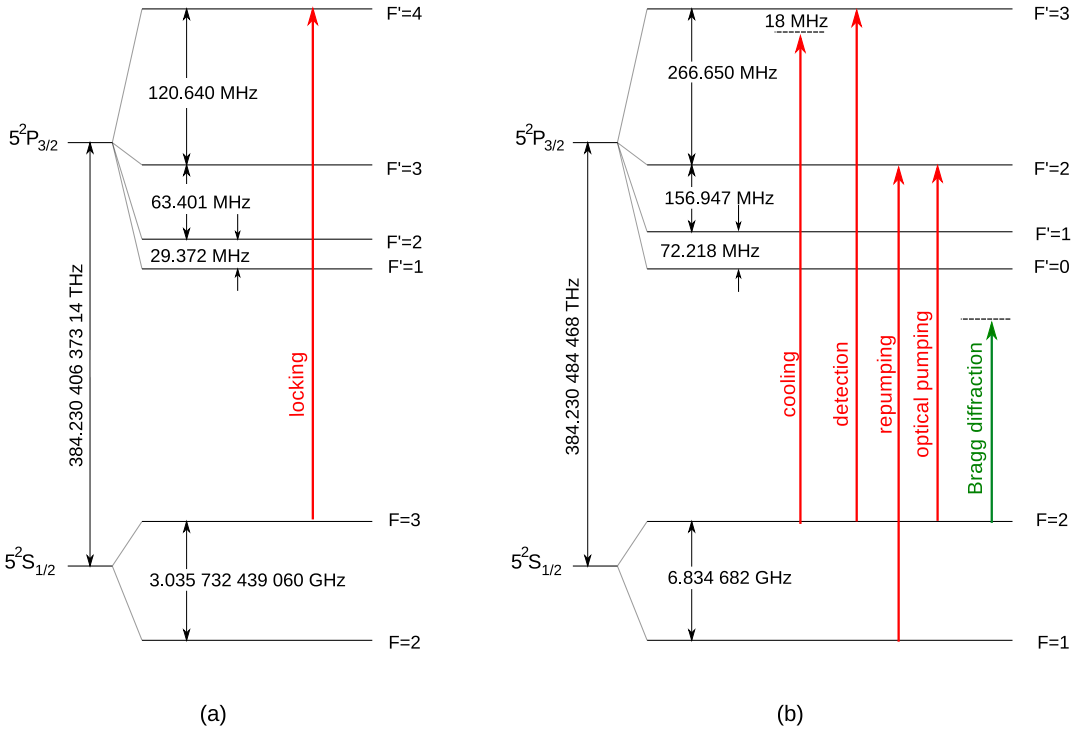

Figure 3.12: The ^{85}Rb (a) and ^{87}Rb (b) D_2-line hyperfine structure and the required laser frequencies in the experiment are presented. The given frequency values are adopted from [88] and [83].

in fig. 3.13. In the following, each part will be briefly described.

3.8.1 Reference Module

In order to provide a stable reference for the optical frequencies in the experiment, a reference laser is actively frequency stabilized on a ^{85}Rb transition in a modulation transfer spectroscopy (MTS) setup [92]. The experiment laser can be phase-locked to this reference laser and its offset frequency can be adjusted. In MTS, the frequency of a pump beam is modulated by a frequency modulating device, that is an EOM or AOM. This modulated beam overlaps with a counter-propagating probe beam inside a rubidium gas cell and generates sidebands in this beam via a four-wave mixing process [93]. This process occurs only when the sub-Doppler resonance condition is fulfilled and therefore, a flat zero background signal is provided. With this, the zero crossing of the MTS signal is not shifted from the atomic transition. The ^{85}Rb D_2 transition $F = 3 \rightarrow F' = 4$ is chosen, because the closed transitions lead to the strongest modulation transfer signals. This generates a clear signal for the laser frequency stabilization even when the excited state hyperfine splittings are closely spaced to each other [94]. Because of the two above mentioned advantages of MTS over the other known frequency stabilization techniques, it

is chosen in the QG-1 experiment. A pigtailed external cavity single-frequency laser in a butterfly housing (Thorlabs SFL-19388) is used as the reference laser. This laser generates a 1560 nm light and its instantaneous linewidth is measured to be 80 kHz [91]. The light power from this laser is about 40 mW. This light is transferred with a single mode PM fiber to an optical isolator (Thorlabs IO-G-1550-APC). Afterwards, it is split by a PM 99 : 1 fiber coupler (Thorlabs PN1550R1A2). The one percent output is used for the frequency stabilization of the DFB laser [91]. The output port with the major light power is first frequency doubled by a periodically poled lithium niobate (PPLN) waveguide mixer (HC Photonics 1WM156048H10108NCP001) before entering the reference module to stabilize the frequency of the reference laser to the atomic transition (see fig. 3.13 and 3.14). An EOM (New Focus 4001NF) is employed to modulate the pump beam by 7 MHz. The rf input for this EOM is provided from the frequency control board after an amplification with an rf amplifier (Mini Circuits ZHL-32A-S+). The probe beam signal is detected with a fast photodiode (Thorlabs SM05PD2B), who's signal is then amplified (Mini Circuits ZX60-14012L-S+) and is demodulated in the control electronics (see fig. 3.13). This signal is used to lock the laser frequency to the atomic transition. More details can be found in [91]. The reference module is assembled on a honeycomb aluminum breadboard and has a dimension of 29.5 cm × 10.5 cm × 8.5 cm.

3.8.2 Distribution module

A distributed feedback (DFB) diode at telecom frequency of 1560 nm (Toptica #LD-1550-0080-DFB-1) is employed as the single laser of the experiment. The intrinsic linewidth stated by the manufacturer is smaller than 200 kHz at 1560 nm. This is measured in the experiment as 579.2 kHz by a series of beat note measurements [91]. The 1560 nm output light is guided through a single mode PM fiber to a polarization maintaining 50 : 50 fiber coupler (Toptica PMC-P-2x2-1550-50/50-3-4FC/APCx4-90x14x8.5-1M). One of the output ports is used for the offset lock to the reference laser (see fig. 3.13). The other output is first phase modulated by a fiber-coupled EOM (EOspace PM-0K5-10-PFA-PFA-UL) for the generation of the repumper frequency. Afterwards, it is attenuated by 20 dB using a fiber coupled attenuator (keopsys) before entering the erbium-doped fiber amplifier (Keopsys CEFA-C-PB-HP-PM-42-NL1-0M1-B301-FA-FA), who's maximum input power lays at 0 dBm. The fiber amplifier creates saturated output power of up to 42 dBm while maintaining the polarization and narrow linewidth of the input light. This provides an output light power of 15 W at a wavelength of 1560 nm. Its total electric power consumption is up to 350 W based on the datasheet and uses about 110 W during the operation of the experiment. This fiber amplifier is mountable in the experiment's control rack consuming three height units and can be controlled via RS232/USB interface. The output light of the amplifier is guided with a single mode PM optical fiber into the second harmonic generation (SHG) module mounted on the distribution board (see fig. 3.14). Here, its frequency is doubled by passing through a PPLN bulk crystal in a single pass configuration. An output light power of up to 3.2 W at 780 nm is generated. The fundamental wavelength is reflected from two filters onto a beam dump attached to the housing of the SHG module. The second harmonic beam and its modulated wavelengths generated by the EOM enter the distribution module.

The distribution module is assembled on a honeycomb breadboard with customized and miniaturized free-space optic components, a beam height of 2 cm and a total dimension of 40 cm × 27.5 cm × 10.5 cm (fig. 3.14). In this module, the total light power is divided into several paths and its frequency is further manipulated using AOMs (Opto-Electronic MT80-A1,5-IR, AA) to generate the required light frequency for each purpose. The AOMs are used for frequency modulation in a range of few MHz as well as fast switching of the lights during the experimental sequence. Additionally, in front of each fiber input, a mechanical bistable shutter (UniBlitz TS6B) is installed to thoroughly block the remaining light. This prevents the entry of stray light into the fibers. The beam is divided into three main paths, each including an AOM. The first order of the AOM in the first path (shown in blue in fig. 3.14) is divided and guided into three fiber collimators (Schäfter+Kirchhoff60FC-F-4-M5-10) meant for the 2D-cooling and two detecting lights. Before each fiber coupler, a $\lambda/2$ waveplate adjusts the polarization of the light to one of the principal axes of the fiber. The output light for the $2D^+$-MOT (output 3) enters a 1 : 4 fiber coupler (section 3.8.3), which guides the light into two transverse collimators and the pusher collimator (section 3.2.1). The two other outputs (outputs 1 and 2) are coupled into 10 m fibers and are guided to the sensor head. One of them provides the light for the detection of the atomic ensemble in the 3D-MOT chamber and the second one is guided to the bottom of the interferometry tube and will be used for the detection of the atoms after the interferometry sequence. The second main path (shown in red in fig. 3.14) is guided into two fiber couplers. One (port 5) is meant for the 3D-cooling light. A 1 : 4 fiber beam splitter (section 3.8.3) divides this beam into four beams with equal powers and guides them to the 3D-collimators (section 3.2.4). The other port (port 6) is meant as a pick up light for monitoring or comparison purposes. The last main path is for the Bragg-interferometry (shown in green in fig. 3.14). The frequency difference between the two interferometry beams in a Bragg-type atom interferometer is in an order of several kHz up to a few MHz. Therefore, they both can be generated with one single AOM, on which two different acoustic frequencies are applied simultaneously. This light is then coupled into a 10 m PM fiber which guides the interferometry beams to the collimator. In this way, all the optics on the path of the two interferometry beams, except the reference mirror, are common and their phase noise is suppressed.

In each of the three main paths, a photodiode (Farnell SLSD-71N500) is installed behind an unused output of a polarizing beam splitter (PBS). In this way, the fluctuations in the power and polarization of the laser light can be monitored.

3.8.3 Fiber splitters

The laser light is guided from the laser system to the sensor head through 10 m PM optical fibers. A 1 : 4 PM fiber beam splitter (OZ-Optics FOBS-14P-11111-5/125-PPPPP-780-45/45/7/3) divides the beam from output 3 of the distribution module (fig. 3.14) into four paths. The output power distribution of 45/45/7/3 is specified by the company. This is measured as 44.15%, 44.9%, 7.3% and 3.6% in the experiment. The two ports with the higher power are used as the 2D-transverse beams. The port with 7.3% of the total output power is used merely for monitoring purpose. The last port, with the least output power is used for pushing and retarding in the $2D^+$-MOT. The input fiber of the coupler is chosen

with a length of 10 m and the output fibers are 1 m long each.

For the operation of the mirror-MOT, four laser beams with equal power and frequency are required. Therefore, the light for the 3D-MOT is distributed by a $1:4$ spliceless PM evanescent coupler (Evanescent Optics Inc.). This fiber splitter is chosen, because spliceless coupler arrays provide a low loss and high polarization isolation. The input fiber is 10 m long with 3 mm diameter sleeving. The four output fibers are 1 m long each with only 900 μm sleeving in order to be lighter in the weight. The output powers are measured as 25.1%, 26.0%, 25.8% and 23.2% of the total output power at each port. Both fiber splitters will be mounted on the aluminum support of the sensor head.

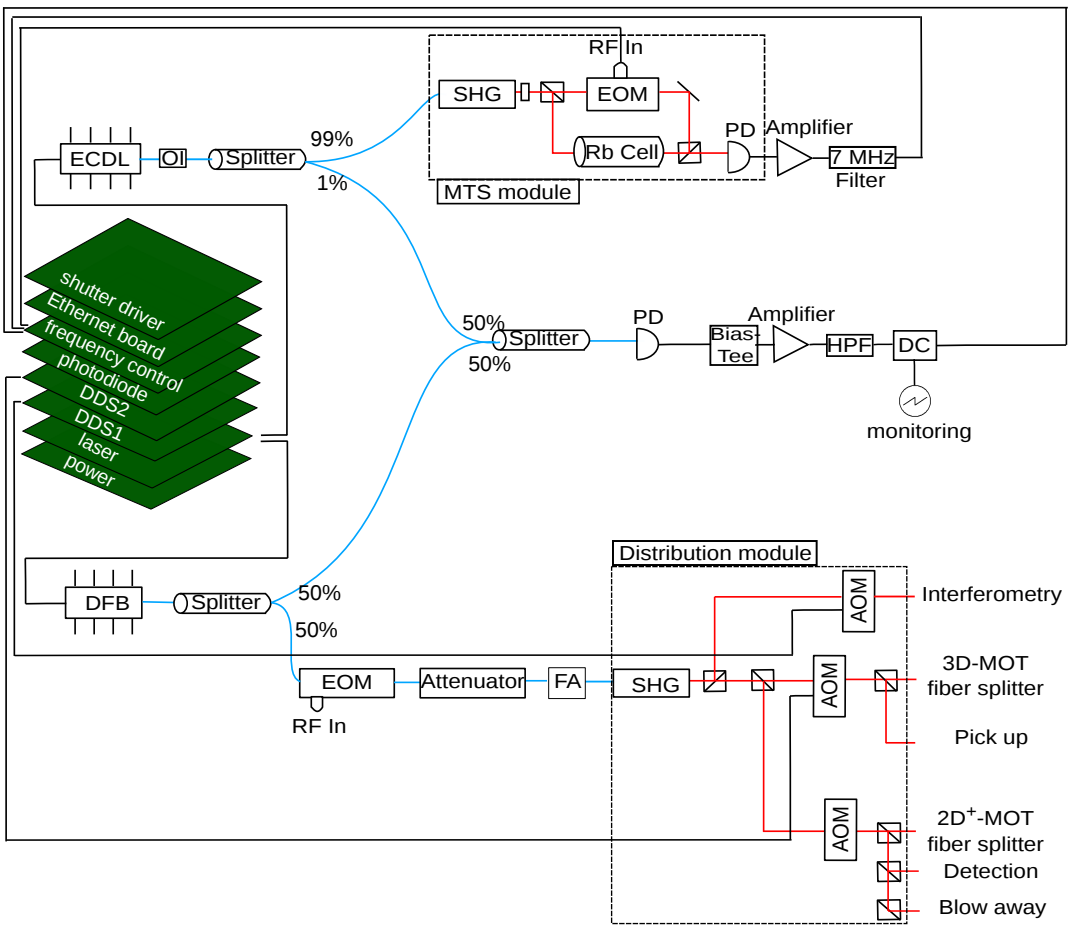

Figure 3.13: A schematic of the complete laser system in QG-1 and its control electronics. The reference laser passes through an optical isolator (OI) before it splits into two paths. The major power is guided to the reference module for stabilization of the laser frequency on the rubidium transition. This part is presented in the upper part of the schematic and is described in section 3.8.1. The other path, shown in the middle of the image, is used for frequency stabilization of the experiment laser. Here, the lights from both lasers superimpose on a fiber coupled photodiode (PD). This beat signal is processed by a bias tee and an amplifier. After passing through a high pass filter (HPF), it is divided into two parts via a directional coupler (DC). One part of the signal is sent to the frequency control board for the frequency stabilization and the second part is used for monitoring. Further description on the operation is found in [91]. The experiment laser is a DFB diode. Its light is divided into two paths with equal powers. One is used for its offset lock to the reference laser. The second path is distributed into different fibers after the amplification with the fiber amplifier (FA) and frequency doubling in the SHG module (section 3.8.2). These fibers are guided to the sensor head through PM optical fibers. The control stack of the laser includes 8 cards, which are briefly described in section 3.9.1. The blue lines depict the fiber-coupled light at 1560 nm, the red lines show the free-space beams at 780 nm and the black lines are the electrical connections. This picture is adopted and updated from [91].

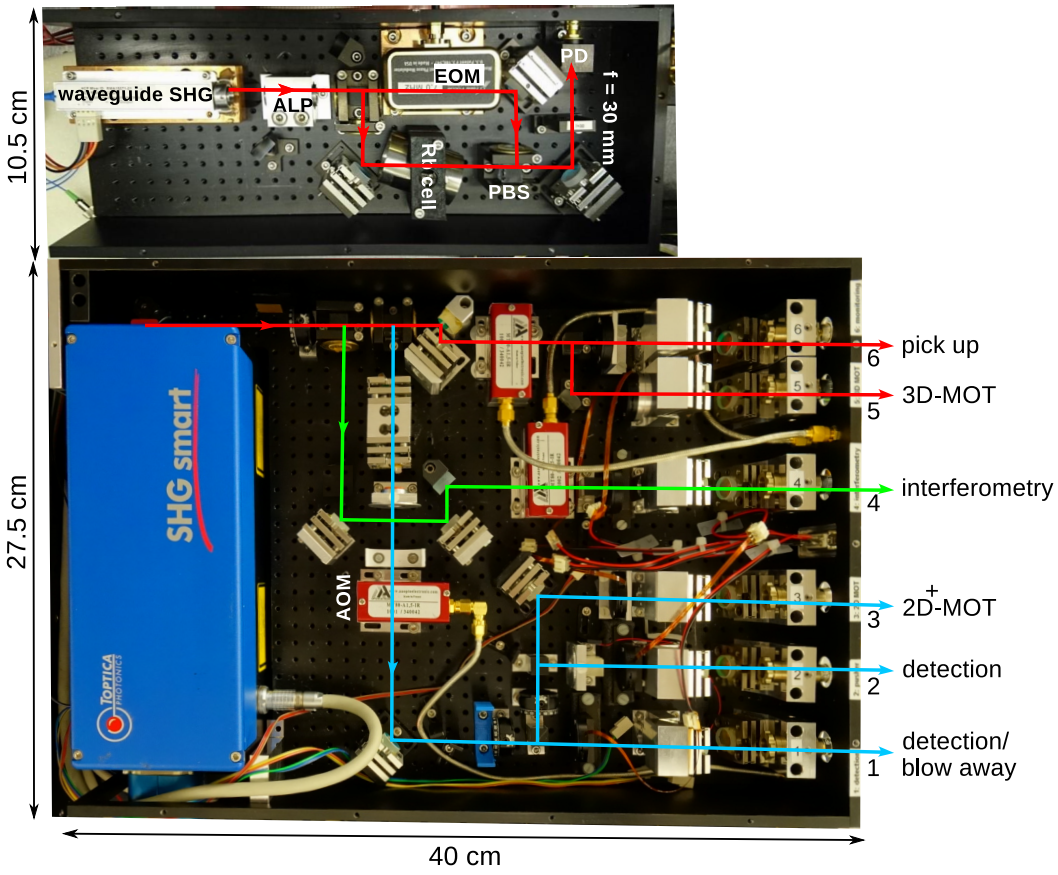

Figure 3.14: A picture of the laser system. The upper part shows the reference module. The laser light from the ECDL enters this module and its frequency is doubled by a waveguide SHG. This light is then collimated in an afocal lens pair (ALP) and splits into pump and probe beams via a polarizing beam splitter (PBS). The frequency of the pump beam is modulated at 7 MHz in an EOM. The probe beam is focused on a fast photodiode (PD). Full description on the reference module is found in section 3.8.1. The lower part of the picture demonstrates the distribution module, in which the light from the DFB diode is frequency doubled and divided into the necessary paths for the experiment. This module is described in section 3.8.2. This laser system fits in one 19 inch rack shelve and will occupy three height unit of the experiment's rack.

3.9 Electronics

The electronic system of a transportable apparatus requires to be compact and consume low amount of electric power. The control electronics of the laser system and the current drivers are based on a bus system developed in the framework of the QUANTUS collaboration and is known as the TBus system [95, 96]. The hardware consists of 10 cm × 10 cm electronic boards stacked on each other and connected via pin arrays. In QG-1, two electronic stacks, one for the laser system control (section 3.9.1) and one for the generation of the required magnetic fields (section 3.9.3), are utilized. The experimental sequence is timed by a computer control system programmed in a virtual instrumentation (VI) software (National Instruments LabVIEW) and a field programmable gate array (FPGA) (National Instruments NI USB-7855R FPGA) with digital trigger-lines and analog input and outputs [97]. The communication between the two electronic stacks and the computer control system is realized by Ethernet interfaces. The clocks of both stacks are synchronized to the FPGA clock. The output of the current drivers are connected to the so-called chip safety boards [72] before the connection to the coils and chip structures. The chip safety boards provide the safety of these structures by allowing the flow of a current with a maximum set value for a limited set time after receiving a trigger signal from the computer control system. They additionally provide a readout of the flowing currents. This is further described in section 3.9.3.

The temperature of the two lasers and the two doubling stage modules are controlled and stabilized using four commercial thermoelectric temperature controllers (Meerstetter Engineering miniature precision peltier temperature controller TEC-1091). This is based on a proportional-integral-derivative (PID) regulation concept. Temperatures of the reference laser, DFB laser, waveguide SHG of the reference module and the SHG crystal of the distribution module are stabilized at 32.1°C, 40.8°C, 44.9°C and 39.5°C respectively. These four circuit boards are mounted via pin headers on one homebuilt power distribution board, of which the serial connection to the computer is provided via a programmable embedded processor module (XPort Lantronix) using RS485 protocol. The temperature regulation and optimization is done using the control software provided by the manufacturer. Monitoring of the temperatures is integrated in the computer control system of the experiment. Two of these distribution boards fit inside a 13 cm × 11.5 cm × 18 cm box fitting in a 19 inch rack-mount enclosure. With this, all the four temperature controllers for the laser system together with the two for the rubidium reservoir and valve are fitting inside one box. The electrical connection of each two temperature controller boards is provided by one HD15 connector on the front panel of the enclosure.

In order to mount the electronic system inside the experiment's rack (section 3.7), two 19 inch rack-mount enclosures with 4 height units are employed. Since the high electric power of some of the components leads to heating of the electronic system, the temperature of the transportable rack is stabilized using four peltier element cooling stages.

3.9.1 Control electronics and frequency stabilization

The laser stack includes the following circuit boards, which are developed in the QUANTUS collaboration [95]. Further description of the function of each board can be found in [91].

Power supply card provides the required voltages for the stacks and a monitoring of these voltages. It is connected to two low noise laboratory power supplies (Hameg HMP4040), which provide the electric power for the laser and the current driver stack (section 3.9.3).

Laser current driver card has two outputs for generation and stabilization of the currents of the reference laser and the DFB laser.

DDS cards - Each direct digital synthesizer (DDS) card contains two output channels. The frequency, phase and amplitude of the output signals can be jumped or swept. Two DDS cards are assembled in the control electronic stack of QG-1. Three channels control the frequencies of the AOMs in the 2D-, 3D- and the interferometry paths. The last output is used as the reference frequency for the phase-locked loop (PLL) used to control the repumper frequency (section 3.9.2).

Frequency control card provides the frequency stabilization of the laser system. The details on the process of the frequency stabilization from the signals obtained by the photodiode in the reference module and the beat photodiode is described in [91]. The feedback signal is sent to the laser current driver card through the TBus pins.

Photodiode card provides a monitoring of the voltages of the photodiodes in each collimator and inside the distribution module. This is used to monitor the fluctuations in the light power and polarization.

Shutter driver card is designed in the frame of this experiment [98] for a fast operation of 6 bistable shutters to be compatible with the TBus electronics. It uses the trigger lines of the stack for its operation and can provide a switching with a frequency of 20 Hz.

Ethernet card provides the connection of the stack to the computer control system.

The schematic of the laser stack is depicted in fig. 3.13 and its total height is equal to 16.5 cm.

3.9.2 Control over the repumper frequency

Since the cooling transition of ^{87}Rb is not fully closed, during the cooling process, atoms get lost from the cycle by decaying to the F = 1 ground state. Hence, for an efficient cooling process, a repumping light on resonance with the D_2 transition $F = 1 \rightarrow F' = 2$ is necessary (fig. 3.12). This frequency is generated from the phase modulation of the DFB laser via a fiber-coupled EOM (section 3.8). In order to keep the repumping frequency on resonance while changing the cooling frequency, a control over the modulation frequency is required. During the experimental sequence, the red-detuning of the cooling light from the D_2 transition $F = 2 \rightarrow F' = 3$ is changed from -18 MHz for the 3D-MOT (section 5.2.2) to -150 MHz for the polarizatin gradient cooling (section 5.3). Therefore, a control over the repumper frequency in this range is necessary. The rf input to the EOM is produced by a phase-locked loop (PLL) (Analog Devices HMC834LP6GE) integrated on a circuit board designed in the institute [99]. The frequency output of this PLL is controlled by a reference frequency generated from the DDS card on the laser stack (section 3.9.1).

With this, the repumper frequency can be tuned up to 162.4 MHz without changing the frequency of the voltage controlled oscillator (VCO) in the PLL. The frequency of the VCO is set by a microcontroller board (Arduino Due), which communicates with the computer through a USB cable. Hence, a change in its frequency requires about 1 s time and is not feasible during one experiment cycle. Due to this reason, a change in the repumper frequency beyond the aforementioned range of 162.4 MHz during one cycle is not possible. For the optical state preparation in QG-1, the cooling light is employed and its frequency is set on resonance with the $F = 2 \rightarrow F' = 2$ transition (section 5.4.1). In order for the repumper light to stay on resonance with the $F = 1 \rightarrow F' = 2$ transition during the whole cycle, a change of 248.6 MHz in the modulation frequency of the EOM is required from the 3D-MOT step to this step. Consequently, the optical state preparation during the work of this thesis is performed without the repumping light. The control over the VCO frequency will be implemented in the computer control system in the near future.

The optimum input power to the EOM is measured to be 2.7 dBm (section 5.2.2). After passing through two +10 dB amplifier and one −7 dB attenuator (Mini-Ciruits), The rf power is equal to 2.6 dBm. During the absorption imaging, the repumper light should be switched off. For this, the input voltage required for the amplification of the signal is switched off with a field-effect transistor (FET) switch (Onsemi BS170). This is controlled by the analog output of the NI USB FPGA. The rf power drops to −20 dBm when the FET switch is open. With this, a stable and switchable repumping frequency is realized.

3.9.3 Magnet field current drivers

The current drivers of the magnetic field generating structures must be compact and produce high currents while consuming low electric power. Their switching should be fast in order to trap a higher number of atoms in a shorter period of time. Additionally, they are required to have a low noise level, since a noise in the electric current of the chip structures or coils leads to fluctuations in the trapping frequencies. This causes heating of the trapped atoms and therefore shortens the trap lifetime [100]. The closer the atomic sample is to the field generating structures, the bigger the effect of the electric current noise in the lifetime of the trapped atoms would be. Hence, this is more critical for the case of the chip current drivers. The current drivers are designed in the frame of the QUANTUS collaboration to be compatible with the TBus system [96]. These cards are 10 cm × 10 cm circuit boards stackable on the TBus. Each chip current driver card includes two galvanically isolated channels, which provide up to 10 A unipolar currents. Each coil current driver card includes one bipolar current source with −5 A to +5 A output current. Both chip and coil current drivers contain a so-called power board, which provides a temperature readout and an emergency shutdown of the current when the circuit's temperature is above a set critical value of 60°C. They both permit jumps and linear ramps for the current and their background noise level is measured below 1 μA in 1 s [96].

PID regulators are employed to make the switching in between of different values of output currents faster. Chip current drivers can switch in less than 150 μs. In the case of the coils, the high inductance of the structure increases the switching time. Therefore, the regulation coefficients should be adjusted for each coil depending on its inductance to avoid oscillations in the output current and lower the switching time. This can be set by soldering

the proper electronic components for the PID regulator. The corresponding switching time can be simulated using a simulation program with integrated circuit emphasis (SPICE) software (TINA-TI) [96]. Graph 3.15 illustrates an example of the result of this simulation and compares it to the measurement performed in the experiment. This is repeated for all the coil current drivers. In table 3.3, the maximum measured switching time in each structure is presented. The measured inductance of each coil can be seen in table 3.2.

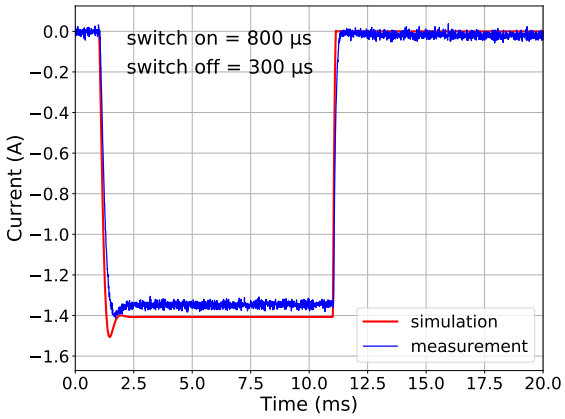

Figure 3.15: The switching time of the current in the Z-coil in the case of a jump to −1.4 A. The red line is the result of the simulation and the blue line is measured in the experiment.

Table 3.3: Maximum switching time of the current in different structures in QG-1.

Current driver	Max measured switch time
Chip structure	150 µs
2D-coils	1.4 ms
Small 3D-coils	300 µs
3D-coils	1.5 ms

The current driver stack in QG-1 consists of two chip and six coil current driver cards. One chip current driver card is used for the mesoscopic H- and U-structure and the second one for the base and science chip. The six coil current driver cards provide the current for the 2D-, x-, y-, z-, small x- and small y-coils. These cards together with a TBus power supply card and an Ethernet card form the current driver stack. The power supply card is connected to the laboratory power supplies of the laser stack (section 3.9.1). Another two low noise power supplies (Hameg HMP4040) are used to provide the input power for the current drivers. The experimental sequence can be sent to the stack from the computer control system via Ethernet interface [97].

In between of the current drivers and the coils or chip structures, the chip safety boards are installed. Each board contains four channels. The circuit closes by a trigger signal from the control system and the current can flow. After a certain set time or when the current exceeds a maximum set value, the circuit channel opens. The maximum time is set to 8 s for the coils and the mesoscopic U-structure, since they are used in the 3D-MOT step. The

current flow in the mesocopic H, base and science chip is limited to 3 s. Maximum allowed current is limited to 7 A for the coils, 10 A for the mesoscopic structure, 6.3 A for the base and 2.7 A for the science chip. The communication between the chip safety boards and the computer control system is established via the NI USB FPGA. These boards together with the current driver stack and the box, which provides the connection between the chip safety board and the NI USB FPGA are mounted inside a 19 inch enclosure to be placed inside the portable rack (section 3.7).

3.9.4 Power supplies and power consumption

Low noise power supplies provide the required powers for the laser and current driver stacks. These stacks consume about 43 W of power while the experiment is running. Typical power consumption of the fiber amplifier is about 110 W during the operation of the experiment. Two other low noise power supplies provide the input power for the coil and chip current drivers. Six power channels are required to drive the temperature controllers, the amplifiers for the AOMs and EOMs, the chip safety boards, the amplifiers for the input signal to the fiber-coupled EOM and the Light induced atom desorption (LIAD) circuits. The maximum power is consumed by the peltier element cooling stages for the rack with a total nominal power of about 1 kW. With this, the total power consumption would be around 1.4 kW when the experiment is running. The power supplies will fit inside the portable rack and will be connected with one power cord to a main supply.

CHAPTER 4

Imaging system

For the characterization and optimization of an atomic ensemble, the observation of several properties including its temperature, density, size and shape is necessary. Hence, before discussing the experimental realization of the trapped atoms in the next chapter, a description of the imaging system and its characterizations is provided. Two imaging techniques are employed in QG-1. One is based on the absorption of a near-resonance probe beam, the so-called absorption imaging (section 4.1) and the second is based on the spontaneous re-emission of this absorbed light, known as the fluorescence imaging (section 4.3). The fluorescence imaging system is mounted on the 3D-MOT chamber (fig. 3.9) and is more suitable for obtaining information about the atom number, loading rate and lifetime of the 3D-MOT as well as the velocity and flux of the atomic beam loaded from the $2D^+$-MOT. By absorption imaging, the size, shape, position, density distribution and the atom number in the atomic cloud can be determined. The temperature of the atomic ensemble is acquired from the expansion rate of the cloud (fig. 5.14). With the combination of these two imaging systems, different steps of atom cooling in QG-1 are characterized.

4.1 Absorption Detection

The image of a collimated probe beam passing through an atomic ensemble is used to deduce information about this atomic cloud. The attenuation of the probe beam's intensity along the beam axis (z') is calculated from the Beer-Lambert law

$$\frac{dI}{dz'} = -n(x',y',z')\sigma I. \tag{4.1}$$

Here, n is the local density, (x', y', z') is the camera coordinate system, such that z' is parallel to the detection beam pointing towards the atoms and σ is the scattering cross section given by [83]

$$\sigma = \frac{\sigma_0}{1 + 4\left(\frac{\delta}{\Gamma}\right)^2 + \frac{I}{I_{sat}}} \tag{4.2}$$

where $\sigma_0 = \hbar\omega\Gamma/(2I_{sat})$ is the on-resonance cross section, δ is the detuning of the probe beam from resonance, $\Gamma = 2\pi \,.\, 6.065\,\mathrm{MHz}$ is the natural linewidth of the transition and I_{sat} is the saturation intensity and is equal to $1.669\,\mathrm{mW/cm^2}$ for a circularly polarized

light on resonance with the D_2 transition $|F = 2, m_F = \pm 2 > \rightarrow |F' = 3, m'_F = \pm 3 >$ of ^{87}Rb [83]. Integrating eq. (4.1), the column density of atoms along the direction of the probe beam is given as

$$n(x',y') = \int n(x',y',z')dz' = \frac{1 + 4\left(\frac{\sigma}{\Gamma}\right)^2}{\sigma_0} \ln\left(\frac{I_i}{I_f}\right) + \frac{I_i - I_f}{\sigma_0 I_{sat}}. \tag{4.3}$$

Here, I_i is the initial intensity of the probe beam and I_f is the beam intensity after passing through the atomic ensemble. In the experiment, these intensities are deduced from taking one image of the beam without the atoms (I_{beam}) and one with the atoms (I_{atoms}). In order to reduce the noise from the background light, a third image is taken with no beam and no atoms ($I_{background}$), which will be subtracted from both images:

$$\begin{aligned} I_i &= I_{beam} - I_{background} \\ I_f &= I_{atoms} - I_{background} \end{aligned} \tag{4.4}$$

The light from the detection collimators (fig. 3.10(c)) with a beam diameter of 17.2 mm is employed as the imaging beam. After passing through the center of the 3D-MOT chamber, this beam is collected on a CCD camera (PCO AG pco.1400). The part of the beam which would hit the chip edge is blocked on the collimator to avert stray light in the chamber. The CCD sensor has a resolution of 1392×1040 pixels with a pixel size of $6.45\,\mu\text{m} \times 6.45\,\mu\text{m}$. The manufacturer specifications provide a quantum efficiency of 15% at 780 nm.

At the current stage, two absorption imaging setups are mounted on the 3D-MOT chamber. The first one (fig. 4.1(a)) is built and characterized for BEC imaging within the work of a bachelor thesis [101] and is referred to as the detection system 1. This system is based on an optimized achromatic lens pair (Thorlabs MAP1075150-B). Achromatic pairs combine two achromatic doublets, which are placed at a certain distance from each other by the manufacturer to minimize the aberrations. In the case of this system, the focal lengths are $f_1 = 75$ mm on the side of the atoms and $f_2 = 150$ mm on the side of the camera. Since the achromatic lenses are so close to each other, they act as a single lens with a combined focal length of 50 mm ($\frac{1}{f} = \frac{1}{f_1} + \frac{1}{f_2}$). Therefore, the distance from the atoms to the first lens is set to 50 mm. With a 150 mm distance between the CCD camera and the second lens, a magnification factor of 2 will be obtained:

$$d_{\text{image}} = (M + 1)f. \tag{4.5}$$

Here, M is the magnification factor and f is the focal length of the lens. The CCD chip has a size of 8.9 mm × 6.7 mm and hence, with a magnification factor of 2 the effective field of view (FOV) will be equal to 4.45 mm × 3.35 mm. Using a resolution test chart (USFA 1951), this system is characterized and an optical resolution of 7.82 μm at the position of the atoms is measured [101].

Since the FOV of the first imaging system is not large enough for the characterization of the laser cooled atoms, a second absorption imaging setup (fig. 4.1(b)) is built and

is temporarily assembled on the 3D-MOT chamber. This is referred to as the detection system 2 and is mounted to the chamber at a 45° angle to the x- and y-axes (fig. 3.9). With the combination of these two detection systems, a three-dimensional spatial information of the atomic ensemble is available. In this system, a one lens telescope is implemented. A best form lens (Thorlabs LBF254-050-B) with a focal length of 50 mm is mounted inside an adjustable one inch tube (Thorlabs SM1). The lens is placed at a 150 mm distance from the atoms and 75 mm from the CCD camera. With this, a magnification factor of 0.5 will be attained. The effective FOV of this system is therefore 17.9 mm × 13.4 mm. A second detection collimator, similar to the first one (fig. 3.10(c)) is constructed for this imaging system. Since the beam size in comparison to the FOV is small, an apodizing ND filter (Thorlabs NDY10A) is added to the front of the collimator to flatten the Gaussian beam's intensity profile. With this, a more homogeneous intensity in the beam area is obtained, which improves the image quality. Both of the imaging systems are attached to the chamber in the way that the x´-axis of the camera is the z-axis of the chip coordinate system, showing the distance of the atomic ensemble from the chip surface.

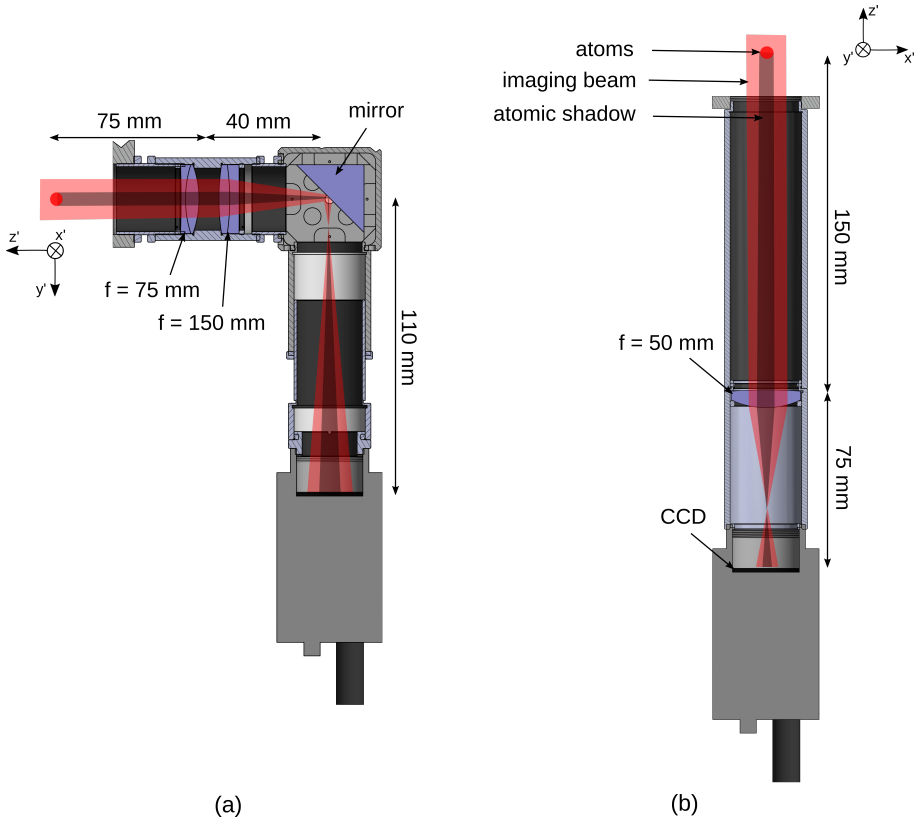

Figure 4.1: CAD drawing of the two absorption imaging telescopes: a) Detection system 1 mounted on the 3D-MOT chamber parallel to the x-axis (z´ = -x). b) Detection system 2 attached to the chamber forming a 45° angle with the x- and y-axes (z´ = +x - +y). With the combination of these two setups, a three-dimensional spatial information of the atomic ensemble is available. The camera coordinate system is shown on the image. x´= z in the case of both cameras, showing the distance of the atomic ensemble to the chip surface.

4.2 Characterization of the detection system

Some optimizations were required in order to reduce the noise level of the image and obtain a more accurate atom number. The detection light power and its exposure time are optimized for the cloud densities in a laser cooled (section 5.3) and magnetically trapped (section 5.4.2) atoms. This is done using the signal-to-noise-ratio (SNR) of the image as the parameter to evaluate the image quality. For this, the power and duration of the pulse are scanned and the parameters which result in the highest SNR are chosen as the optimum. Figure 4.2 illustrates an example of the result of this scan and shows that a light pulse with a duration of 80 to 100 μs and a power of 40 to 110 μW will result in the highest SNR. The proper values can be chosen from this range depending on the density of the atomic cloud. Switching the detection light is performed using an AOM instead of the exposure time of the camera in order to reach more accurate timings. The detection pulse power is as well controlled with this AOM.

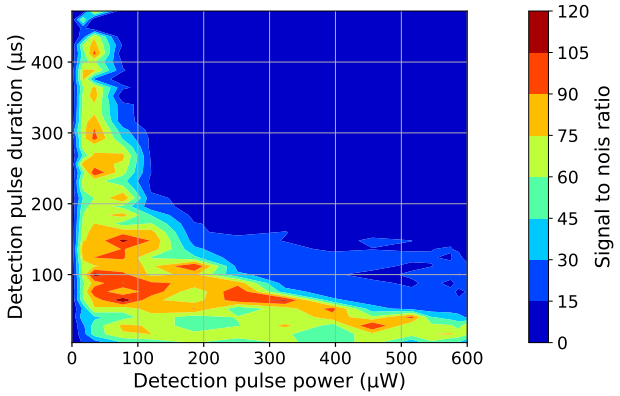

Figure 4.2: An example of the optimization of the detection pulse power and duration for the absorption imaging of the atomic cloud after the PGC stage. The SNR of the image is observed at different intensities and durations of the detection light. The result shows that a 100 μW pulse shined on the atoms for 80 μs can be chosen to achieve a high image quality. This light power corresponds to an intensity of 43 μW/cm^2.

The probe light is on resonance with $5^2S_{1/2}, F = 2 \rightarrow 5^2P_{3/2}, F' = 3$ transition of ^{87}Rb (fig. 3.12) and has a circular polarization. In order to calculate the correct atom number, a quantization field of 4.33 Gauss is applied parallel to the detection beam to induce σ^+ transitions. $|F = 2, m_F = +2> \rightarrow |F' = 3, m'_F = +3>$ is a closed transition and therefore, after a few cycles all the atoms are pumped into the $|F = 2, m_F = +2>$ Zeeman state. The quantization field is generated by the 3D-Helmholtz coils. Detection system 1 is installed parallel to the x-axis and therefore, this field is generated by -0.56 A current in the x-coils. The appropriate quantization field for the detection system 2, is provided by the combination of equal strength fields with a magnitude of -3.06 Gauss from the x- and y-coils. This is applied via -0.40 A current in the x-coils and -0.52 A in the y-coils. The coil currents are switched on 1 ms before the light pulse, compatible with their rise time duration (table 3.3). To confirm the laser frequency experimentally, the number of atoms in the ensemble is monitored while scanning the detection light frequency over the

resonance. The result of this scan for the detection system 2 is shown in fig. 4.3. The calculated frequency shifts of σ^+ transitions due to the Zeeman effect, $|\mathrm{F} = 2, m_F = i>$ $(i = -2, -1, 0, +1 \,\text{and}\, +2) \rightarrow |\mathrm{F}' = 3, m'_F = j>$ $(j = -1, 0, +1, +2 \,\text{and}\, +3)$ are shown in red lines, which are equal to 2, 3, 4, 5 and 6 MHz for this applied quantization field.

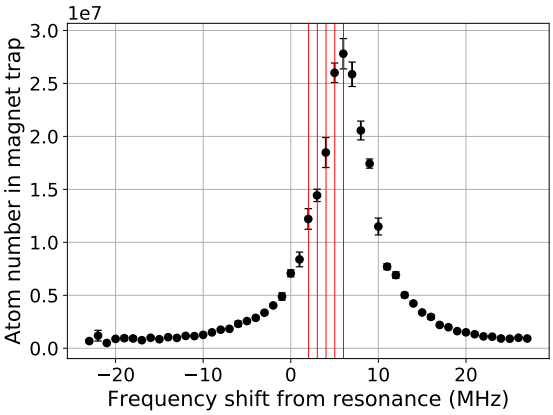

Figure 4.3: Characterization of the resonance frequency of the detection beam for the absorption imaging. This plot is taken from the detection system 2 with a quantization field of 4.33 Gauss and is averaged over 3 sets of measurement. The calculated frequency shifts of the transitions due to the Zeeman effect are shown with the red lines.

The magnification factor of each system is verified through a free-fall measurement of the atomic ensemble. Comparing the resulting accelerations from a polynomial fit to the free-fall trajectory of the atoms with the expected acceleration results in the magnification factor. This measurement is depicted for both systems in fig. 4.4. The free fall of the atoms from a magnetic trap is used in the case of the detection system 1 and a magnification factor of 1.94 is measured (fig. 4.4(a)). Since the FOV of the second detection system is large enough, the free fall of atoms from a laser cooled ensemble after the PGC stage can be used for this measurement. The magnification factor of this system is measured as 0.5 (fig. 4.4(b)).

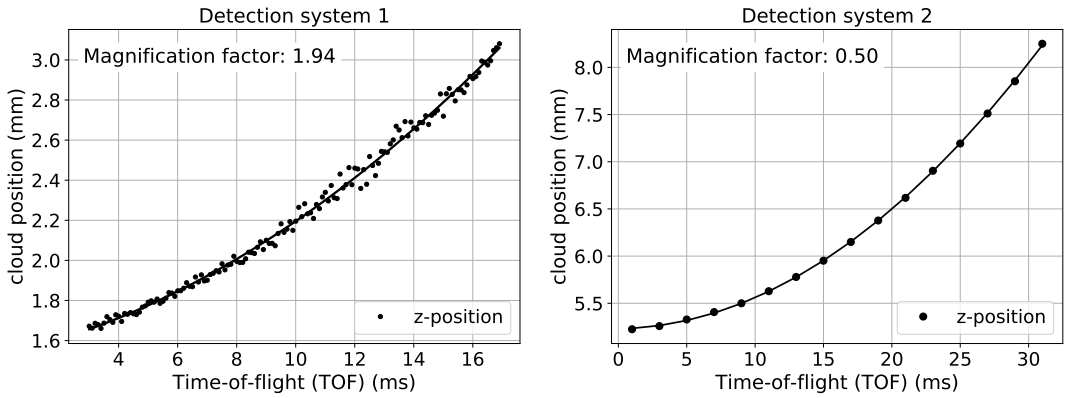

(a) **(b)**

Figure 4.4: Measurement of the magnification factor of the detection systems. The position of the atomic cloud is imaged after different free expansion times. Comparing the falling acceleration taken from the fit on the trajectory of the free-falling atoms to the expected gravitational acceleration, the magnification factor of the imaging system is extracted. These plots are an average over 3 sets of measurement.

4.3 Fluorescence imaging

In addition to the absorption imaging, the experiment is equipped with a fluorescence imaging system, which is mounted on the big view port of the 3D-MOT chamber opposite to the atom chip (fig. 3.9). Fluorescence detection is a suitable tool for fast diagnoses of the 3D-MOT. It provides a simple way for observation of the loading rate and lifetime of the 3D-MOT during the optimization and alignment process. The re-emitted radiation by the atoms that have absorbed the cooling light is collected on a large area photodiode (Thorlabs SM1PD1B). However, since the 3D-MOT light is detuned from the resonance, it is preferable to use an on resonance light from the detection collimator to acquire a more consistent atom number.

A double-lens telescope is set up inside a lens tube (Thorblas SM30L30) to focus the light on the photodiode (fig. 4.5). The first lens is an achromatic doublet (Thorlabs AC300-080-B) with f = 80 mm and is placed with its focal point on the atoms. The second lens is another achromatic doublet (Thorlabs AC300-050-B) with f = 50 mm and is placed with its focal point on the photodiode. The lenses are fixed in place using retaining rings, leading to a clear aperture of 27.9 mm. The acquired photo current from the photodiode enters a variable gain low noise current amplifier (FEMTO DLCPA-200). This device translates the photo current to a voltage and amplifies the signal by a factor of G, which can be set using the computer control system in a range of 10^3 to 10^{11} V/A.

Atom number from the fluorescence signal is calculated from

$$N = \frac{4\pi\ S_F}{S\ G\ d\Omega\ R_{Sc}\ \hbar\omega}. \tag{4.6}$$

Here, S_F is the voltage of the signal acquired from the FEMTO amplifier, S is the sensitivity

of the photodiode equal to 0.55 A/W at 780 nm, G is the gain factor of the amplifier, $d\Omega$ is the solid angle of the lens equal to 0.108 sr in this case (fig. 4.5), $\hbar\omega$ is the energy of one photon and R_{Sc} is the total photon scattering rate given by [83]

$$R_{sc} = \left(\frac{\Gamma}{2}\right) \frac{(I/I_{sat})^2}{1 + 4(\delta/\Gamma)^2 + (I/I_{sat})} \tag{4.7}$$

where Γ is the natural linewidth of the transition, δ is detuning of the probe beam from the resonance, I is the light intensity of the probe beam and I_{sat} is the saturation intensity. The reflection of the fluorescent light from the atom chip is as well collected on the photodiode, which has to be considered in the atom number calculation. The distance between the position of the atoms to the chip surface is equal to 4 mm. Therefore, the solid angle of the reflecting photons is equal to $d\Omega' = 0.088$ sr. With an output voltage of S_d from the photodiode, the real fluorescence signal emitted from the atoms can be calculated from

$$S_F = \frac{S_d d\Omega}{d\Omega + d\Omega'}. \tag{4.8}$$

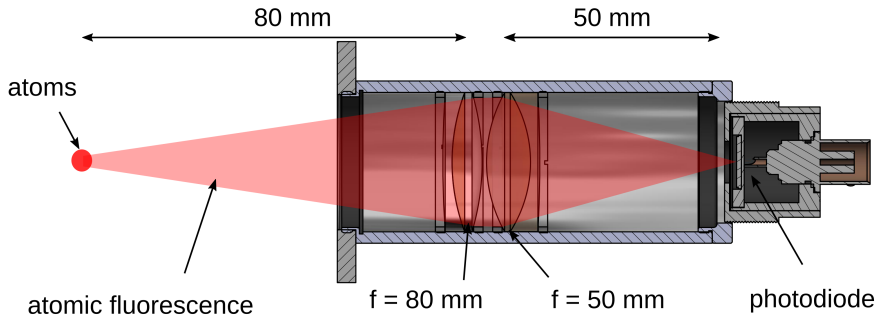

Figure 4.5: CAD drawing of the fluorescent imaging telescope installed on the 3D-MOT chamber.

The two presented absorption imaging systems and the fluorescence imaging setup installed on the 3D-MOT chamber are used to characterize and optimize the steps of cooling and trapping the atoms in this thesis.

CHAPTER 5

Realization and characterization of the atomic source

In this chapter the experimental sequence of cooling the atoms in a MOT and trapping them inside a magnetic trap generated by the wire structures on the atom-chip assembly is described. The characterization of each step as well as their optimal parameters is presented. The ultimate target is establishing a source for matter-wave interferometry for the purpose of gravity measurement with a 0.5 Hz repetition rate. For this, a large number of atoms should be trapped and cooled to quantum degeneracy within a short time (section 2.2). In addition to the high-flux requirement, the experimental apparatus for the generation of this atomic source needs to be compact for portability. These two conditions are met by cooling the atomic cloud in a two-stage MOT [56] on an atom chip [102]. A large number of atoms is trapped from the background gas and cooled in two dimensions in the $2D^+$-MOT chamber. The generated high-flux atomic beam is guided into the center of the 3D-MOT chamber through the pumping stage. Here, the atoms are trapped in the 3D-chip-MOT where the cooling beams overlap at the center of a quadrupole field. This field is created by the mesoscopic U-structure of the atom chip in combination with the bias field of the coils [55]. The UHV environment of the 3D-MOT chamber leads to a long lifetime of atoms inside the 3D-MOT and the following magnetic trap. The atom chip is placed inside the vacuum chamber in close distance to the atoms. This allows reaching higher trap frequencies over smaller volumes with lower power consumption in comparison to a magnetic field merely generated by coils outside of the vacuum chamber. Also, the considerably lower inductance of these structures, leads to much faster switching times. These properties make an atom chip a very suitable device for generation of a high-flux BEC in a compact setup [69]. The atom-chip assembly of QG-1 consists of three layers with different structure sizes (fig. 5.1). This allows a sequential compression of the trapped atoms. The atoms can be first confined further away from the chip surface in a larger volume magnetic trap produced by larger structures of the mesoscopic and base layers. Afterwards, they can be transferred to the final magnetic trap closer to the chip surface generated by the smaller wire structures of the science chip. With this consecutive compression, a large number of atoms can be confined in the final high frequency magnetic trap. From here, the atoms can be evaporatively cooled to the critical temperature for BEC. The wire structure of the atom-chip assembly used in each step as well as the required bias field from the Helmholtz coils is illustrated in fig. 5.1.

In the following, the consecutive steps in reaching the quantum degeneracy is described in details.

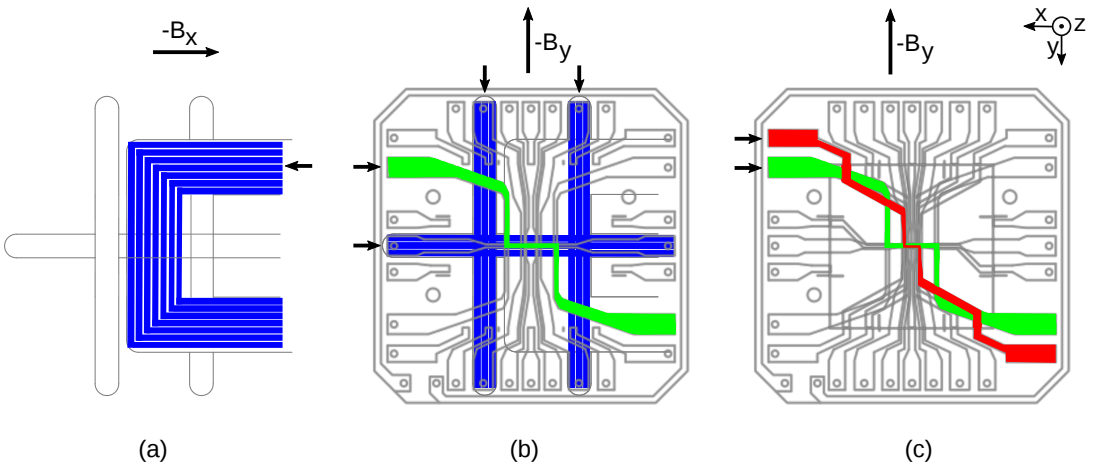

Figure 5.1: The chip structures and bias fields used to create the quadrupole field for the U-MOT (a) and the Ioffe-Pritchard fields for the initial magnetic trap (b) and the final magnetic trap (c). The black arrows indicate the direction of the electric current in the chip structure. The bias field for the quadrupole trap is generated from a negative current in the x-coils and for the Ioffe-Pirtchard trap from a negative current in the y-coils. The chip coordinate system is illustrated and is described in section 3.4.1.

5.1 Rubidium source

A one gram rubidium ampule heated to a certain temperature is used as the atomic source for the experiment. The setup is described in section 3.2.2. By varying the temperature, the rubidium vapor pressure inside the $2D^+$-MOT chamber can be adjusted. At low pressures, the atomic beam flux rises linearly with the pressure. Increasing the vapor pressure further, increases the collision rate of the cold atoms in the beam with the hot background atoms and decreases the atomic beam flux [57]. Therefore, an optimum rubidium pressure should be realized. Furthermore, high rubidium vapor pressures in the $2D^+$-MOT chamber can lead to a chemical reaction of the rubidium atoms with the indium sealing of the vacuum windows. Hence, the temperature of the oven should be raised very carefully, while the rubidium vapor pressure in the $2D^+$-MOT chamber is monitored. For the purpose of this measurement, an absorption spectroscopy is employed [103]. Here, the reflection of one of the two transverse cooling beams from the mirror coating of the optics on the opposite window is collected on a photodiode (S5106, Hamamatsu Photonics). A picture of the setup can be seen in fig. 5.3(a). A detailed description of the setup is provided in the master thesis in [91]. The frequency of the cooling laser is stabilized with respect to the reference laser and scanned over the absorption frequencies of ^{85}Rb and ^{87}Rb. An example of the observed Doppler-free saturated absorption signal[1] [103] on the photodiode is shown in fig. 5.2. In the beginning, the temperature of the rubidium reservoir is increased very slowly

1 The choice of a saturation absorption spectroscopy is not necessary and is made because of the geometry of the setup as can be seen in fig. 5.3 .

from the room temperature until the initial signal appeared. Further heating is stopped at 26.5°C. At later stages, this temperature has been increased further to 28.5°C in order to attain more rubidium atoms in the MOT. At this point, the temperature of the valve connecting the reservoir to the $2D^+$-MOT chamber is set to a slightly higher temperature of 30°C in order to prevent condensation of rubidium atoms in this section. The partial pressure of rubidium in the $2D^+$-MOT chamber is calculated from this absorption signal and the ideal gas law, $P = \frac{N}{V} k_B T$, where k_B is the Boltzmann constant. The atom number per volume (N/V) is derived from the intensity attenuation of the probe light after traveling through the width of the chamber twice before being absorbed on the photodiode [104]

$$\frac{N}{V} = -\frac{6\sqrt{2}\,\Delta\omega_D}{\sqrt{\pi}\,z\,\sigma_0\,\Gamma}\left(\ln\left(\frac{I_z}{I_0}\right) + 2\frac{I_z - I_0}{I_{sat}}\right). \tag{5.1}$$

In the above formula, σ_0 is the on-resonance cross section, Γ is the natural linewidth of the transition, I_0 is the intensity of the light entered the chamber, I_z is the intensity of the light after travelling the length of z and I_{sat} is the saturation intensity. $\Delta\omega_D = \omega_0\sqrt{(8k_BT\ln 2)/(mc^2)}$ is the Doppler broadening of the spectral line, where ω_0 is the rest frequency and m is the mass of ^{87}Rb atoms. The values for σ_0, Γ and I_{sat} are provided in section 4.1. The length that the light has travelled in the chamber, z, is twice the width of the $2D^+$-MOT chamber and therefore equal to 8.2 cm. The intensity of the absorbed light is estimated via a Gaussian fit on the absorbed signal as shown in fig. 5.2. With this, the vapor pressure of rubidium gas in the $2D^+$-MOT chamber is estimated to be 7.2×10^{-7} mbar, which matches to the value presented in [83] at this temperature.

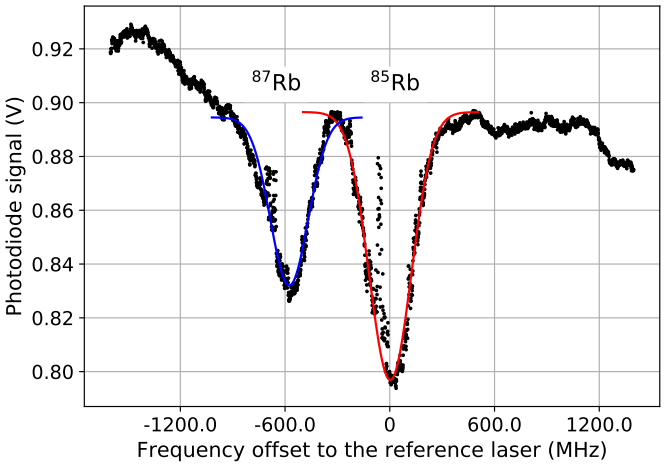

Figure 5.2: Doppler-free saturated absorption spectrum in the 2D$^+$-MOT chamber. The frequency of the cooling laser is stabilized with respect to the reference laser and is scanned over the D_2 cooling transition of ^{85}Rb and ^{87}Rb. The frequency of the reference laser itself is stabilized to the D_2 $F = 3 \rightarrow F' = 4$ transition of ^{85}Rb as described in section 3.8.1. This signal is collected on a photodiode mounted on one of the 2D-transverse beam collimators (fig. 5.3) and is used for the measurement of the rubidium partial pressure in the 2D$^+$-MOT chamber. This plot is an average over 20 single spectrum scans. The vapor pressure is estimated at 7.2×10^{-7} mbar.

5.2 Magneto-optical trapping of neutral atoms

For the initial cooling and trapping of a sample of atoms usually a MOT is utilized. Counter-propagating near-resonance red-detuned laser beams with opposite circular polarizations are employed along the three dimensions. This leads to the Doppler cooling [58] via which the atomic sample can be cooled down to temperatures of a few hundred μK. Adding a magnetic field with linear gradient additionally leads to the spatial trapping of these cooled atoms. The trapping field is usually a magnetic quadrupole field generated by a pair of Helmholtz coils. For an optimal cooling process, the cooling light should be a few MHz red-detuned from a closed atomic transition. In this case, each absorption of a photon is always followed by a spontaneous emission back to the initial state and so the atoms stay in the cooling cycle. For this reason, the cooling process of the ^{87}Rb atoms is carried out on the D_2 transition $F = 2 \rightarrow F' = 3$. This light is provided from the laser system as it is described in section 3.8. All the required beam frequencies are summarized in fig. 3.12(b). Since the upper hyperfine splitting of ^{87}Rb D_2 transition is not large enough to avoid $F = 2 \rightarrow F' = 2$ transitions, an inevitable excitation to the unwanted upper hyperfine states occurs from where spontaneous decays to the $F = 1$ state is possible. The $F = 1$ hyperfine state is dark to the cooling beam and therefore these atoms will be lost from the cooling cycle. To prevent this, a second beam on resonance with the D_2 transition $F = 1 \rightarrow F' = 2$ is required to optically repump these atoms and bring them back to the the cooling cycle. The repumping light in QG-1 is generated from the sidebands of a phase modulation of the cooling laser with a fiber-coupled EOM as it is described in section 3.8.

The force exerted on the atoms from the MOT beams in one dimension is given by

$$\vec{F} = \vec{F}_+ + \vec{F}_-, \tag{5.2a}$$

$$\vec{F}_\pm = \pm\hbar\vec{k}\,\frac{\Gamma}{2}\,\frac{I/I_{sat}}{1 + I/I_{sat} + (2\delta_\pm/\Gamma)^2}, \tag{5.2b}$$

where $+/-$ refers to the beam in the positive or negative direction of the beam axes and the effective detuning $\delta_\pm$ is

$$\delta_\pm = \delta \mp \vec{k}.\vec{v} \pm \mu' B/\hbar. \tag{5.3}$$

Here, δ is the laser detuning from the resonance of the transition, $\vec{k}$ is the photon wave vector, $\vec{v}$ is the velocity of the atoms, B is the amplitude of the magnetic field at the position of the atoms and μ' is the effective magnetic moment for the transition and is equal to $\mu' = (5/6)\mu_B$ for the cooling line of ^{87}Rb [58], where μ_B is the Bohr magneton.

Equation 5.2 represents that the MOT force depends on the magnetic field gradient and the detuning and intensity of the cooling light. All these parameters change the shape of the MOT force profile and can affect the atom number, temperature and density of the atomic cloud and hence their optimum parameters should be found. Since the optimum detuning of the cooling light from the resonance depends on the Zeeman splitting of the atomic sublevels, which changes with the magnetic field, the detuning of the cooling light needs to be adjusted accordingly when the magnetic field gradient is changing. Coupled parameters like this make optimization of the MOT a multi-dimensional search for the optimal flux, instead of being able to tune each parameter individually. In the following, the process of this optimizing in the QG-1 experiment is described.

5.2.1 2D$^+$-MOT

This chapter covers the characterization and optimization of the 2D$^+$-MOT in QG-1. The goal is to produce a cold atomic beam with the highest possible flux while keeping the velocity of the atoms in this beam lower than the capture velocity of the 3D-MOT[1]. The atomic beam flux is proportional to the number of atoms in the beam and their longitudinal velocity, which can be increased by improving the number of transversally cooled and compressed atoms in the 2D$^+$-MOT.

In a 2D-MOT, two counter-propagating cooling beams together with a two-dimensional quadrupole magnetic field generated from two pairs of coils in a racetrack configuration are used to cool and trap the atoms in two dimension from the background vapor. In a 2D$^+$-MOT, a molasses cooling is added in the longitudinal axis by including an extra pair of beams, the so-called pusher and retarder beams, counter-propagating to each other on this axis [56, 105]. This reduces the mean longitudinal velocity and the width of the longitudinal velocity distribution in the atomic beam and thus enhances the capture of atoms inside the 3D-MOT. Additionally, this reduction of the atomic longitudinal velocity

1 The capture velocity of the 3D-MOT is defined as the highest velocity that an atom can have when it is passing across the MOT volume to be still captured inside the trap.

makes them spend more time in the transverse cooling beams area and therefore leads to a reduction in their transverse velocity distribution as well. This increases the number of atoms passing through the pumping stage. A shadow is formed in the middle of the retarder beam due to the hole at the center of the pumping stage, which allows the atoms at the middle of the beam passing through. The configuration of the 2D$^+$-MOT chamber in QG-1 is illustrated in fig. 5.3. With the double beam configuration of the transverse cooling lights, the cooling area is enhanced to be able to captured more atoms from the background vapor.

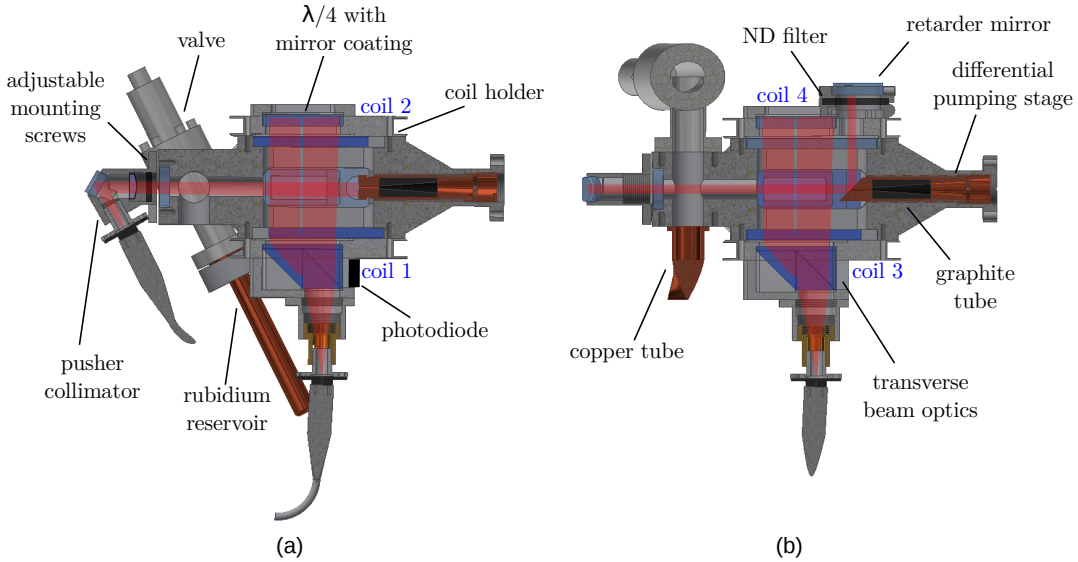

Figure 5.3: CAD drawing of the 2D$^+$-MOT chamber as well as the differential pumping stage. The sectional views from two perpendicular axes are illustrated showing the optical elements (section 3.5.1) and magnetic coils (section 3.4.2). The coil numbers are labeled on the picture and the light beams are shown in red.

For the measurement of the atomic beam flux, its fluorescence in the 3D-MOT chamber is collected on a photodiode. As the probe beam for this measurement, an on resonance laser beam shined at 90° angle to the atomic beam is used. The setup for this measurement is illustrated in fig. 5.4(a). The flux of the cold atomic beam in the detection volume is proportional to the magnitude of the collected signal on the photodiode S_F [57]:

$$\Phi = \frac{4\pi S_F < v_z >}{SGd\Omega L_P R_{sc} \hbar\omega} \tag{5.4}$$

where S_F is the photodiode voltage with sensitivity S and amplification G. $< v_z >$ is the mean longitudinal velocity of the atoms, $d\Omega$ is the detection solid angle, L_P is the diameter of the probe beam, indicating the length that the atomic beam is in the detection beam, R_{sc} is the photon scattering rate of individual atoms (eq. (4.7)) and $\hbar\omega$ is the energy of one photon. For this measurement, one of the detection collimators (section 3.5.1) with 17.2 mm

beam diameter is mounted on one of the view ports of the 3D-MOT chamber which forms a 90° angle to the atomic beam and its frequency is scanned over the resonance frequency of cooling transition so that the whole longitudinal velocity distribution is addressed.

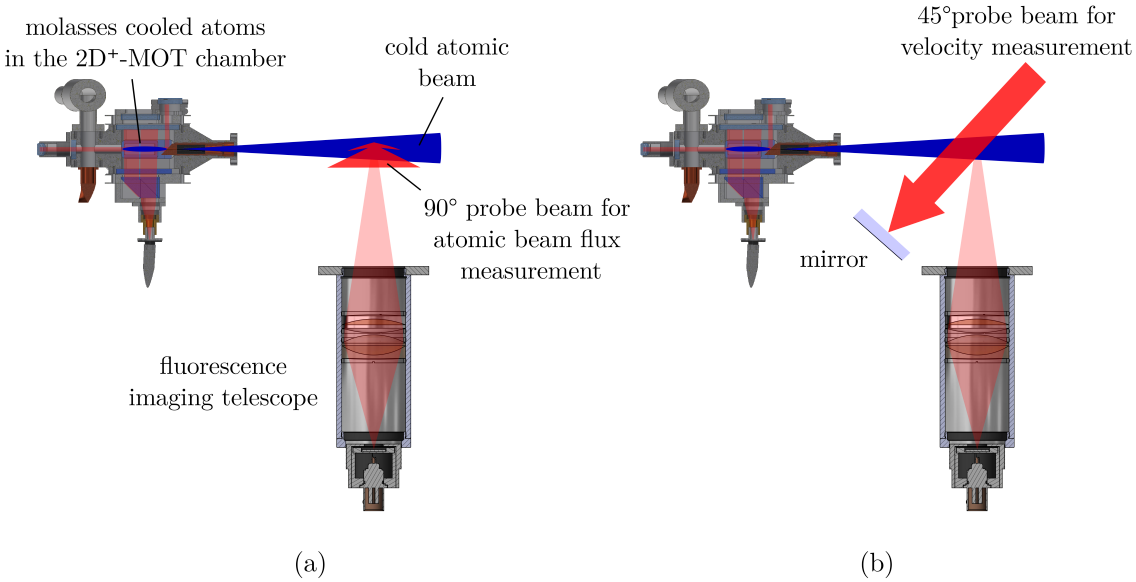

Figure 5.4: The setup for the characterization of the cold atomic beam. a) An on resonance probe beam shining at 90° angle to the atomic beam is used for the measurement of the atomic beam flux. b) For the measurement of the longitudinal velocity and the longitudinal velocity distribution of the cold atomic beam, a retro-reflecting on resonance probe beam mounted at a 45° angle to the atomic beam is used.

The mean longitudinal velocity $< v_z >$ and the longitudinal velocity distribution of the cold atomic beam are measured by mounting the probe beam at a 45° angle with respect to the atomic beam and retro-reflecting it from a broadband mirror. The setup for this measurement is shown in fig. 5.4(b). Due to the Doppler effect, while scanning the frequency of the probe beam over the resonance, two different velocity classes are addressed by the beam itself and by its reflection. This forms two peaks in the fluorescence signal, which appear symmetrically on both sides of the resonance. An example of this signal can be seen in fig. 5.5. From the frequency difference between these two peaks, the mean longitudinal velocity of the atoms can be determined [57]:

$$< v_z >= \frac{\Delta\nu\lambda}{cos\theta}. \tag{5.5}$$

Here, $\Delta\nu$ is the Doppler shift which is half of the frequency difference between the peaks, λ is the probe laser wavelength and θ is the angle between the probe beam and the atomic beam, which is 45° in this case. The longitudinal velocity distribution is determined from the broadening of the Doppler profile subtracting the natural linewidth of the transition. The longitudinal components of the radiation pressure exerted on the atoms from these two beams are in opposite directions. In the case of one of the beams, it pushes the atoms out

of the probe beam area and results in a smaller peak with a broader velocity distribution (right peak in fig. 5.5), while for the other beam it adds further molasses cooling in the longitudinal axis and holds them longer in the area of the probe beam. This results in the larger and narrower peak (left peak in fig. 5.5). The frequency of the probe laser needs to be scanned over the resonance frequency in a range of several MHz. Since the cooling laser has to be kept on a constant detuning from the transition to maintain the atomic flux of the $2D^+$-MOT, a second laser is required. An external cavity diode laser (ECDL) amplified by a tapered amplifier (TA) [106, 107] is used for this purpose. The frequency of this laser is stabilized through an offset lock on the 0th order of the AOM of the cooling laser. With this method, the velocity of the atomic beam is measured at $17.2 \pm 0.2\,\mathrm{m/s}$ with a longitudinal velocity distribution of $2.2 \pm 0.8\,\mathrm{m/s}$. This beam velocity is less than the capturing velocity of the 3D-MOT, which lies approximately at $30\,\mathrm{m/s}$ [79].

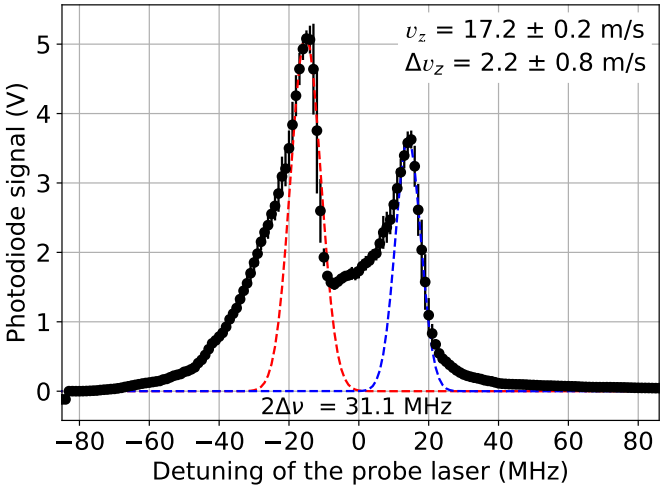

Figure 5.5: An example of the fluorescence signal detected for the velocity measurement of the atomic beam. The velocity is calculated from the Doppler shift, which is half the distance between the two peaks. The longitudinal velocity distribution can be determined from the broadening of this Doppler profile subtracting the natural linewidth of transition.

Having this tool, the atomic beam flux can be optimized by scanning the $2D^+$-MOT parameters. The 2D-quadrupole field and the laser beams for the transverse cooling should be adjusted such that a better alignment of the atomic beam with respect to the aperture of the pumping stage can be gained. The retro-reflection configuration of the transverse cooling beams (fig. 5.3) leads to an intensity imbalance between the counter-propagating lights, which needs to be compensated by balancing the electric current in the 2D-coils. For this, two of the neighboring coils called coils 2 and 4 in the experiment (fig. 5.3) are connected in series and their electric currents are kept similar to each other. At each certain current of this pair of coils, the currents in the two other coils, coil 1 and 3, are scanned independently. By this, the center of the quadrupole trap can be adjusted for the highest 2D-atomic beam flux. An example of this scan is shown in fig. 5.6(a). This process is repeated for different currents of coils 2 and 4 in order to find the optimum magnetic field gradient. When the magnetic field gradient is changing, the detuning of the

cooling light needs to be changed correspondingly (section 5.2). Therefore, at each electric current composition, the light detuning is scanned as well. The result of this scan for three different magnetic field gradients is illustrated in fig. 5.6(b). Plot 5.6(c) summarizes the result of this four-dimensional scan. It shows the dependence of the atomic beam flux and its velocity on the magnetic field gradient. Each point in this graph, represents the highest flux reached at a certain current in the pair of coils 2 and 4. The best cooling light detuning and the resulted atomic beam velocity for each data point is illustrated on the graph. The optimum magnetic field gradient is found from fitting a polynomial function on the measurement points as $\vec{\nabla}B = 19.8\,\mathrm{G/cm}$. The optimum cooling light detuning is $-18\,\mathrm{MHz}$ at this magnetic field. Such field is produced with 2.95 A in coils 2 and 4 [1]. Figure 5.6(a) shows the dependence of the atomic beam flux on the currents in coils 1 and 3 while the current in the pair of coils 2 and 4 is equal to 3 A. Since the dependency of the beam flux on the coil currents is not following a symmetric model, the optimum values of these currents are found from a two-dimensional Spline interpolation on the data points. From here, the correct proportion of the electric currents in the 2D-coils is established. This results in

$$\begin{aligned} I_1 &= 1.06\ I_{2and4} \\ I_3 &= 1.03\ I_{2and4} \end{aligned} \tag{5.6}$$

A voltage divider circuit is made afterwards to provide the correct electric current for the 2D-coils from one single programmable power supply.

Rising the intensity of the transverse cooling light broadens the atomic spectral lines and therefore atoms with higher velocities can be captured for a fixed light detuning. Higher light intensity additionally results in a steeper MOT potential and further compression of the atomic beam. This leads to an improvement of the atomic flux [57]. Since high light power is available in the QG-1 laser system, the transverse light power is kept at 100 mW per collimator which is equivalent to an intensity of $24.8\,\mathrm{mW/cm^2}$. Increasing the beam intensity to this value has shown an increase in the atomic beam flux almost linearly. Through the intensity of the pusher and retarder beams, the longitudinal velocity and the longitudinal velocity distribution of the atomic beam can be adjusted. The intensity ratio of pusher to retarder is studied in the QUANTUS-2 experiment [108]. It shows that the highest effective loading of the 3D-MOT is obtained by $I_{\mathrm{pusher}}/I_{\mathrm{retarder}} = 4:1$. Since this result agrees with the one presented in [57] and the $2D^+$-MOT setup of QG-1 is similar to QUANTUS-2, this ratio is also employed for QG-1 without independent optimization. For this, instead of using an additional collimator for the retarder beam, the reflection of the pusher beam from the surface of the pumping stage is used after a retro-reflection from a broadband mirror installed outside of the vacuum chamber. The setup is shown in fig. 5.3(b). A 50% ND filter is attached in front of the retro-reflecting mirror, through which the pusher light passes twice. With such configuration, the intensity ratio of the pusher beam to the retarder beam stays constant at 4 : 1. This ratio can still be adjusted

1 The 2D-coils generate a magnetic field gradient of 6.73 G/cm/A. This value results from the magnetic field simulation [77].

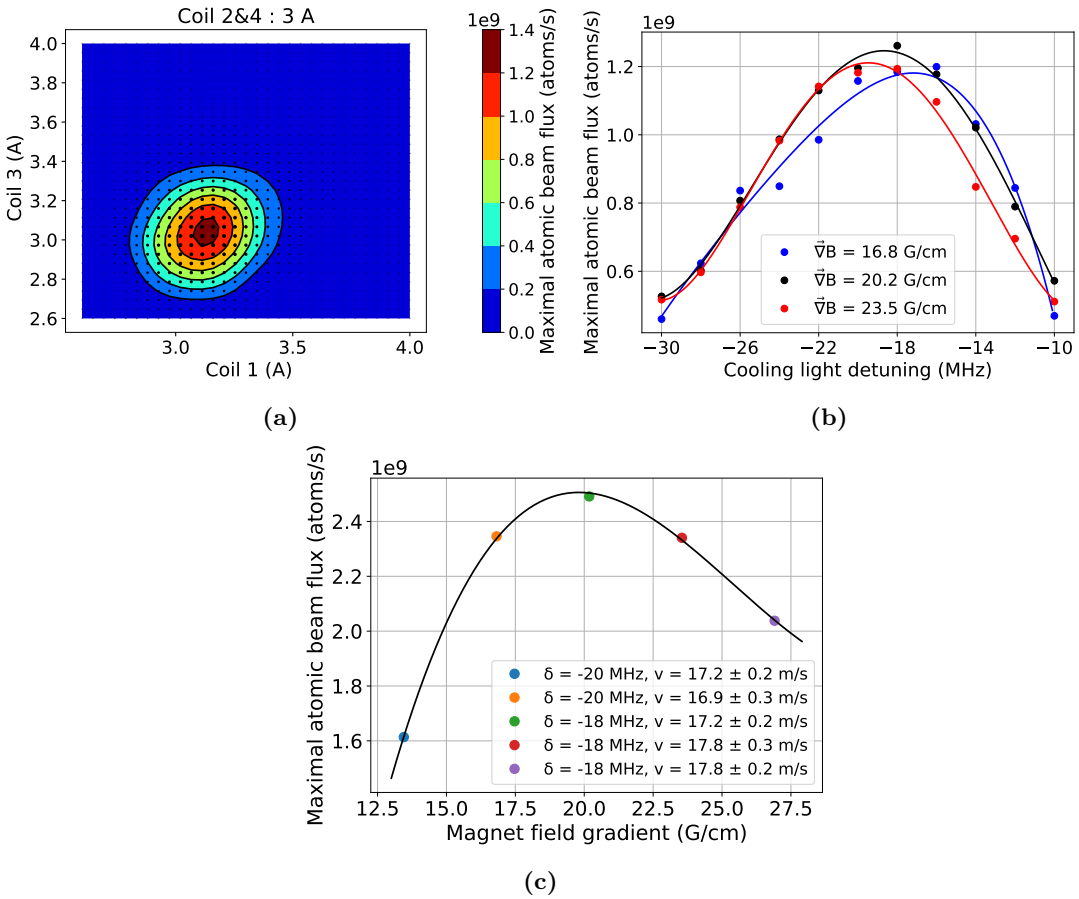

Figure 5.6: a) The center of the quadrupole field is aligned scanning the coil currents. Here, the result of this scan for the case of 3 A current in the coil pair 2 and 4 is presented. The optimum current in coils 1 and 3 is found from a Spline interpolation on the data points. b) The dependency of the maximal 2D-beam flux on the magnetic field gradient and cooling light detuning. Larger light detuning is required for stronger magnetic field gradients. The highest flux is reached with 18 MHz red-detuned cooling light. c) A summary of the four-dimensional scan of the 2D$^+$-MOT parameters. The dependency of the maximal atomic beam flux and its velocity on the 2D-magnetic field gradient and the cooling light detuning is plotted. The optimum magnetic field gradient is found to be at 19.8 G/cm, which is generated by 2.95 A in the coil pairs 2 and 4. The measured velocity of atoms in the beam with these parameters is measured at $v = 17.2 \pm 0.2$ m/s.

using a different ND filter if required. Keeping the intensity ratio of pusher to retarder constant, the intensity of the pusher light is scanned and its effect on the atomic beam flux is studied. The result is presented in fig. 5.7. The highest flux is achieved at a pusher light power of 3 mW. With the 6 mm beam diameter, this corresponds to 10.6 mW/cm^2 light intensity which is 6.3 I_{sat}.

In order to reach the maximum possible flux, the pusher beam should be aligned parallel to the hole of the differential pumping stage. The alignment is possible using the mounting

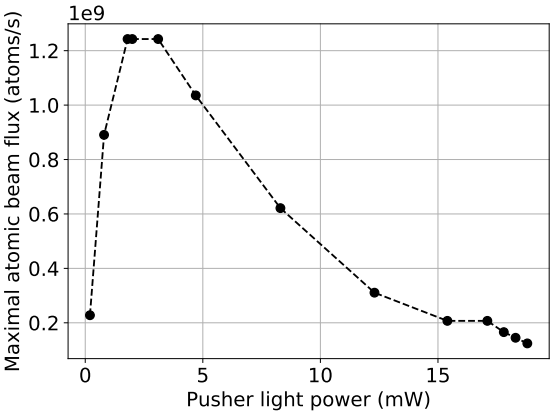

Figure 5.7: Dependence of the cold atomic beam flux on the pusher light power. The highest flux is obtained at a pusher light power of 3 mW.

screws on the pusher collimator (fig. 5.3(a)). Since the view port of the 3D-MOT chamber in front of the pumping stage is free of optics, the alignment process is realized by observing the beam from this window. It is expected, that the highest flux will be obtained when the pusher beam is straight. The collimator is deliberately tilted on two axes and the atomic beam flux is monitored at each angle. It is observed that the beam flux increases when the pusher beam is slightly tilted in the horizontal direction to an angle of 0.3 degree. This tilt is required to compensate the remaining asymmetries in the magnetic field geometry and to reach the highest atomic beam flux.

Light induced atom desorption (LIAD)

An immediate and temporary increase in the partial pressure of rubidium atoms in the $2D^+$-MOT chamber is possible using LIAD [109, 110]. Radiating ultraviolet (UV) light in the chamber desorbs the atoms which are absorbed on the walls of the vacuum chamber. This leads to a temporary increase in the partial pressure of rubidium. The LIAD circuits in QG-1 are mounted on the two sides of the $2D^+$-MOT chamber on which no collimators are assembled (on the sides with coils 2 and 4 as it can be seen in fig. 5.3). Each circuit contains three light-emitting diodes (LED)s with emission wavelength of 375 nm (PUR-LED 414375030). These LEDs are connected in series with a 56 Ω resistor and a solid-state relay (Crydom D1D40) to a 12 V supply. With this, they can be switched by the experiment's control system. The LIAD is only switched on during the operation of the $2D^+$-MOT. An improvement in the atomic beam flux by a factor of 1.5 is attained adding LIAD to the QG-1 setup.

In summary, a cold atomic beam flux of 2.2×10^9 atoms/s is realized, which is 6.6 times higher than the one reached with the pure 2D-MOT without the pusher and retarder beams.

5.2.2 3D-chip-MOT

The atoms loaded from the cold beam are trapped in a 3D-MOT formed of a quadrupole magnetic field in combination with the 3D-cooling lights. For the operation of a 3D-MOT,

laser light forces are required from all directions and thus six laser beams are needed. In a mirror-MOT setup, two of the cooling beams are reflecting on the chip surface under a 45° angle lowering the number of required cooling collimators to four [54]. The magnetic field of a mirror-MOT is generated from a U-wire and a homogeneous magnetic field provided by a pair of Helmholtz coils [54]. In QG-1, a two-dimensional quadrupole field is generated from the center part of the mesoscopic U-wires in combination with the bias field generated from the x-coils (fig. 5.1(a), see fig. 3.9 for the definition of the coils). The confinement along the y-axis is added by the bent sides of the U-structure, forming a three-dimensional trap. However, the magnetic field gradient produced by these side wires is weaker than that of the middle wires. Therefore, in the direction along the center wire, e.g. along the y-axis (fig. 5.1), the magnetic field gradient is the weakest and it is known as the weak axis of the U-MOT. Correspondingly, the strongest gradient is in the direction perpendicular to the center wire, e.g. along the x- and z- axes. Furthermore, the bent side wires cause a z-component in the generated magnetic field, which leads to a deviation in the quadrupole axes and needs to be compensated. Such compensation is implemented by a bias field from the z-coils [55]. Adjusting the current in the U-wires and x-coils defines the strength of the trapping field and its center position. The center of the quadrupole field should be where the 3D-MOT beams overlap. This lays at the middle point of the 3D-MOT chamber, 4 mm away from the chip surface.

The atoms start to fill the MOT with the loading rate Φ, which depends on the atomic beam flux and the capturing efficiency of the 3D-MOT. The lifetime of the atoms in the MOT is limited due to the loss of atoms caused from interactions with each other and with the background gas or because of the radiation pressure from the rescattered photons. In a double MOT setup, since the background pressure in the 3D-MOT chamber is very low and the MOT is loaded from an atomic beam, the loss due to the atom-atom interactions is negligible and the main limiting factor is light-assisted collisions. The maximum number of trapped atoms N_{max} in a MOT is therefore determined by the balance between the loading rate and the loss rate. The time derivative of the atom number in the MOT is given by:

$$\frac{dN(t)}{dt} = \Phi - \Gamma N(t) \tag{5.7}$$

where, $N(t)$ is the number of atoms in the MOT as a function of time, Φ is the loading rate of the MOT and Γ is the total loss rate of the atoms from the MOT. At the point in which the loading rate and the loss rate are equal, the number of trapped atoms saturates at N_{max}. The lifetime of the atoms in a MOT can be determined by stopping the loading mechanism into the MOT and observing the decay of the number of the trapped atoms. Substituting $\Phi = 0$ in eq. (5.7), the solution is an exponential decay curve:

$$N(t) = N_0 e^{-t/\tau}. \tag{5.8}$$

Here, N_0 is the number of the atoms in the trap at the moment that the loading into the trap is stopped and τ is the lifetime of the MOT. The loading and holding of the MOT is observed using its fluorescence signal (section 4.3). An example of a MOT loading curve in

QG-1 is illustrated in fig. 5.8. From this curve, information about the MOT parameters is obtained. The effective loading rate, Φ_{eff}, is extracted from the initial linear slope of the loading curve. In order to measure the lifetime of the MOT, τ, the exponential decay of the atom number in the MOT is observed when the loading has stopped. During this time, the magnetic field and the light of the 2D$^+$-MOT are switched off.

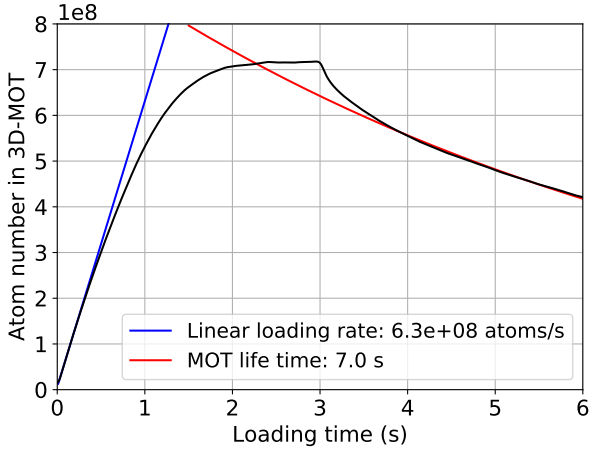

Figure 5.8: An example of the 3D-MOT loading curve obtained from the fluorescence imaging (black curve) is presented. The effective loading rate of the MOT, Φ_{eff}, is derived from the initial slope (blue line). This shows an almost linear increase in the atom number from which $\Phi_{eff} = 6.3 \times 10^8$ atoms/s is resulted. The atom number in this MOT saturates with $N_{max} = 7.1 \times 10^8$ atoms in 2.1 s. An exponential decay fit yields to a MOT lifetime of $\tau = 6.4$ s (red curve).

MOT parameters can be adjusted by the magnetic field gradient and the cooling light power and detuning (section 5.2). Increasing the magnetic field gradient, increases the trap depth but reduces the trapping volume. Therefore, its optimum value and the corresponding cooling light detuning needs to be found. This optimization is performed by observing the effective loading rate while scanning the cooling light detuning and the field generating currents. The cooling light detuning can be set independently for the 2D$^+$- and 3D-MOT using two AOMs (section 3.8.2). The effective loading rate of the 3D-MOT can be attained from the loading curve realized by the atomic fluorescence using the 3D-cooling lights as fig. 5.8 represents. However, this detected fluorescence signal depends on the 3D-light power, detuning and its position with respect to the atoms. During the optimization process, the cooling light detuning as well as the currents in the mesoscopic U-wires and three pairs of Helmholtz coils are scanned, which affect the center position of the 3D-MOT as well. Hence, the fluorescence signal from the 3D-MOT beams is not a suitable tool for optimization of the effective loading rate and an absorption imaging (section 4.1) after a certain time of the MOT loading is used instead. For this measurement, the detection system 2 with the magnification factor of 0.5 is employed. The goal of QG-1 is reaching the highest atom number in the shortest possible time. Furthermore, QUANTUS-2 has illustrated the generation of a BEC with 4×10^5 atoms with a MOT loading time of only 150 ms. Therefore, a MOT loading time of 100 ms is chosen for this measurement

considering the high available flux of the atomic beam. After 7 ms of free expansion time, an image is taken using a 2 mW on resonance probe light. The result of this five-dimensional scan is summerized in fig. 5.9 and 5.10. Every point is an average between two sets of measurement. Since this five-dimensional scan of the MOT parameters require a time period of about an hour, the averaging is not performed over more sets of measurements. This is to prevent the effect from a drift of parameters such as light power during a long measurement time.

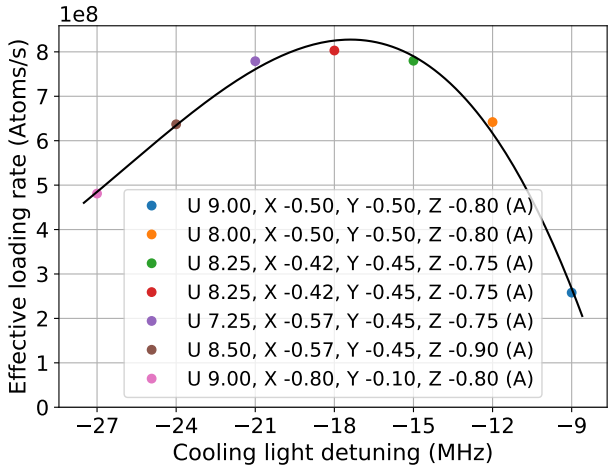

Figure 5.9: 3D-MOT effective loading rate dependence on the cooling light detuning from the transition. The optimum detuning is found from a polynomial fit on the data points. It shows that an 18 MHz red-detuned cooling light results in the highest effective loading rate. Each data point is an average over two measurement sets.

Figure 5.9 shows the maximum effective loading rate reached at each cooling light detuning. The optimum electric current in each current carrying structure is illustrated on the plot. From a polynomial fit to this data, the optimum cooling light detuning is estimated at -18 MHz. Figure 5.10 depicts the dependence of the effective loading rate on the currents in the coils and chip structure for -18 MHz red-detuned light. The optimum values are found from a Spline interpolation of the measurement points since an analytical model does not fit on this asymmetric data. The resulting optimum currents are $[I_{\mathrm{Meso-U}}, I_{\mathrm{x-coil}}, I_{\mathrm{y-coil}}, I_{\mathrm{z-coil}}] = [8.25, -0.42, -0.45, -0.75]$ A. Typically, for a similar setup, a magnetic field gradient of 20 G/cm along the strong axis, x-axis in this case, leads to an optimum MOT operation [72, 79]. Since the measured position of the 3D-MOT center does not agree with the predicted position of the center of the quadrupole field from the simulation, the simulation has not be employed for the estimation of the properties of this quadrupole field [77]. In order to study if this mismatch is caused due to the electric current in the chip structure and coils, the current drivers are characterized and calibrated in [77] and their proper performance is approved. Therefore, the cause is assumed to be due to the alignment of the 3D-MOT beams with respect to each other. It is suspected that the intersection of these beams is not placed at the center of the 3D-MOT chamber. Additionally, the light imbalance of these four beams due to the adoption of the fiber

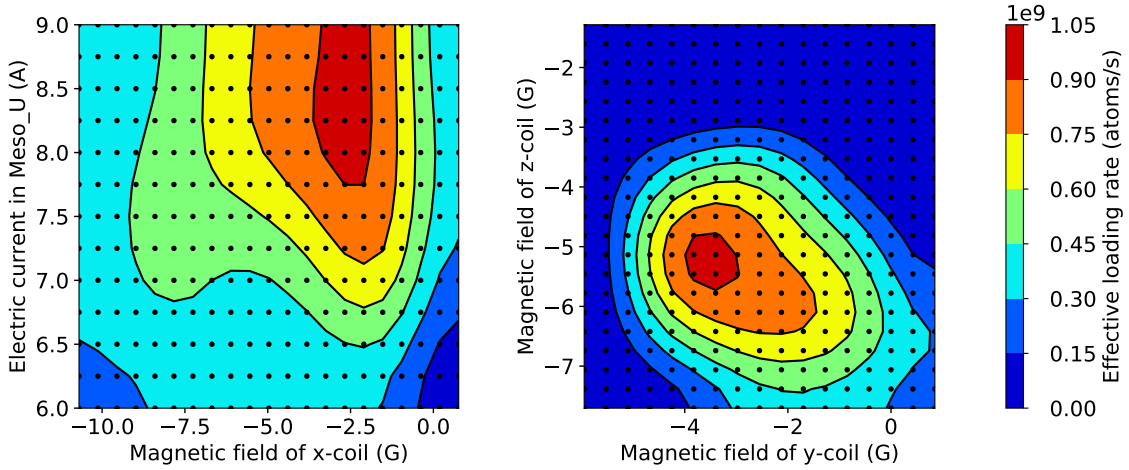

Figure 5.10: Dependence of the 3D-MOT effective loading rate on the magnetic field configuration for 18 MHz red-detuned light. The effective loading rate is plotted over the current in the mesoscopic U-wires and the bias field of the three pairs of Helmholtz coils. The plot depicts the results of a Spline interpolation on the data points from which the optimal currents are found. Each data point is an average over two measurement sets. For further details refer to [77].

splitter (section 3.8.3) affects the center position of the 3D-MOT as well. This is also the cause of the requirement of a high bias field in the y-axis, e.g. −3.8 Gauss as seen in fig. 5.10. In the next stages of the experiment, a homebuilt free-space beam splitter is replacing this fiber splitter and the finer adjustments of the beam orientation will be performed.

In order to confirm that the presented result form imaging the 3D-MOT after 100 ms of loading time is not leading to only the highest loading rate, but also to a high atom number and a long lifetime, another measurement is performed observing the loading curve of the 3D-MOT using the fluorescence imaging. In this measurement, the 3D-MOT parameters are scanned similar to the above measurement and a 3D-MOT loading time of 2 s is followed by a decay time of another 2 s. The optimum parameters for obtaining the maximal Φ_{eff}, N_{max} and τ are confirmed to be at the same range as the previous measurement.

An increase of the cooling light intensity increases the scattering rate R_{sc} and hence the cooling force acting on the atoms. However, this increase in force will stop when the scattering rate saturates, because rising the light intensity further increases the rate of stimulated emission [58]. The dependency of the effective loading rate of the 3D-MOT on the cooling light power is illustrated in fig. 5.11. No improvement in the effective loading rate is observed at powers higher than 24 mW per beam. Therefore, this power is chosen in the experiment, which with a beam diameter of 17.2 mm (3.5.1) corresponds to 10.6 mW/cm^2 which is 6.3 I_{sat}.

Increasing the diameter of the cooling beams at a constant intensity, increases the capturing volume of the 3D-MOT and therefore more atoms can be trapped. However, in

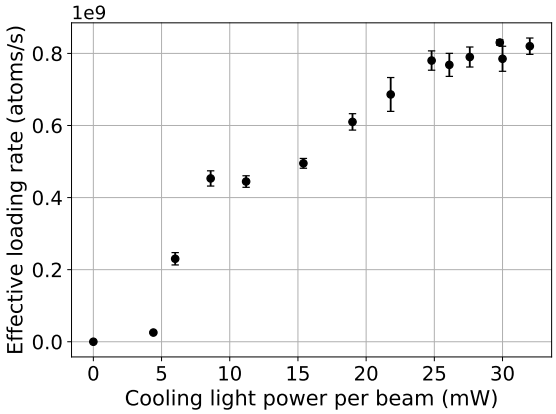

Figure 5.11: 3D-MOT effective loading rate dependence on the cooling light power in each collimator. The presented plot is an average over 4 sets of measurements. 24 mW per beam is chosen in the experiment.

the compact chip setup, a large beam can lead to stray light scattered from the chip edges. In QG-1, the part of the 3D-MOT beams which would shine light on the chip holder are covered on the view ports of the chamber. In order to study the possibility of using smaller beam diameters without reducing the MOT performance for the miniaturization of the next generation setups, the influence of a smaller beam diameter to the 3D-MOT loading rate is studied. For this measurement, one inch iris diaphragms (Thorlabs SM2D25) are installed onto the front of each 3D-collimator. Figure 5.12 shows the dependence of the effective loading rate on the beam diameter. It confirms an improvement increasing the beam size to the full diameter of the collimators at 17.2 mm. A 2 mm reduction of the beam diameter lowers the efficiency by only 5%. After this measurement, the apertures are detached from the experiment.

Another parameter that needs to be optimized for a good performance of the 3D-MOT is the input electric signal to the fiber-coupled EOM, which generates the repumping light. The frequency of this signal should be such that the sideband frequency of the EOM lays at the repumping frequency, i.e. on resonance with the D_2 transition $F = 1 \rightarrow F' = 2$. This corresponds to 6.586 GHz at the cooling light detuning of -18 MHz and can be set by the computer control system. The input electric power to the EOM defines the amplitude of the sidebands, which specifies the power distribution of the laser system between the cooling and the repumping light. In this section, the optimization of the input electric power is presented. Adjusting this power is realized by attaching different rf attenuators before the input of the EOM. The effective loading rate of the 3D-MOT is measured at these different electric powers. In order to confirm if the repumping light power is sufficient, the input frequency is scanned over a range of 400 MHz and the effective loading rate of the 3D-MOT is monitored. The result of this scan is presented in fig. 5.13. The highest loading rate is observed at an input power of 2.7 dBm shown with the red color in the graph. The broadened peak at 6.586 GHz confirms an adequate light power to repump the atoms from their dark state. The second and smaller peak appears when the frequency of the sideband

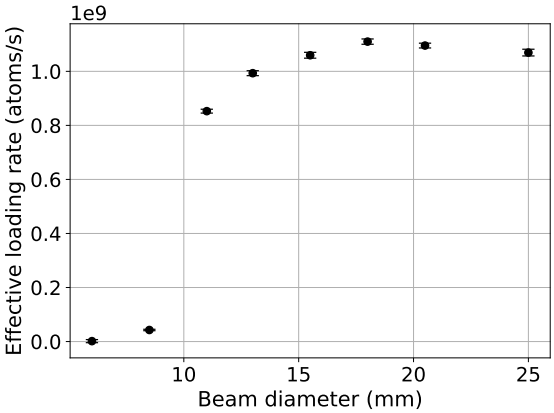

Figure 5.12: Dependency of the 3D-MOT effective loading rate on the 3D-beam diameter. The diameter of the cooling beams is reduced using iris diaphragms installed onto the front of each 3D-collimator. Each data point is an average over 10 measurements. Opening the apertures to the full beam diameter of 17.2 mm improves the effective loading rate of the 3D-MOT. A 2 mm reduction of the beam diameter lowers the efficiency by 5%.

is on resonance to the $F = 1 \rightarrow F' = 1$ transition, since such light addresses the atoms on their dark state as well and brings them back to the cooling cycle less efficiently. The repumping light power at this point can be estimated by calculating the absolute square of the 1^{st} order Bessel function in dependence of the modulation depth as $\delta = \pi V_m / V_\pi$ [91]. Here, V_m is the modulation voltage, which is about 0.3 V at an rf input with 2.7 dBm power. V_π is the half-wave voltage and is estimated from the response graph of the EOM as $V_\pi \simeq 5.59$ V at 6.5 GHz. With this, it is estimated that 98.6% of the total light power is in the career for cooling and about 1% is in the first sideband for repumping.

In summary, a reliable performance of the 3D-MOT with an effective loading rate of 8.1×10^8 atoms/s has been realized.

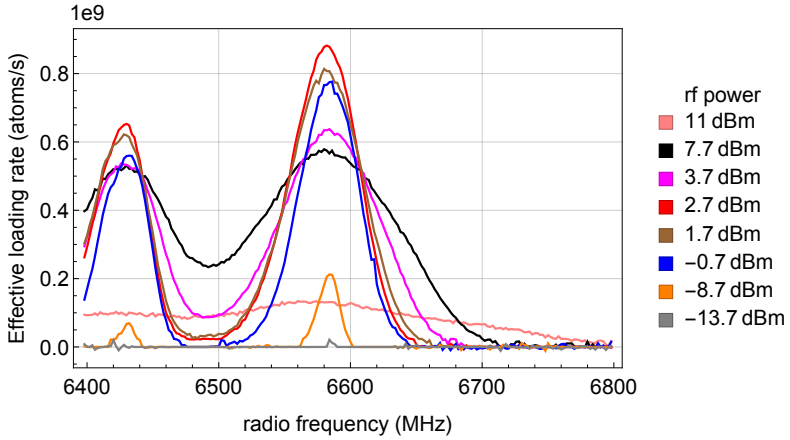

Figure 5.13: Dependence of the 3D-MOT effective loading rate on the electric power and frequency of the input signal to the fiber-coupled EOM used for the generation of the sidebands for repumping. An optimum input electric power of 2.7 dBm is resulted (red curve). A scan of the input frequency over the repumping resonance confirms a sufficient light power for repumping. The second and smaller peak appears when the repumping light is on resonance to the $F = 1 \rightarrow F' = 1$ transition. This light talks to the atoms fallen into their dark state as well and brings them back into the cycling transitions, but less efficiently.

5.3 Compressed MOT and the polatization gradient cooling

The 3D-MOT is loaded at the center of the 3D-MOT chamber 4 mm away from the chip surface. For an efficient transfer of the atoms to the first magnetic trap, they should be shifted to the point where the minimum of this trap is located. This is at 1.2 mm distance from the chip surface. Increasing the bias field of the x-coils while reducing the current in the mesoscopic U-wires shifts the center of the 3D-MOT towards the chip. By this, the atomic cloud compresses as well leading to higher atomic densities. Increasing the cooling light detuning additionally helps to further compress the cloud. The higher the density of the cloud gets, the more atoms can be transferred to the initial magnetic trap. This compression is particularly important in the QG-1 setup, since the weak axis of the quadrupole field of the U-MOT in the y-direction is perpendicular to the weak axis of the harmonic trap in the x-direction (fig. 5.1, refer to section 3.4.1 for the reason of this choice). This makes the mode matching more difficult and can lead to a loss of atoms during the loading process if the atomic density at the center of the cloud is low. After the shift and compression, the magnetic fields are switched off. Simultaneously, the introduced force from the light on the atoms is reduced by increasing the light detuning further while lowering its intensity. Here, the atomic ensemble is cooled to sub-Doppler temperatures by polarization gradient cooling (PGC) [60, 111]. The residual environmental magnetic fields at the position of the atoms should be compensated in this step in order to reach lower

temperatures[1]. The compensation field is provided by three pairs of Helmholtz coils on the 3D-MOT chamber for the x-, y- and z- directions. The required current in the coils needs to be characterized. For this, the current in each pair is independently scanned and the cloud temperature after the PGC phase is determined via a time-of-flight (TOF) measurement (fig. 5.14) [112]. The result of temperature dependence on the current in each pair of coils is presented in fig. 5.15. The absorption imaging system 2 with the magnification factor of 0.5 and parallel to the x-y-axis is employed for this measurement (section 4.1). The lowest temperature is obtained for coil currents $(I_x, I_y, I_z) = (-14.5, -98.6, -9)\,\mathrm{mA}$. This corresponds to a bias magnetic field of $(B_x, B_y, B_z) = (-111, -844, -58)\,\mathrm{mG}$ at the position of the atoms (table 3.2). The environmental magnetic field at the location of the sensor head is measured with a Gaussmeter (F.W. Bell 7030) as $(B_{Hx}, B_{Hy}, B_{Hz}) = (120, 370, 40)\,\mathrm{mG}$. The large difference between the measured and the expected values of the required bias field for the compensation in the y-axis is due to the same cause described in section 5.2.2, it is suspected that the 3D-MOT beams are not overlapping at the center of the 3D-MOT chamber and therefore a high current in the y-coil is required to compensate this shift.

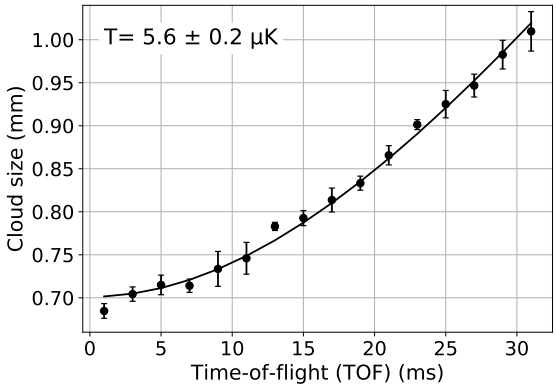

Figure 5.14: Temperature measurement after the PGC from the free expansion of the cloud during the free fall. The size of the atomic cloud after different times of free expansion is determined via absorption imaging. The temperature of the ensemble can be found from the rate of this expansion and equation 5.9.

An example of the measurement of the atomic sample's temperature is illustrated in fig. 5.14. For this, the cloud is let to free fall after the PGC step. From absorption imaging after different times of free expansion, the size of the cloud is determined. Its temperature can be calculated from the rate of this expansion:

$$\sigma^2 = \sigma_0^2 + \left(\frac{K_B T}{m} t^2\right). \tag{5.9}$$

Here, σ is the size of the cloud after the free expansion time and σ_0 is its initial size in the

1 The magnetic shield has not yet been assembled on the sensor head in order to permit enough physical access to the setup.

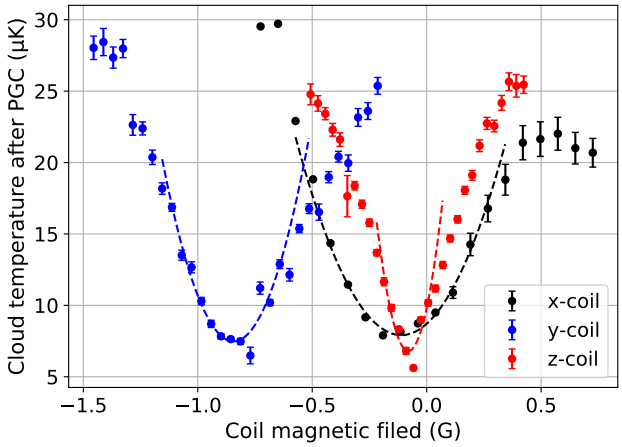

Figure 5.15: Dependence of the cloud temperature after PGC on the magnetic field generated by each pair of the bias coils for the compensation of the environmental field. The minimum temperature is obtained when the coils' field compensate the environmental magnetic field at the position of the atoms. This is reached at the coil fields of $(B_x, B_y, B_z) = (-111, -844, -58)\,\mathrm{mG}$. The TOF measurement at this point is the one illustrated in fig. 5.14 and results in a temperature of $5.6\,\mu\mathrm{K}$. Detection system 2 installed parallel to the x-y-axis with magnification factor of 0.5 (section 4.1) is employed for this measurement. Each data point in this plot is an average over 3 sets of measurement.

cold atomic cloud before the release. K_B is the Boltzmann constant, m is the mass of a ^{87}Rb atom and t is the free-fall time. The temperature is found from this formula and the fit to the measurement points. The lowest temperature reached in QG-1 is $5.6 \pm 0.2\,\mu\mathrm{K}$. This shows an improvement in comparison to the previous similar setups, QUANTUS-2 and MAIUS-A, in which the temperature after PGC is reported as $12\,\mu\mathrm{K}$ and $14.8\,\mu\mathrm{K}$ respectively [71, 72]. The temperature that can be reached by PGC is limited by the power imbalance and polarization imperfections of the cooling lights. This is due to the poor quality of the fiber splitter as well as further power imbalance caused by the mirror-MOT setup, which introduces an initial velocity of atoms after the PGC step. This velocity is measured from tracing the atomic trajectory during the free fall as $1.3\,\mathrm{mm/s}$.

Several measurements have been performed to find the optimum parameters in each step in order to obtain the highest number of trapped atoms in the initial magnetic trap. The optimal sequence has been found as the following. The 3D-MOT is loaded for $300\,\mathrm{ms}$[1]. Afterwards, the atomic ensemble is pulled closer to the chip surface and is compressed. This is done by ramping up the bias field via increasing the x-coil current to $-1.8\,\mathrm{A}$ within $10\,\mathrm{ms}$. The current in the mesoscopic U is simultaneously ramped down to $7\,\mathrm{A}$. With this, the atomic density is increased. The intensity and detuning of the cooling light stays unchanged during this step. The compression of the cloud through increasing the magnetic field gradient is not feasible in this setup since it could only be applied by increasing

1 This time is chosen based on the loading efficiency into the magnetic trap. See section 5.4.2.

the bias field, which moves the center of the trap into the chip assembly. Therefore, the atomic cloud is further compressed by increasing the cooling light detuning. This process is divided into three steps. In the first 2 ms, the U-current is ramped down to 3 A while the x-coil current is ramped down to −0.66 A. The detuning of the light is stayed unchanged. In the next 1 ms, the currents in the U-wires and the x-coils are further reduced to 1 A and −0.1 A respectively while the cooling light detuning is ramped up to −60 MHz. The currents are ramped down further to 300 mA in the chip wire and −14.5 mA in the x-coils[1] in the next 500 μs. At the end of this stage, the atoms are at a temperature of 126 μK and 1.2 mm away from the chip surface, where the center of the initial magnetic trap is located. The peak density of this ensemble is measured at 2.9×10^{10} atoms/cm^3, which is an order of magnitude larger than the measured value in the 3D-MOT as 2.0×10^9 atoms/cm^3. At this position, the cloud temperature is reduce by polarization gradient cooling. This improves the number of atoms that can be confined in the subsequent magnetic trap. For this, all the magnetic fields are switched off and the bias coils' currents are set to the values required for the compensation of the environmental magnetic field (fig. 5.15). The light force on the atoms is reduced by ramping up the cooling light detuning and lowering the intensity of the cooling and repumping light. The dependency of the cloud temperature to these parameters is studied and the result is summarized in fig. 5.16. Changing the light parameters shows more significant effect on the cloud temperature than the atom number. The lowest temperature is attained when ramping the total light power down to 2.7 mW and ramping the detuning of the cooling light up to −157 MHz. The duration of the PGC step is optimized using the same method as fig. 5.17 illustrates. Increasing this duration up to 3 ms shows an improvement in the temperature. Elongating this step further, does not introduce any temperature reduction, but can lead to an expansion of the cloud or loss of the atoms due to random interactions. Therefore, 3 ms is chosen for the duration of the PGC step.

1 This is the current required to compensate the environmental magnetic field.

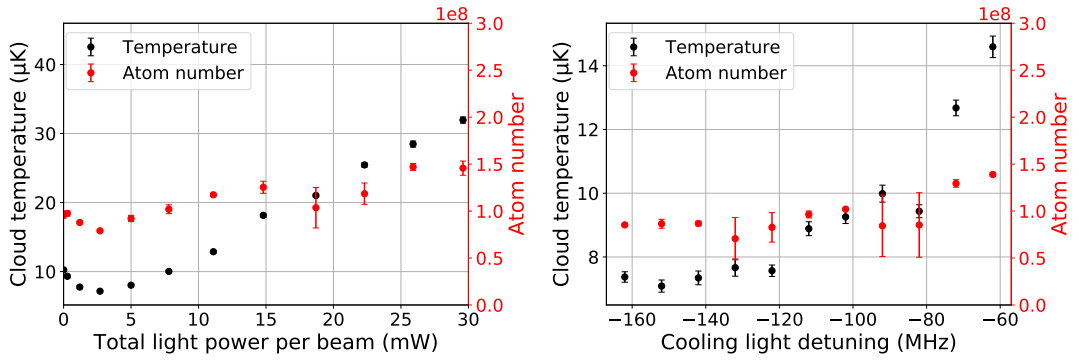

(a) (b)

Figure 5.16: Dependence of the cloud temperature after PGC on the light parameters. These plots suggest that the minimum temperature is obtained when ramping the cooling and repuming light power down to 2.7 mW (a) while increasing the detuning of the cooling light to −157 MHz (b). A big influence on the total atom number in the cloud has not been observerd. Each data point is an average over 3 sets of measurements.

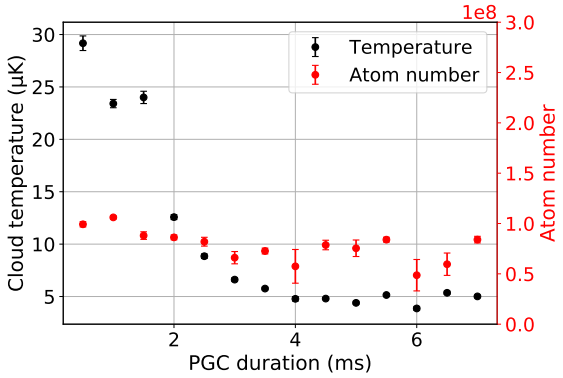

Figure 5.17: Temperature dependance of the atomic cloud after the PGC step on the duration of this step. The cloud temperature is reduced by increasing the duration of the process up to 3 ms and no improvements has been observed at longer durations. Each data point is an average over 3 sets of measurements.

5.4 Magnetic trap

Laser cooling of atoms is limited to the recoil temperature by the energy that atoms receive when reabsorbing scattered photons [58]. This temperature is equal to 361.96 nK in the case of ^{87}Rb [83]. In order to cool atoms beyond the recoil limit, one can use evaporative cooling [113]. This process relies on collisions to rethermalize the atoms. Therefore, the laser cooled atoms need to be first confined inside a magnetic trap. The magnetic trap provides the confinement of the atoms and compresses them to increase the collision rates for an efficient evaporation.

5.4.1 Optical state preparation

As described in section 2.3, the atoms in the low-field seeking states, $m_F g_F > 0$, can be trapped in a local minimum of an inhomogeneous magnetic potential. For the $5^2S_{1/2}, F = 2$ level of ^{87}Rb, these are atoms with magnetic quantum numbers $m_F = +1$ or $+2$ as $g_F = +1/2$. It is preferable to trap atoms in their Zeeman state $m_F = +2$ in order to obtain a higher trap depth, because the force applied on them in a same magnetic field is twice larger in comparison to the atoms in the $m_F = +1$ state. However, after the polarization gradient cooling the atoms in the cloud are spread in different spin states of the $5^2S_{1/2}, F = 2$ level. Hence, before transferring them in a magnetic trap, they are pumped into $m_F = +2$ with σ^+ polarized light on resonance with $F = 2 \rightarrow F' = 2$ transition in a few cycles. This process is referred to as the optical state preparation. $| F = 2, m_F = +2 >$ is a dark state for the pumping light, which makes this way preferable to an optical state preparation process using a light on resonance with $F = 2 \rightarrow F' = 3$ transition. In the experiment, the same beam collimator is used for the detection and the optical state preparation. The atoms are exposed to a light pulse of 1.2 mW power corresponding to an intensity of 0.5 mW/cm^2 for 100 μs. The pulse intensity and duration are set low enough to avoid heating of the ensemble. For the quantization, a 4.33 G magnetic field parallel to the direction of the circular polarized light is employed via the Helmholtz coils, the same way as it is done for the absorption imaging (section 4.2). At this stage of the experiment, the repumper light is switched off during the optical state preparation. This is because a fast change of the repumper frequency in a time below 1 s was limited to a range of 162.4 MHz. This is described in details in section 3.9.2. In the next steps of the experiment, a wider control range of the repumper frequency will be implemented in the computer control system [97]. Adding the repumper light during the optical state preparation will improve the number of atoms transferred into the magnetic trap.

In order to determine the optimal light frequency for the optical state preparation, experiments with different frequency values of the light are performed and the number of atoms captured in the subsequent magnetic trap is measured. Figure 5.18 illustrates the result of this scan for both σ^+ (black dots) and σ^- (red dots) lights. For this measurement, the pumping light is shined parallel to the x-axis (fig. 3.9) and the quantization field is applied via a $-/+0.56$ A current in the x-coils for the σ^+ and σ^- transitions respectively. The frequency of the light is scanned in a range of 80 MHz over the resonance frequency. The calculated frequencies of all σ^+ transitions $|F = 2, m_F = i>$ $(i = -2, -1, 0 \text{ and } 1) \rightarrow$ $|F' = 2, m_F = j>$ $(j = -1, 0, 1 \text{ and} 2)$, are shown in black vertical lines and for the σ^- transitions, $|F = 2, m_F = i>$ $(i = -1, 0, 1 \text{ and } 2) \rightarrow |F' = 2, m_F = j>$ $(j = -2, -1, 0 \text{ and } 1)$, are shown in red lines. As it can be seen from the graph, the number of captured atoms in the magnetic trap in this measurement increases from 0.9×10^7 to 2.8×10^7 atoms by adding the optical state preparation before the loading process, which corresponds to an improvement by a factor of 3.

5.4.2 Initial magnetic trap

The atomic cloud after the polarization gradient cooling stage features a size of 0.47 mm along the x- and z-direction and 1.2 mm along the y-direction with a temperature of 5.6 μK (section 5.3). After the optical state preparation, the atoms in this ensemble are loaded

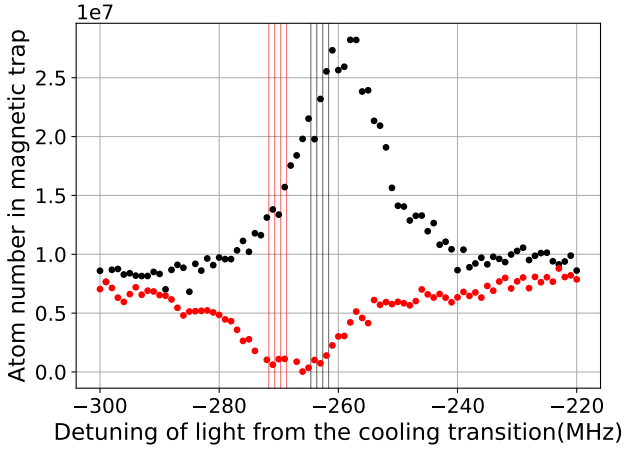

Figure 5.18: Characterizing the optimum laser frequency for optical state preparation. The number of atoms in the initial magnetic trap is observed while scanning the frequency of the cooling beam in a range of 80 MHz over the resonance frequency of the $F = 2 \rightarrow F' = 2$ transition. The beam is shined parallel to the x-axis and the quantization field is implemented via the x-coils (fig. 3.9). The x-axis of the graph determines the red-detuning of the light frequency from the cooling transition of ^{87}Rb, $F = 2 \rightarrow F' = 3$. The measurement is repeated for both σ^+ (black dots) and σ^- (red dots) light polarization by flipping the direction of the magnetic field used for quantization. The calculated frequencies of all the σ^+ (black lines) and σ^- (red lines) transitions are depicted on the graph. The result confirms an improvement by a factor of 3 in the number of trapped atoms after the optical state preparation.

into the initial magnetic trap. This trap is a large volume Ioffe-Pritchard trap, which is used as the intermediate step to transfer the laser cooled atoms to the final magnetic trap with a higher frequency and smaller volume. The initial Ioffe-Pritchard trap in QG-1 is generated from the mesosocopic H-wires supported by the Z-wire of the base chip in combination with the bias fields of the Helmholtz coils as it is illustrated in fig. 5.1(b) and fig. 5.19(c). The center wire of the Z-structure and the I-wires of the H-structure together with the bias field of the y-coils generate a two-dimensional quadrupole filed. The side wires of the Z- and H- structures raise the magnetic field at the center of the trap and add confinement in the third axis, e.g. the x-axis. The magnetic field at the trap center can be approximated by a three-dimensional anisotropic harmonic oscillator potential. The confinement along the center wires is weaker in comparison to the one perpendicular to it. Therefore the x-axis is referred to as the weak confining axis of the trap. By changing the bias field of the y-coils, the trap frequency and the distance of its center position to the chip surface can be adjusted. The bias field of the x-coils can be used to adjust the magnetic field strength at the minimum of the trap.

The initial magnetic trap is created by a 9 A current in the mesoscopic H-wires and 5 A in the Z-wire of the base chip. With −0.4 A current in the x-coils, −2 A in the y-coils and −0.5 A in the z-coils, a harmonic trap centered at 1.2 mm distance from the chip surface is generated. 3.6×10^7 atoms are captured in this trap. An absorption image of the atomic cloud is illustrated in 5.19(c). The simulated trap frequency with the mentioned

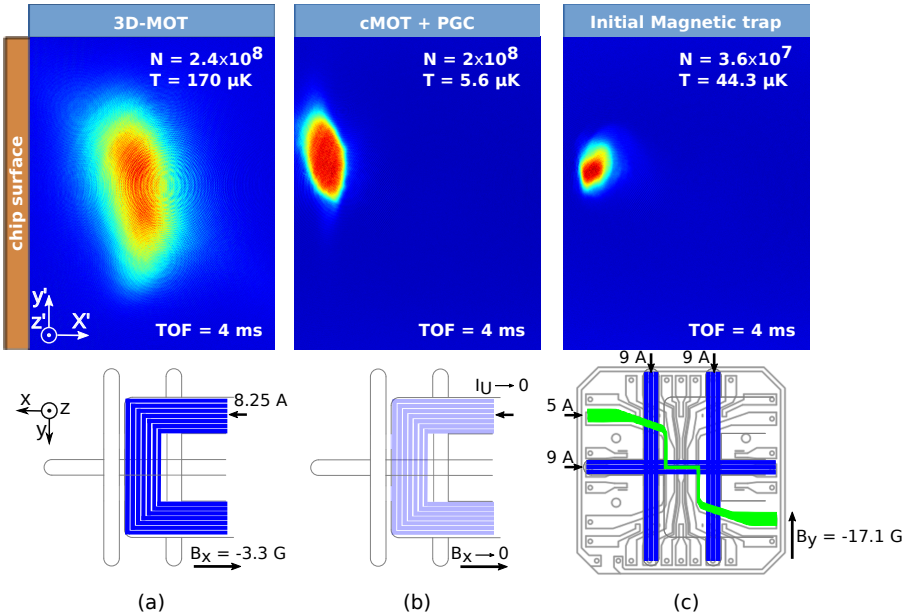

Figure 5.19: Experimental cycle in QG-1 is illustrated using three absorption images together with the employed chip structures and the bias fields. The detection system 2 with a magnification of 0.5 is used for these images. The coordinate system of the camera (x´,y´,z´), x´ = z, y´ = +x - -y, z´ = +x - +y, is illustrated in the picture. The images are taken after 4 ms of free expansion time. After 300 ms loading, 2.4×10^8 atoms are trapped in the 3D-chip-MOT formed by the mesoscopic U-structure of the atom-chip assembly in combination with the bias field of the x-coils. The center of this cloud is place at 4 mm distance from the chip surface, where the MOT beams are intersecting (a). This cloud is compressed and pulled closer to the atom chip, at a 1.2 mm distance. Here, the ensemble is further cooled in a polarization gradient cooling stage to 5.6 μK (b). 3.6×10^7 atoms can be captured in the initial magnetic trap formed by the mesoscopic H-structure and the Z-structure of the base chip together with the bias field of the y-coils (c).

parameters is equal to $(10.5, 51.8, 49.8)$ Hz [77]. In order to measure the trap frequency in the experiment, a center of mass motion measurement is performed changing the holding time of the atoms in the magnetic trap. For this, the holding time is scanned from 50 to 250 ms and the center position of the trap is detected after 10 ms of free fall. The result is shown in fig. 5.20(a) and reveals a trap frequency of 9.1 Hz along the weak axis with a start oscillation amplitude of 900 μm. Observing the atom number in the trap after varied holding times up to 1.6 s, the lifetime of the atoms in the trap is estimated as 5.3 s from an exponential decay fit. The result of this measurement is illustrated in fig. 5.20(b).

In order to determine the optimum loading time of the 3D-MOT, the number of confined atoms in the initial magnetic trap in dependence of the loading time of the 3D-MOT is observed. For this measurement, the 3D-MOT loading time is scanned up to 1 s. At each point, the number of the atoms in the 3D-MOT as well as in the initial magnetic trap after 50 ms of holding is measured. The atom number is determined from an absorption imaging after the 3D-MOT and after the magnetic trap in iterations followed by a 5 ms

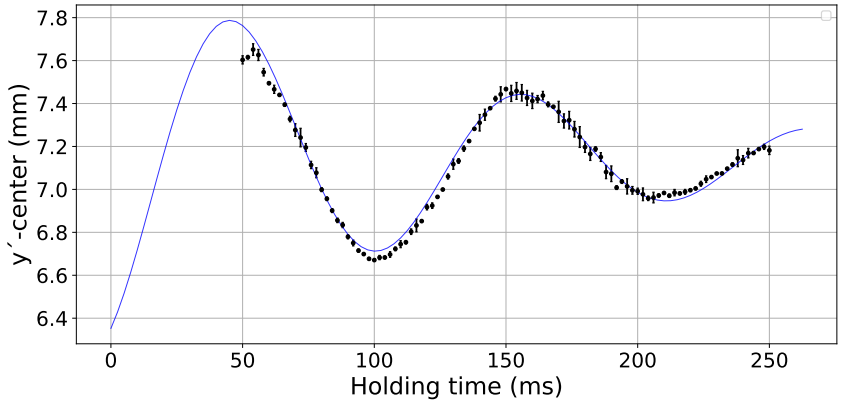

(a)

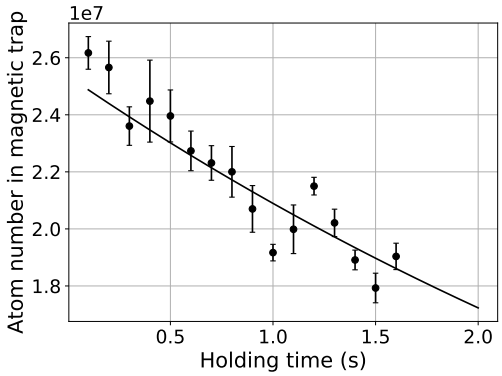

(b)

Figure 5.20: a) Measurement of the trap frequency. The center position of the initial magnetic trap after 10 ms of time-of-flight is plotted in dependence of the holding time of the atoms in this trap. Absorption system 2 (section 4.1) is employed for the imaging. y´ is the y-axis of the camera, which form a 45° angle with the x- and y-axes of the chip coordinate system (section 3.4.1). From this, the trap frequency in the weak axis, which is along the x-axis of the coordinate system is measured at 9.1 Hz. b) Atom number in the initial magnetic trap in dependence of the holding time in this trap. The lifetime of the atoms in the trap is estimated at 5.3 s from an exponential decay fit to this data. The image is taken after 7 ms of free expansion time.

time-of-flight. The result is illustrated in fig. 5.21(a). Figure 5.21(b) shows the efficiency of the transfer into the initial magnetic trap after different loading times of the 3D-MOT. Graph 5.21(a) show that the number of atoms captured in the trap saturates after 300 ms of the 3D-MOT loading time. Although, the number of atoms in the 3D-MOT increases after this time, not all these atoms can be trapped since the size of the cloud increases as well. Therefore, 300 ms is chosen as the loading time of the 3D-MOT. Figure 5.21(b) shows an 18% transfer efficiency of the atoms into the initial magnetic trap at this point. This transfer efficiency can be improved by adding the repumping light during the optical state preparation.

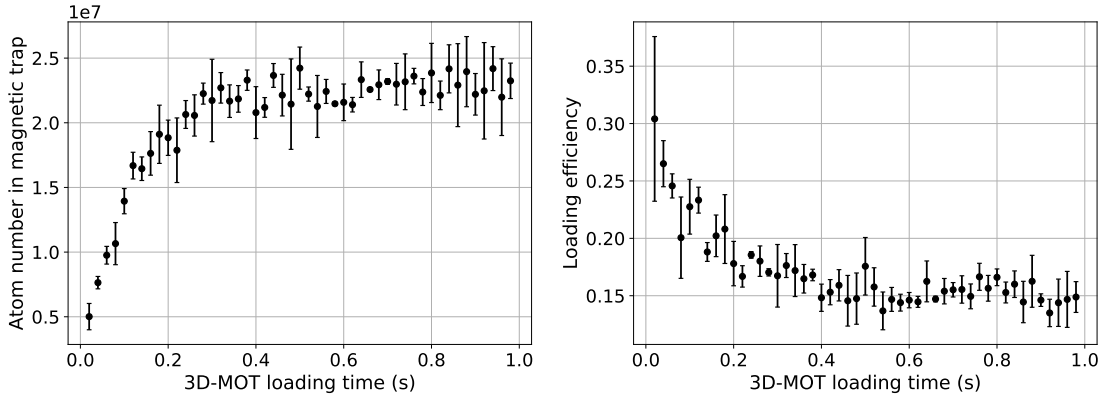

(a) **(b)**

Figure 5.21: Number of atoms captured in the initial magnetic trap (a) and its ratio to the number of atoms in the 3D-MOT (b) in dependence of the loading time of the 3D-MOT. Efficient transfer into the magnetic trap saturates with a transfer efficiency of 18% after 300 ms of 3D-MOT loading.

The goal is to enhance the density of the atomic cloud for an efficient evaporation. The phase-space density (PSD) of an atomic cloud is calculated from

$$\rho = n_0 \lambda_{dB}^3 \tag{5.10}$$

where n_0 is the atomic peak density in the cloud and λ_{dB} is the de Broglie wavelength of the atoms defined as

$$\lambda_{dB} = \sqrt{\frac{2\pi\hbar^2}{m k_B T}}. \tag{5.11}$$

The peak density at the center of a Gaussian cloud is calculated from

$$n_0 = \frac{N}{2\sqrt{2\pi^3}\sigma_x\sigma_y\sigma_z} \tag{5.12}$$

where $\hbar$ is the Plank constant, k_B is the Boltzmann constant, T is the temperature of the ensemble found from a TOF measurement (fig. 5.14), N is the total atom number in the trap and σ_x, σ_y and σ_z are the size of the atomic cloud. The measurement illustrated on graph 5.22 is used for the estimation of the PSD of the atomic cloud inside the initial magnetic trap. For this measurement, the density of the cloud is observed after different expansion time of the cloud after the release from the magnetic trap. The PSD of the magnetic trap is extrapolated from a fit of its function (eq. (5.10)) on these measurement points. For the 3.6×10^7 atoms confined in the magnetic trap, the PSD is estimated as 4.5×10^{-7}. The reason of choosing this method for the estimation of the PSD in the magnetic trap is because the number of the trapped atoms determined from the absorption imaging is more accurate after a few millisecond of free expansion time, when the atomic

cloud is more dilute.

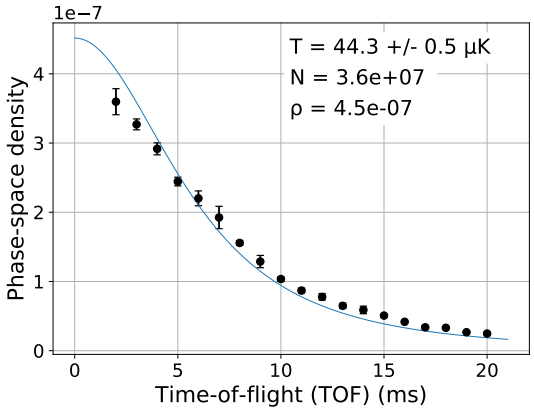

Figure 5.22: The density of the atomic cloud in dependence of the free expansion time after the release from the initial magnetic trap. The PSD of the atoms in the trap is extrapolated from a fit of its function on the measurement points. With 3.6×10^7 atoms confined in this trap, a PSD of 4.5×10^{-7} is estimated. Each data point is an average over three measurement points.

In summary, trapping of 3.6×10^7 atoms in the initial magnetic trap with a PSD of 4.5×10^7 has been demonstrated.

5.4.3 Final magnetic trap

After the atoms have reached thermal equilibrium in the first magnetic trap, they have been adiabatically transferred to the final magnetic trap. This trap features higher frequencies and smaller volumes with its center closer to the atom chip, at 100 μm distance to the chip surface. In such trap, the density of the atomic cloud and hence the collision rates are higher, which leads to a more efficient evaporation. During the loading process, the atoms are shifted closer to the chip surface by switching from the mesoscopic H-structure to the Z-wire of the science chip while keeping the current in the Z-wire of the base chip constant and increasing the current in the bias coils. As the consequence, the atomic cloud is compressed and hence its density is increased. In an initial demonstration, 2.2×10^7 atoms have been trapped in the final magnetic trap.

CHAPTER 6

Summary and Outlook

6.1 Summary and discussions

In this document, the steps towards cooling and trapping ^{87}Rb atoms on an atom chip in the QG-1 experiment has been presented. An atomic beam with a flux of 2.2×10^9 atoms/s, a mean longitudinal velocity of 17.2 m/s and a narrow longitudinal velocity distribution of 2.2 m/s has been produced from the background rubidium gas in the 2D-chamber (section 5.2.1). This high-flux atomic beam has been employed to load an atom-chip-based 3D-MOT and has been optimized aiming for the highest loading rate. This is a critical step to lower the uncertainty and reach a high cycling rate in the quantum gravimeter. A loading rate of 8.1×10^8 atoms/s has been attained (section 5.2.2), which is comparable to the one in QUANTUS-2 presented as 1×10^9 atoms/s [69] and in MAIUS-A as 9×10^8 atoms/s [72]. In the optimized experimental sequence, the 3D-MOT is loaded for 300 ms and 2.4×10^8 atoms are trapped 4 mm away from the chip surface. To guarantee a good spatial overlap, this cloud has been shifted to 1.2 mm away from the chip where the center of the initial magnetic trap is located. Here, the atomic ensemble has been cooled in a PGC stage to 5.6 μK before loading into the initial magnetic trap (section 5.3). This temperature shows an improvement in comparison to the one realized in QUANTUS-2 at 12 μK [71] and the one in MAIUS-A at 14.8 μK [72]. Adding the optical state preparation before loading into the magnetic trap has increased the number of the trapped atoms by a factor of 3 (section 5.4.1). Several measurements on the shifting and compression steps as well as the parameters for the initial magnetic trap have been performed to achieve a better mode match between the laser cooled atoms and this trap. As the result, 3.6×10^7 atoms have been trapped with a lifetime of 5.3 s. This number can yet be improved by adding the repumping light in the optical state preparation. The magnetically trapped ensemble features a temperature of 44.3 μK with a phase-space density (PSD) of 4.5×10^{-7}. The measured value for the trap frequency in the weak axis is equal to 9.1 Hz (section 5.4.2).

6.2 Outlook

After the demonstration of the presented results, the process of adiabatically transferring the atoms into the final magnetic trap with a higher trapping frequency has been performed. During this transfer, the atomic cloud has been pulled closer to the chip surface and its density has been raised. The characterization and optimization of this trap has been done by Jonas Matthias and his PhD thesis is in preparation [97]. In the next step of the experiment, the evaporative cooling will be implemented on this dense atomic sample, in which the ensemble will be further cooled by selectively removing the atoms in the high

energy tail of the Boltzmann distribution [31–33]. This will be done using radio frequency photons generated from the U-structures on the base chip (section 3.4.1). The required rf input is provided from the DDS card in the laser stack (section 3.9.1) and its functionality has been already tested in the experiment. In order to reduce the velocity spread of the atomic ensemble further, the so-called delta-kick collimation (DKC) will be employed [37, 114]. In this technique, after a certain time of free expansion, when most of the mean field energy is converted into kinetic energy, a transient harmonic potential will be applied. The position dependent force from such a potential acts analogous to a lens in optics and collimates the expansion of the atomic ensemble. The lensing potentials will be provided by the current carrying structures on the base and science layers of the atom chip as it is presented in [69].

After the preparation of the atomic ensemble, gravity measurements will be performed on the free-falling atoms. The noise floor of the interferometer is fundamentally limited by the shot-noise limit described by eq. (2.6). QUANTUS-2 and MAIUS-A have demonstrated the production of BECs with 10^5 atoms at a 1 Hz rate [2, 69]. The presented results in this thesis have illustrated comparable outcomes to these experiments and thus the same BEC flux can be expected in QG-1. A maximum free-fall distance of 320 mm is provided in the experiment, which can permit interferometry times of up to $2T = 250$ ms (section 3.2.5). Furthermore, BEC sources allow improvement of fidelities in the manipulation of the atoms during the atom-light interaction, making it feasible to approach an interferometry contrast of unity. Assuming a pulse separation time of $T = 100$ ms, an interferometer contrast of 1 and a cycle time of 2 s, a shot-noise limit of $28\,\mathrm{nm/s^2}$ in 1 s will be estimated for the first-order Bragg-pulse interferometer. With this, a noise level of $0.46\,\mathrm{nm/s^2}$ can be obtained within only an hour of integration. This value will be improved further using higher-order momentum transfer with Bragg-type beam splitters [51, 115, 116] or increasing the time that the atoms spend in the interferometer. Thanks to the narrow momentum width of the magnetically collimated BEC, higher-order Bragg diffractions can be employed with high efficiency [117]. In a mobile ground-based apparatus, the free-fall time is limited by the size of the device. Therefore, increasing the interferometry time can be implemented using a launching mechanism similar to the one presented in the atom-chip fountain gravimeter [51]. In this scheme, the time that atoms spend in the interferometer is extended by accelerating the ensemble upwards using Bloch oscillations and increasing the free-fall time with respect to simply dropping the BEC. In order to reach the atomic shot-noise limited short-term instability, technical noises during measurements should be reduced. The dominant noise source in state-of-the-art gravimeters is the vibration. To reduce this noise, the sensor head will be inertially decoupled from the environment by being placed on a vibration isolation platform during measurements (3.7). The remaining vibrations will be tracked by correlating the interferometry signal with classical sensors and will be post-corrected [118]. Other sources of noises including the laser noise, detection noise and magnetic field effects will be correspondingly investigated and mitigated.

For an accurate gravimetry, in addition to the noise sources, the effects which lead to a bias in the absolute value should be canceled out as well. With the resulted non-expanding ensemble, the improved flatness of the reflective surface on the atom chip to $\lambda/26$ (section 3.4.1) and the high quality reference mirror on the tip-tilt mount inside the

vacuum chamber (section 3.2.6), the bias from the two leading order uncertainties due to the wavefront aberrations and the Coriolis acceleration will be suppressed. In pursuance of improving the accuracy in the measured value of the gravitational acceleration, systematic analysis needs to be conducted. The residual bias from the wavefront aberration will be post-corrected after mapping the wavefront of the interferometer beam via altering the release position and expansion rate of the atomic ensemble. The residual contribution of the wavefront distortion in the uncertainty is estimated below $0.1\,\mathrm{nm/s^2}$. In the case of the Coriolis effect, the spatial area in between the interferometer arms will be adjusted by varying the release velocity of the atoms. With the possibility of high-resolution imaging at the beginning, in the middle and at the end of the free fall, mapping the 3D-trajectory of the atoms during the interferometer and therefore the impact from the Coriolis acceleration will be possible. This bias can then be corrected and its residual uncertainty contribution in QG-1 is estimated below $0.1\,\mathrm{nm/s^2}$. In order to approach the desired uncertainty below $3\,\mathrm{nm/s^2}$, contributions to the error budget from the shifts due to the blackbody radiation [119] and mean field interactions [120, 121] need to be analyzed as well. Due to their electric polarizability, atoms will interact coherently with the thermal electromagnetic field. Therefore, temperature gradients in the path of the interferometer, induce additional acceleration to the atomic ensemble. This acceleration can be mitigated by monitoring the temperature and modeling the introduced bias in the measured value of gravity via a ray tracing simulation of the thermal radiation and its residual uncertainty contribution is estimated below $1\,\mathrm{nm/s^2}$. Due to the high atomic densities in BECs, the impact from atom-atom interactions is not negligible. Therefore, an instability of the first beam splitting pulse will lead to a differential phase shift in between the interferometer arms. This is known as mean-field shift and introduces a bias in the measured value of gravity [30, 120, 121]. This bias will be minimized by letting the free expansion before the delta-kick collimation to reduce the density of the atomic ensemble as well as by minimizing the instabilities for the first interferometry pulse. Mean field shifts can be further investigated by deliberately altering the beam splitting ratio and the density of the atomic ensemble. With this, their contribution to uncertainty budget is estimated below $2\,\mathrm{nm/s^2}$. Taking these systematic studies into account, the total instrumental uncertainty of QG-1 is estimated to reach below $3\,\mathrm{nm/s^2}$.

Finally, QG-1 will establish its transportability and long-term stability by performing accurate gravity measurements in geodetic interesting sites. The performance of QG-1 will be evaluated in measurement campaigns in comparison to classical and superconducting gravimeters. QG-1 will contribute in the field modeling of the Fennoscandian land uplift region [41] in collaboration with the group of Jürgen Müller in the Institut für Erdmessung (IFE) at LUH. Furthermore, it will contribute in the hydro-geophysical modeling of groundwater variations in central Europe in collaboration with the group of Ludger Timmen in IFE. It is planned to be employed for measuring the temporal variations in the gravity due to the groundwater changes with an accuracy below $10\,\mathrm{nm/s^2}$ over a long period of a few months to years. With all these achieved, the capability of QG-1 in long-term measurement campaigns will be demonstrated and it will contribute to geodetic observations monitoring Earth's mass transport mechanism with a performance beyond state-of-the-art, which will open the route towards refining the Earth's mass model.

Bibliography

1. Schlippert, D., J. Hartwig, H. Albers, L. L. Richardson, C. Schubert, A. Roura, W. P. Schleich, W. Ertmer, and E. M. Rasel: 'Quantum Test of the Universality of Free Fall'. *Physical Review Letters* (May 22, 2014), vol. 112(20) (cit. on p. 3).
2. Becker, Dennis et al.: 'Space-borne Bose–Einstein condensation for precision interferometry'. *Nature* (Oct. 2018), vol. 562(7727): pp. 391–395 (cit. on pp. 3, 86).
3. Aguilera, D N et al.: 'STE-QUEST—test of the universality of free fall using cold atom interferometry'. *Classical and Quantum Gravity* (June 7, 2014), vol. 31(11): p. 115010 (cit. on p. 3).
4. Dimopoulos, Savas, Peter W. Graham, Jason M. Hogan, and Mark A. Kasevich: 'Testing General Relativity with Atom Interferometry'. *Physical Review Letters* (Mar. 15, 2007), vol. 98(11) (cit. on p. 3).
5. Zhou, Lin, Shitong Long, Biao Tang, Xi Chen, Fen Gao, Wencui Peng, Weitao Duan, Jiaqi Zhong, Zongyuan Xiong, Jin Wang, Yuanzhong Zhang, and Mingsheng Zhan: 'Test of Equivalence Principle at 10^{-8} Level by a Dual-Species Double-Diffraction Raman Atom Interferometer'. *Physical Review Letters* (July 2, 2015), vol. 115(1) (cit. on p. 3).
6. Hauth, M., C. Freier, V. Schkolnik, A. Senger, M. Schmidt, and A. Peters: 'First gravity measurements using the mobile atom interferometer GAIN'. *Applied Physics B* (Oct. 2013), vol. 113(1): pp. 49–55 (cit. on pp. 3, 33).
7. Hu, Zhong-Kun, Bu-Liang Sun, Xiao-Chun Duan, Min-Kang Zhou, Le-Le Chen, Su Zhan, Qiao-Zhen Zhang, and Jun Luo: 'Demonstration of an ultrahigh-sensitivity atom-interferometry absolute gravimeter'. *Physical Review A* (Oct. 8, 2013), vol. 88(4) (cit. on p. 3).
8. Bidel, Yannick, Olivier Carraz, Renée Charrière, Malo Cadoret, Nassim Zahzam, and Alexandre Bresson: 'Compact cold atom gravimeter for field applications'. *Applied Physics Letters* (Apr. 8, 2013), vol. 102(14): p. 144107 (cit. on p. 3).
9. Mayer-Gürr, Torsten, Annette Eicker, Enrico Kurtenbach, and Karl-Heinz Ilk: 'ITG-GRACE: Global Static and Temporal Gravity Field Models from GRACE Data'. *System Earth via Geodetic-Geophysical Space Techniques*. Ed. by Flechtner, Frank M., Thomas Gruber, Andreas Güntner, M. Mandea, Markus Rothacher, Tilo Schöne, and Jens Wickert. Advanced Technologies in Earth Sciences. Berlin, Heidelberg: Springer Berlin Heidelberg, 2010: pp. 159–168 (cit. on p. 3).

10. *iOSG™ Superconducting Gravity Meters - GWR Instruments, Inc. - San Diego, California*. URL: http://www.gwrinstruments.com/iosg-superconducting-gravity-meters.html (cit. on p. 3).
11. Lacoste, Lucien, Neal Clarkson, and George Hamilton: 'LACOSTE AND ROMBERG STABILIZED PLATFORM SHIPBOARD GRAVITY METER'. *GEOPHYSICS* (Feb. 1967), vol. 32(1): pp. 99–109 (cit. on p. 3).
12. Crossley, David, Jacques Hinderer, and Umberto Riccardi: 'The measurement of surface gravity'. *Reports on Progress in Physics* (Apr. 1, 2013), vol. 76(4): p. 046101 (cit. on p. 3).
13. *FG5-X Absolute Gravimeter User's Manual*. URL: http://microglacoste.com/wp-content/uploads/2018/01/FG5-X-Manual-115060001.pdf (cit. on p. 3).
14. *FG5-X ABSOLUTE GRAVITY METER Brochure*. URL: http://microglacoste.com/wp-content/uploads/2018/02/FG5-X-Brochure.pdf (cit. on p. 3).
15. Bordé, Ch.J.: 'Atomic interferometry with internal state labelling'. *Physics Letters A* (Sept. 1989), vol. 140(1): pp. 10–12 (cit. on pp. 3, 4, 8).
16. Kasevich, Mark and Steven Chu: 'Atomic interferometry using stimulated Raman transitions'. *Physical Review Letters* (July 8, 1991), vol. 67(2): pp. 181–184 (cit. on p. 3).
17. Peters, A, K Y Chung, and S Chu: 'High-precision gravity measurements using atom interferometry'. *Metrologia* (Feb. 2001), vol. 38(1): pp. 25–61 (cit. on p. 3).
18. Peters, Achim, Keng Yeow Chung, and Steven Chu: 'Measurement of gravitational acceleration by dropping atoms'. *Nature* (Aug. 1999), vol. 400(6747): pp. 849–852 (cit. on p. 4).
19. Freier, C, M Hauth, V Schkolnik, B Leykauf, M Schilling, H Wziontek, H-G Scherneck, J Müller, and A Peters: 'Mobile quantum gravity sensor with unprecedented stability'. *Journal of Physics: Conference Series* (June 2016), vol. 723: p. 012050 (cit. on pp. 4, 9).
20. Schmidt, M., A. Senger, M. Hauth, C. Freier, V. Schkolnik, and A. Peters: 'A mobile high-precision absolute gravimeter based on atom interferometry'. *Gyroscopy and Navigation* (July 2011), vol. 2(3): pp. 170–177 (cit. on p. 4).
21. Fang, B, I Dutta, P Gillot, D Savoie, J Lautier, B Cheng, C L Garrido Alzar, R Geiger, S Merlet, F Pereira Dos Santos, and A Landragin: 'Metrology with Atom Interferometry: Inertial Sensors from Laboratory to Field Applications'. *Journal of Physics: Conference Series* (June 2016), vol. 723: p. 012049 (cit. on p. 4).
22. Gillot, P, O Francis, A Landragin, F Pereira Dos Santos, and S Merlet: 'Stability comparison of two absolute gravimeters: optical versus atomic interferometers'. *Metrologia* (Oct. 1, 2014), vol. 51(5): pp. L15–L17 (cit. on p. 4).
23. Bodart, Q., S. Merlet, N. Malossi, F. Pereira Dos Santos, P. Bouyer, and A. Landragin: 'A cold atom pyramidal gravimeter with a single laser beam'. *Applied Physics Letters* (Mar. 29, 2010), vol. 96(13): p. 134101 (cit. on pp. 4, 9).

24. *Absolute Quantum Gravimeter*. URL: https://www.muquans.com/index.php/products/aqg (cit. on p. 4).

25. Louchet-Chauvet, Anne, Tristan Farah, Quentin Bodart, André Clairon, Arnaud Landragin, Sébastien Merlet, and Franck Pereira Dos Santos: 'The influence of transverse motion within an atomic gravimeter'. *New Journal of Physics* (June 28, 2011), vol. 13(6): p. 065025 (cit. on p. 4).

26. Lan, Shau-Yu, Pei-Chen Kuan, Brian Estey, Philipp Haslinger, and Holger Müller: 'Influence of the Coriolis Force in Atom Interferometry'. *Physical Review Letters* (Feb. 27, 2012), vol. 108(9) (cit. on p. 4).

27. Freier, Christian: 'Atom interferometry at geodetic observatories'. PhD thesis. June 1, 2017 (cit. on pp. 4, 9).

28. Schkolnik, V., B. Leykauf, M. Hauth, C. Freier, and A. Peters: 'The effect of wavefront aberrations in atom interferometry'. *Applied Physics B* (Aug. 2015), vol. 120(2): pp. 311–316 (cit. on p. 4).

29. Karcher, R., A. Imanaliev, S. Merlet, and Franck Pereira dos Santos: 'Improving the accuracy of atom interferometers with ultracold sources'. *New Journal of Physics* (Nov. 28, 2018), vol. 20(11): p. 113041 (cit. on pp. 4, 5).

30. Debs, J. E., P. A. Altin, T. H. Barter, D. Döring, G. R. Dennis, G. McDonald, R. P. Anderson, J. D. Close, and N. P. Robins: 'Cold-atom gravimetry with a Bose-Einstein condensate'. *Physical Review A* (Sept. 9, 2011), vol. 84(3) (cit. on pp. 5, 87).

31. Anderson, M. H., J. R. Ensher, M. R. Matthews, C. E. Wieman, and E. A. Cornell: 'Observation of Bose-Einstein Condensation in a Dilute Atomic Vapor'. *Science, New Series* (1995), vol. 269(5221): pp. 198–201 (cit. on pp. 5, 86).

32. Bradley, C. C., C. A. Sackett, J. J. Tollett, and R. G. Hulet: 'Evidence of Bose-Einstein Condensation in an Atomic Gas with Attractive Interactions'. *Physical Review Letters* (Aug. 28, 1995), vol. 75(9): pp. 1687–1690 (cit. on pp. 5, 86).

33. Davis, K B: 'Bose-Einstein Condensation in a Gas of Sodium Atoms'. *PHYSICAL REVIEW LETTERS* (1995), vol. 75(22): p. 5 (cit. on pp. 5, 86).

34. Andrews, M. R.: 'Observation of Interference Between Two Bose Condensates'. *Science* (Jan. 31, 1997), vol. 275(5300): pp. 637–641 (cit. on p. 5).

35. Shin, Y., M. Saba, T. A. Pasquini, W. Ketterle, D. E. Pritchard, and A. E. Leanhardt: 'Atom Interferometry with Bose-Einstein Condensates in a Double-Well Potential'. *Physical Review Letters* (Feb. 6, 2004), vol. 92(5) (cit. on p. 5).

36. Müntinga, H. et al.: 'Interferometry with Bose-Einstein Condensates in Microgravity'. *Physical Review Letters* (Feb. 25, 2013), vol. 110(9) (cit. on p. 5).

37. Kovachy, Tim, Jason M. Hogan, Alex Sugarbaker, Susannah M. Dickerson, Christine A. Donnelly, Chris Overstreet, and Mark A. Kasevich: 'Matter Wave Lensing to Picokelvin Temperatures'. *Physical Review Letters* (Apr. 8, 2015), vol. 114(14) (cit. on pp. 5, 86).

38. Folman, Ron, Peter Krüger, Jörg Schmiedmayer, Johannes Denschlag, and Carsten Henkel: 'Microscopic Atom Optics: From Wires to an Atom Chip'. *Advances In Atomic, Molecular, and Optical Physics*. Vol. 48. Elsevier, 2002: pp. 263–356 (cit. on p. 5).

39. Hänsel, W., P. Hommelhoff, T. W. Hänsch, and J. Reichel: 'Bose–Einstein condensation on a microelectronic chip'. *Nature* (Oct. 2001), vol. 413(6855): pp. 498–501 (cit. on p. 5).

40. Fortágh, József and Claus Zimmermann: 'Magnetic microtraps for ultracold atoms'. *Reviews of Modern Physics* (Feb. 1, 2007), vol. 79(1): pp. 235–289 (cit. on p. 5).

41. Müller, Jürgen, Majid Naeimi, Olga Gitlein, Ludger Timmen, and Heiner Denker: 'A land uplift model in Fennoscandia combining GRACE and absolute gravimetry data'. *Physics and Chemistry of the Earth, Parts A/B/C* (Jan. 1, 2012), vol. 53-54: pp. 54–60 (cit. on pp. 5, 87).

42. Berman, Paul R.: *Atom Interferometry*. Elsevier, 1997 (cit. on p. 7).

43. Cronin, Alexander D., Jörg Schmiedmayer, and David E. Pritchard: 'Optics and interferometry with atoms and molecules'. *Reviews of Modern Physics* (), vol. 81(3): pp. 1051–1129 (cit. on p. 7).

44. Bettles, Robert: 'Single Two-Level Atom'. *Cooperative Interactions in Lattices of Atomic Dipoles*. Cham: Springer International Publishing, 2017: pp. 15–37 (cit. on p. 7).

45. Abend, Sven: 'Atom-chip Gravimeter with Bose-Einstein Condensates'. (), vol.: p. 186 (cit. on pp. 8, 10, 36).

46. Bordé, Christian J.: 'Theoretical tools for atom optics and interferometry'. *Comptes Rendus de l'Académie des Sciences - Series IV - Physics* (Apr. 2001), vol. 2(3): pp. 509–530 (cit. on pp. 7, 8).

47. Itano, W. M., J. C. Bergquist, J. J. Bollinger, J. M. Gilligan, D. J. Heinzen, F. L. Moore, M. G. Raizen, and D. J. Wineland: 'Quantum projection noise: Population fluctuations in two-level systems'. *Physical Review A* (May 1, 1993), vol. 47(5): pp. 3554–3570 (cit. on p. 9).

48. Allan, D.W.: 'Statistics of atomic frequency standards'. *Proceedings of the IEEE* (1966), vol. 54(2): pp. 221–230 (cit. on p. 9).

49. Santarelli, G., Ph. Laurent, P. Lemonde, A. Clairon, A. G. Mann, S. Chang, A. N. Luiten, and C. Salomon: 'Quantum Projection Noise in an Atomic Fountain: A High Stability Cesium Frequency Standard'. *Physical Review Letters* (June 7, 1999), vol. 82(23): pp. 4619–4622 (cit. on p. 9).

50. Le Gouët, J., T.E. Mehlstäubler, J. Kim, S. Merlet, A. Clairon, A. Landragin, and F. Pereira Dos Santos: 'Limits to the sensitivity of a low noise compact atomic gravimeter'. *Applied Physics B* (Aug. 1, 2008), vol. 92(2): pp. 133–144 (cit. on p. 9).

51. Abend, S., M. Gebbe, M. Gersemann, H. Ahlers, H. Müntinga, E. Giese, N. Gaaloul, C. Schubert, C. Lämmerzahl, W. Ertmer, W. P. Schleich, and E. M. Rasel: 'Atom-Chip Fountain Gravimeter'. *Physical Review Letters* (Nov. 11, 2016), vol. 117(20) (cit. on pp. 9, 13, 36, 86).

52. Prodan, John V., William D. Phillips, and Harold Metcalf: 'Laser Production of a Very Slow Monoenergetic Atomic Beam'. *Physical Review Letters* (Oct. 18, 1982), vol. 49(16): pp. 1149–1153 (cit. on p. 10).

53. Schoser, J., A. Batär, R. Löw, V. Schweikhard, A. Grabowski, Yu. B. Ovchinnikov, and T. Pfau: 'Intense source of cold Rb atoms from a pure two-dimensional magneto-optical trap'. *Physical Review A* (Aug. 26, 2002), vol. 66(2) (cit. on p. 10).

54. Reichel, Jakob and Vladan Vuletic: *Atom Chips*. 1. Weinheim, Germany: Wiley-VCH, Feb. 9, 2011. 445 pp. (cit. on pp. 10, 11, 22, 68, 100).

55. Wildermuth, S., P. Krüger, C. Becker, M. Brajdic, S. Haupt, A. Kasper, R. Folman, and J. Schmiedmayer: 'Optimized magneto-optical trap for experiments with ultracold atoms near surfaces'. *Physical Review A* (Mar. 17, 2004), vol. 69(3) (cit. on pp. 10, 57, 68).

56. Dieckmann, K., R. J. C. Spreeuw, M. Weidemüller, and J. T. M. Walraven: 'Two-dimensional magneto-optical trap as a source of slow atoms'. *Physical Review A* (Nov. 1, 1998), vol. 58(5): pp. 3891–3895 (cit. on pp. 10, 18, 57, 61).

57. Chaudhuri, Saptarishi, Sanjukta Roy, and C. S. Unnikrishnan: 'Realization of an intense cold Rb atomic beam based on a two-dimensional magneto-optical trap: Experiments and comparison with simulations'. *Physical Review A* (Aug. 18, 2006), vol. 74(2) (cit. on pp. 10, 58, 62, 63, 65).

58. Metcalf, Harold J. and Peter Van der Straten: *Laser cooling and trapping*. Graduate texts in contemporary physics. New York: Springer, 1999. 323 pp. (cit. on pp. 10, 24, 60, 61, 71, 78).

59. Petrich, Wolfgang, Michael H. Anderson, Jason R. Ensher, and Eric A. Cornell: 'Stable, Tightly Confining Magnetic Trap for Evaporative Cooling of Neutral Atoms'. *Physical Review Letters* (Apr. 24, 1995), vol. 74(17): pp. 3352–3355 (cit. on pp. 10, 11).

60. Chu, Steven, L. Hollberg, J. E. Bjorkholm, Alex Cable, and A. Ashkin: 'Three-dimensional viscous confinement and cooling of atoms by resonance radiation pressure'. *Physical Review Letters* (July 1, 1985), vol. 55(1): pp. 48–51 (cit. on pp. 10, 74).

61. Ketterle, W. and D. E. Pritchard: 'Trapping and focusing ground state atoms with static fields'. *Applied Physics B Photophysics and Laser Chemistry* (May 1992), vol. 54(5): pp. 403–406 (cit. on p. 11).

62. Wing, William H.: 'On neutral particle trapping in quasistatic electromagnetic fields'. *Progress in Quantum Electronics* (Jan. 1984), vol. 8(3): pp. 181–199 (cit. on p. 11).

63. Migdall, Alan L., John V. Prodan, William D. Phillips, Thomas H. Bergeman, and Harold J. Metcalf: 'First Observation of Magnetically Trapped Neutral Atoms'. *Physical Review Letters* (June 17, 1985), vol. 54(24): pp. 2596–2599 (cit. on p. 11).

64. Brink, D. M. and C. V. Sukumar: 'Majorana spin-flip transitions in a magnetic trap'. *Physical Review A* (Sept. 11, 2006), vol. 74(3) (cit. on p. 11).

65. Gott, Yu V., M. S. Ioffe, and V. G. Telkovskii: 'SOME NEW RESULTS ON CONFINEMENT IN MAGNETIC TRAPS'. *Nuclear Fusion (Austria)* (Jan. 1, 1962), vol. Vol: Suppl. 2, Pt. 3 (cit. on p. 11).

66. Pritchard, David E.: 'Cooling Neutral Atoms in a Magnetic Trap for Precision Spectroscopy'. *Physical Review Letters* (Oct. 10, 1983), vol. 51(15): pp. 1336–1339 (cit. on p. 11).

67. Esslinger, Tilman, Immanuel Bloch, and Theodor W. Hänsch: 'Bose-Einstein condensation in a quadrupole-Ioffe-configuration trap'. *Physical Review A* (Oct. 1, 1998), vol. 58(4): R2664–R2667 (cit. on p. 11).

68. Zhang, Dong-Fang, Tian-You Gao, Ling-Ran Kong, Kai Li, and Kai-Jun Jiang: 'Production of Rubidium Bose—Einstein Condensate in an Optically Plugged Magnetic Quadrupole Trap'. *Chinese Physics Letters* (July 2016), vol. 33(7): p. 076701 (cit. on p. 11).

69. Rudolph, Jan, Waldemar Herr, Christoph Grzeschik, Tammo Sternke, Alexander Grote, Manuel Popp, Dennis Becker, Hauke Müntinga, Holger Ahlers, Achim Peters, Claus Lämmerzahl, Klaus Sengstock, Naceur Gaaloul, Wolfgang Ertmer, and Ernst M Rasel: 'A high-flux BEC source for mobile atom interferometers'. *New Journal of Physics* (June 1, 2015), vol. 17(6): p. 065001 (cit. on pp. 13, 17, 24, 57, 85, 86).

70. Ménoret, Vincent, Pierre Vermeulen, Nicolas Le Moigne, Sylvain Bonvalot, Philippe Bouyer, Arnaud Landragin, and Bruno Desruelle: 'Gravity measurements below $10^{-9}g$ with a transportable absolute quantum gravimeter'. *Scientific Reports* (Aug. 17, 2018), vol. 8(1): p. 12300 (cit. on p. 13).

71. Herr, Waldemar: 'Eine kompakte Quelle quantenentarteter Gase hohen Flusses für die Atominterferometrie unter Schwerelosigkeit'. PhD thesis. 2013 (cit. on pp. 14, 18, 25, 30, 76, 85).

72. Seidel, Stephan Tobias: 'Eine quelle für die interferometrie mit Bose-Einsteinkondensaten auf höhenforschungsraketen'. PhD thesis. 2014 (cit. on pp. 14, 15, 19, 22, 25, 43, 70, 76, 85).

73. Straessle, Rahel, Matthieu Pellaton, Yves Petremand, Danick Briand, Christoph Affolderbach, Gaetano Mileti, and N. F. de Rooij: 'Low-temperature indium hermetic sealing of alkali vapor-cells for chip-scale atomic clocks'. *2012 IEEE 25th International Conference on Micro Electro Mechanical Systems (MEMS)* (2012), vol.: pp. 361–364 (cit. on p. 14).

74. Bhaskar, N. D. and C. M. Kahla: 'Cesium Gettering by Graphite—Improvement in the Gettering Efficiency'. IEEE Transactions on Ultrasonics, Ferroelectrics, and Frequency Control. (1990), vol. (cit. on p. 19).

75. Wildermuth, Stephan: 'One-dimensional Bose-Einstein condensates in micro-traps'. PhD thesis. 2005 (cit. on p. 19).

76. Moore, John H., Christopher C. Davis, Michael A. Coplan, and Sandra C. Greer: *Building Scientific Apparatus*. 4 edition. Cambridge, UK ; New York: Cambridge University Press, July 20, 2009. 658 pp. (cit. on p. 21).

77. Barbey, Jan Philipp: *Ein Atomchip hohen Flusses für die Quantengravimetrie*. masterthesis (cit. on pp. 30, 65, 70, 71, 81).

78. Custum design by B. Piest, 2016, unpublished (cit. on p. 31).

79. Rudolph, Jan: 'Matter-Wave Optics with Bose-Einstein Condensates in Microgravity'. PhD thesis. 2016 (cit. on pp. 33, 64, 70).

80. Farah, T., C. Guerlin, A. Landragin, Ph. Bouyer, S. Gaffet, F. Pereira Dos Santos, and S. Merlet: 'Underground operation at best sensitivity of the mobile LNE-SYRTE cold atom gravimeter'. *Gyroscopy and Navigation* (Oct. 2014), vol. 5(4): pp. 266–274 (cit. on p. 33).

81. Lautier, J., L. Volodimer, T. Hardin, S. Merlet, M. Lours, F. Pereira Dos Santos, and A. Landragin: 'Hybridizing matter-wave and classical accelerometers'. *Applied Physics Letters* (Oct. 6, 2014), vol. 105(14): p. 144102 (cit. on p. 33).

82. Zhou, Min-Kang, Zhong-Kun Hu, Xiao-Chun Duan, Bu-Liang Sun, Le-Le Chen, Qiao-Zhen Zhang, and Jun Luo: 'Performance of a cold-atom gravimeter with an active vibration isolator'. *Physical Review A* (Oct. 31, 2012), vol. 86(4): p. 043630 (cit. on p. 33).

83. Steck, Daniel: *Rubidium 87 D line data, revision 2.1.5, 13 January 2015*. URL: `https://steck.us/alkalidata/rubidium87numbers.pdf` (cit. on pp. 35, 37, 49, 50, 55, 59, 78).

84. Carraz, O., F. Lienhart, R. Charrière, M. Cadoret, N. Zahzam, Y. Bidel, and A. Bresson: 'Compact and robust laser system for onboard atom interferometry'. *Applied Physics B* (Aug. 6, 2009), vol. 97(2): p. 405 (cit. on p. 36).

85. Lienhart, F., S. Boussen, O. Carraz, N. Zahzam, Y. Bidel, and A. Bresson: 'Compact and robust laser system for rubidium laser cooling based on the frequency doubling of a fiber bench at 1560 nm'. *Applied Physics B* (Nov. 2, 2007), vol. 89(2): pp. 177–180 (cit. on p. 36).

86. Ménoret, V., R. Geiger, G. Stern, N. Zahzam, B. Battelier, A. Bresson, A. Landragin, and P. Bouyer: 'Dual-wavelength laser source for onboard atom interferometry'. *Optics Letters* (Nov. 1, 2011), vol. 36(21): pp. 4128–4130 (cit. on p. 36).

87. Supplee, James M., Edward A. Whittaker, and Wilfried Lenth: 'Theoretical description of frequency modulation and wavelength modulation spectroscopy'. *Applied Optics* (Sept. 20, 1994), vol. 33(27): pp. 6294–6302 (cit. on p. 36).

88. Steck, Daniel: *Rubidium 85 D line data, revision 2.1.6,20 September 2013*. URL: `https://steck.us/alkalidata/rubidium85numbers.pdf` (cit. on p. 37).

89. Theron, Fabien, Olivier Carraz, Geoffrey Renon, Yannick Bidel, Nassim Zahzam, Malo Cadoret, and Alexandre Bresson: 'Narrow linewidth single laser source system for onboard atom interferometry'. *Applied Physics B* (Jan. 2015), vol. 118(1): pp. 1–5 (cit. on p. 36).

90. Müller, Holger, Sheng-wey Chiow, Quan Long, Sven Herrmann, and Steven Chu: 'Atom Interferometry with up to 24-Photon-Momentum-Transfer Beam Splitters'. *Physical Review Letters* (May 8, 2008), vol. 100(18) (cit. on p. 36).

91. Grove, Nina: *A fiber-based laser system for a transportable quantum gravimeter*. masterthesis. Feb. 16, 2017 (cit. on pp. 36, 38, 41, 43, 44, 58, 73).

92. Shirley, Jon H.: 'Modulation transfer processes in optical heterodyne saturation spectroscopy'. *Optics Letters* (Nov. 1, 1982), vol. 7(11): p. 537 (cit. on p. 37).

93. Snyder, J. J., R. K. Raj, D. Bloch, and M. Ducloy: 'High-sensitivity nonlinear spectroscopy using a frequency-offset pump'. *Optics Letters* (Apr. 1, 1980), vol. 5(4): p. 163 (cit. on p. 37).

94. McCarron, D. J., S. A. King, and S. L. Cornish: 'Modulation transfer spectroscopy in atomic rubidium'. *Measurement Science and Technology* (Oct. 1, 2008), vol. 19(10): p. 105601 (cit. on p. 37).

95. Wendrich, Thijs: 'LASUS - Laser System unter Schwerlosigkeit'. (), vol. (cit. on p. 43).

96. Popp, Manuel André: 'Compact, low-noise current drivers for quantum sensors with atom chips'. doctoralThesis. Hannover : Institutionelles Repositorium der Leibniz Universität Hannover, 2018 (cit. on pp. 43, 45, 46).

97. Matthias, Jonas: 'In preparation'. PhD thesis (cit. on pp. 43, 46, 79, 85).

98. 'Shutter driver version 1.0'. Custum design by N. Heine, 2018, unpublished (cit. on p. 44).

99. 'TBus Microwave version 1.0'. Custum design by H. Abedi, 2018, unpublished (cit. on p. 44).

100. Gehm, M. E., K. M. O'Hara, T. A. Savard, and J. E. Thomas: 'Dynamics of noise-induced heating in atom traps'. *Physical Review A* (Nov. 1, 1998), vol. 58(5): pp. 3914–3921 (cit. on p. 45).

101. Wesche, Jannik: 'Entwicklung und Charakterisierung eines Abbildungssystems für die Absorptionsdetektion'. (), vol.: p. 42 (cit. on p. 50).

102. Reichel, J., W. Hänsel, and T. W. Hänsch: 'Atomic Micromanipulation with Magnetic Surface Traps'. *Physical Review Letters* (Oct. 25, 1999), vol. 83(17): pp. 3398–3401 (cit. on p. 57).

103. Demtröder, Wolfgang: *Atoms, Molecules and Photons: An Introduction to Atomic-, Molecular- and Quantum Physics*. 2nd ed. Graduate Texts in Physics. Berlin Heidelberg: Springer-Verlag, 2010 (cit. on p. 58).

104. Loudon, Rodney: *The Quantum Theory of Light*. 3 edition. Oxford ; New York: Oxford University Press, Nov. 23, 2000. 448 pp. (cit. on p. 59).

105. Tiecke, T. G., S. D. Gensemer, A. Ludewig, and J. T. M. Walraven: 'A high-flux 2D MOT source for cold lithium atoms'. *Physical Review A* (July 20, 2009), vol. 80(1) (cit. on p. 61).

106. Gilowski, M., Ch. Schubert, M. Zaiser, W. Herr, T. Wübbena, T. Wendrich, T. Müller, E.M. Rasel, and W. Ertmer: 'Narrow bandwidth interference filter-stabilized diode laser systems for the manipulation of neutral atoms'. *Optics Communications* (Dec. 2007), vol. 280(2): pp. 443–447 (cit. on p. 64).

107. Abend, Sven: *GROSSFLÄCHIGE ATOMINTERFEROMETER FÜR DIE INERTIALSENSORIK*. Diplomarbeit (cit. on p. 64).

108. Becker, Dennis: *Demonstration einer neuartigen kompakten chip-basierten Quelle kalter Atome*. masterthesis. Nov. 17, 2011 (cit. on p. 65).

109. Atutov, S. N., R. Calabrese, V. Guidi, B. Mai, A. G. Rudavets, E. Scansani, L. Tomassetti, V. Biancalana, A. Burchianti, C. Marinelli, E. Mariotti, L. Moi, and S. Veronesi: 'Fast and efficient loading of a Rb magneto-optical trap using light-induced atomic desorption'. *Physical Review A* (May 22, 2003), vol. 67(5) (cit. on p. 67).

110. Gozzini, A., F. Mango, J. H. Xu, G. Alzetta, F. Maccarrone, and R. A. Bernheim: 'Light-induced ejection of alkali atoms in polysiloxane coated cells'. *Il Nuovo Cimento D* (May 1, 1993), vol. 15(5): pp. 709–722 (cit. on p. 67).

111. Dalibard, J. and C. Cohen-Tannoudji: 'Laser cooling below the Doppler limit by polarization gradients: simple theoretical models'. *Journal of the Optical Society of America B* (Nov. 1, 1989), vol. 6(11): p. 2023 (cit. on p. 74).

112. Arora, P., S. B. Purnapatra, A. Acharya, R. Kumar, and A. Sen Gupta: 'Measurement of Temperature of Atomic Cloud Using Time-of-Flight Technique'. *MAPAN* (Mar. 2012), vol. 27(1): pp. 31–39 (cit. on p. 75).

113. Ketterle, W., D. S. Durfee, and D. M. Stamper-Kurn: 'Making, probing and understanding Bose-Einstein condensates'. *arXiv:cond-mat/9904034* (Apr. 1, 1999), vol. (cit. on p. 78).

114. Ammann, Hubert and Nelson Christensen: 'Delta Kick Cooling: A New Method for Cooling Atoms'. *Physical Review Letters* (Mar. 17, 1997), vol. 78(11): pp. 2088–2091 (cit. on p. 86).

115. Chiow, Sheng-wey, Tim Kovachy, Hui-Chun Chien, and Mark A. Kasevich: '102$\hbar k$ large area atom interferometers'. *Physical Review Letters* (Sept. 23, 2011), vol. 107(13): p. 130403 (cit. on p. 86).

116. Müller, Holger, Sheng-wey Chiow, Quan Long, Sven Herrmann, and Steven Chu: 'Atom Interferometry with up to 24-Photon-Momentum-Transfer Beam Splitters'. *Physical Review Letters* (May 8, 2008), vol. 100(18) (cit. on p. 86).

117. Szigeti, S S, J E Debs, J J Hope, N P Robins, and J D Close: 'Why momentum width matters for atom interferometry with Bragg pulses'. *New Journal of Physics* (Feb. 3, 2012), vol. 14(2): p. 023009 (cit. on p. 86).

118. Richardson, L. L. et al.: 'Opto-mechanical resonator-enhanced atom interferometry'. *arXiv:1902.02867 [physics, physics:quant-ph]* (Feb. 7, 2019), vol. (cit. on p. 86).

119. Haslinger, Philipp, Matt Jaffe, Victoria Xu, Osip Schwartz, Matthias Sonnleitner, Monika Ritsch-Marte, Helmut Ritsch, and Holger Müller: 'Attractive force on atoms due to blackbody radiation'. *Nature Physics* (Mar. 2018), vol. 14(3): pp. 257–260 (cit. on p. 87).

120. Jannin, Raphaël, Pierre Cladé, and Saïda Guellati-Khélifa: 'Phase shift due to atom-atom interactions in a light-pulse atom interferometer'. *Physical Review A* (July 13, 2015), vol. 92(1) (cit. on p. 87).

121. Jamison, Alan O., J. Nathan Kutz, and Subhadeep Gupta: 'Atomic interactions in precision interferometry using Bose-Einstein condensates'. *Physical Review A* (Oct. 28, 2011), vol. 84(4) (cit. on p. 87).

122. Treutlein, Philipp: 'Coherent manipulation of ultracold atoms on atom chips'. PhD thesis. Ludwig-Maximilians-Universität München, Apr. 1, 2008 (cit. on p. 99).

123. *ASME - STANDARDS - Surface Texture (Surface Roughness, Waviness, and Lay)*. URL: `https://www.asme.org/products/codes-standards/b461-2009-surface-texture-surface-roughness` (cit. on p. 99).

124. Madou, Marc J.: *Fundamentals of Microfabrication and Nanotechnology, Three-Volume Set*. 3 edition. Boca Raton, Fla: CRC Press, Aug. 1, 2011. 1992 pp. (cit. on p. 100).

A Production of the 3-layer atom-chip assembly

A summary of the process of assembling the QG-1 atom-chip setup is provided in this chapter. The recipe used for the microfabrication of the base and science layers is adopted from [122]. The important specifications and challenges in each step of the production are described in the following.

A.1 Microfabrication of the base and science chips

A.1.1 Substrate

As the substrate for the base and science layers, an aluminium nitride wafer (HEBO spezialglas) is used. Aluminium nitride material is chosen, since it is electrically isolated and provides a high heat conductivity of 170 W/mK for the dissipation of the heat generated by the current carrying wires. The substrates are 635 μm thick and are delivered as 3 inch diameter wafers. They are polished on both sides and have a very small surface roughness of less than 1 µ"Ra[1]. In the following process, the cleaning of the wafers has been always done in three steps. They are first cleaned in an isopropanol and then in an acetone ultrasonic bath at 45°C for 5 minutes each and finally in an oxygen plasma cleaner (Plasmaverascher 100-E[2]) by 200 W and 1.2 mbar for 5 min.

A.1.2 Evaporative coating

In order to grow gold structures on a wafer via photolithography procedure, an initial thin layer of gold needs to be coated on the substrate to form the cathode for the electroplating process. For this, first a thin layer of titanium has to be coated as an adhesion layer between the aluminium nitride substrate and the gold layer. After cleaning of the wafers, a 2 nm thick layer of titanium is deposited on the substrate with a rate of 1 A°/s inside an evaporative cooler (Congo vac[3]). Directly afterwards, a 50 nm thick gold layer with a rate of 2 A°/s is deposited.

A.1.3 Photolithography

In the optical lithography process, light is used to transfer a pattern from a photomask to a light-sensitive layer, photo-resist, which is coating a substrate. After the process, a positive photoresist can be removed from the exposed area by a photographic developer and this area on the chip can be used to deposit materials [122].

For the QG-1 chip, after the cleaning and pre-heating the wafers at 100°C, a 10 μm layer of positive photoresist (Micro resist technology ma-p 1275) is spin coated on this wafer. After 20 minutes of rehydration, the pattern from a chrome photomask (Compugraphics

1 Ra is a representation of surface roughness and is calculated from the arithmetic average of the profile height deviations from the mean line[123].
2 Facilitated by LNQE.
3 Facilitated by PTB.

Jena) is transfered on the photoresist. This is done by exposing to a 365 nm light with an intensity of 8 mW/cm^2 in a mask aligner (SPS MA6[1]) for 80 s. The theoretical resolution obtained in a contact lithography process defines the minimum resolved dimension b_{min}, which is limited by the light diffraction at the edges of the photomask. This diffractions can be reduced by minimizing the gap between the photomask and the photoresist layer. The resulted resolution can be calculated from the formula[124]

$$b_{min} = \frac{3}{2}\sqrt{\lambda\left(s + \frac{z}{2}\right)} \tag{A.1}$$

where λ is the wavelength of the exposed light, s is the gap between the mask and the resist and z is the height of the resist. The theoretical resolution is calculated as 2 μm with the parameters used for the lithrography process in the QG-1 chip. This is sufficient since the smallest wire structure has a width of 50 μm and the minimum distance between two wire structures is equal to 25 μm. After 2 minutes of rehydration, the resist is removed from the area exposed to the light by developing for 100 s (micro resist technology ma-D 331). The pre-baking temperature, rehydration times, lithrography light intensity and exposing time and the developing time depend on many parameters including the viscosity of the photoresist, the humidity of the environment and the wavelength of the exposing light. The optimum parameters are found for the growth of 10 μm of the resist and attaining sharp edges after the development process.

A.1.4 Electroplating

Using the electroplating technique, gold wires are deposited on the areas, which are not covered with the photoresist. For this, the gold layer on the wafer is used as the cathode and a 100 mm × 100 mm platinized titanium mesh (Metakem) is employed as the anode. These are placed inside a 500 ml of ammonium gold sulfite solution containing 15 g Au/l. When a voltage is applied through the electrolytic cell, the gold ions from the solution will be deposited on the cathode surface. The temperature of the solution is kept constant at 58.5°C by keeping it inside a water bath. Furthermore, the solution is stirred during the whole process with a motor to keep the ion density in the solution constant and achieve a more homogeneous electroplated surface. The height of the deposited gold for a cathode surface of S, which is electroplated for a time t with a current of I is calculated from the Faraday's law, which for the gold ions can be simplified as [54]

$$h = 1.1 \times 10^{-10}\frac{m^3}{As} \times \frac{It}{S}. \tag{A.2}$$

Using this formula, the required process time is estimated. The gold surface area in the case of the base chip is about 1526.5 mm^2 and therefore with a 50 mA of current flowing for 50 minutes, 10.8 μm of gold should grow. In the case of the science chip, three science chip structures are printed on one mask, resulting to 1094.5 mm^2 of gold pattern on the substrate. With a 30 mA of current flowing for 70 minutes, 12.7 μm gold wire should

1 Facilitated by LNQE.

grow. The height of the gold structure and its surface quality is afterwards measured by a dual core 3D-measuring microscope (Leica DCM3D[1]). The measured heights are equal to 11.25 μm and 13.25 μm for the base and science chip respectively, which are slightly higher than the calculated values.

A.1.5 Etching

After the wires are grown, the adhesion layers of 50 nm of gold and 2 nm of titanium are removed via wet etching process. This is performed in three steps: After pre-cleaning the wafers, the residual photoresist is removed by soaking the wafers for 60 s in a piranha solution ($H_2SO_4(95-98\%) : H_2O_2(29-32\%)$) with a volume ratio of (4 : 1). In step 2, by soaking the chip for 40 s in an aqua regia solvant ($H_2O : HCl(37\%) : HNO_3(70\%)$) with a volume ratio of (1 : 3 : 1), the 50 nm of the gold layer is etched. In the last step, the 2 nm titanium layer is removed by 30 s soaking in the piranha solvant.

A.1.6 Dicing and cutting

After the wafers are fabricated, the science chips are diced with a diamond blade and the base chips are laser cut (A.l.l Lasertechnik). Before the cutting process, the wafers are covered with photoresist as a protection for the chip surface.

A.2 Gluing of the 3-layer atom-chip assembly

The three layers of the atom chip are assembled on a mount machined in the mechanical workshop of the institute. The chip mount is made of oxygen-free copper (Luvata Cu-OFE OFHC) with a low outgassing rate and high thermal conductivity. In the first step, the mesoscopic wires are winded inside the inlets machined on the surface of the copper mount. First, a wire is winded seven times in the form of U. This wire is looped at a distance of 8 cm away from the mount in the back side to prevent disturbance in the generated magnetic field. The three triple wires for the mesoscopic H-structure are winded in the same manner. A few drops of a thermal conductive and electric isolated UHV-compatible expoy (Epotek H77) is used under the U-wires to provide the thermal dissipation through the copper mount. To cure this epoxy, the setup is heated to 120°C for two hours. The heating starts after 4 hours of waiting for the air bubbles to leave the setup, because the remained air bubbles will later degas in the vacuum setup lowering the UHV quality. Afterwards, a few drops of the same epoxy is used on the surface of the copper mount and the base chip is placed on top. To prevent any thermal shock on the aluminum nitride wafer, the heating and cooling during the cure program are done with slower ramps in a total time of 9 hours. In the next step, the science chip is glued on the base chip with the same technique.

A.3 Dielectric mirror

The upper surface of the atom chip needs to be highly reflective at 45° for 780 nm light. In the QG-1 experiment, special care is taken to improve the surface quality of the reflecting surface (section 3.4.1). This surface is a 2 μm thick dielectric mirror (OIB Jena) with a

1 Facilitated by LNQE.

reflectivity better than 99.5% at 45° for 780 nm light. The mirror is delivered on a glass or a quartz substrates. In order to transfer this mirror on the surface of the atom chip, first a square slightly larger than the size of the science chip is cut using a scalpel. A few drops of an optic epoxy (Epotek 353ND) is applied on the surface of the science chip and the dielectric mirror's substrate is placed on top. After the cure time, the substrate is removed. One limitation in acquiring a high surface quality in the previous generations of the atom chips was due to the remained dust particles on the substrate surface before growing the dielectric layers. Through the gap caused in the dielectric layers due to these dust particles, the epoxy could flow and reach the substrate during the cure time. This leaves lens shaped epoxy over the reflective surface of the atom chip. To prevent this, a more viscous epoxy is applied. The viscosity of the epoxy is increased by preheating it to 75°C before applying on the chip surface. In this case, the atom chip and the dielectric mirror's substrate should be pre-heated correspondingly to prevent a thermal shock, which would lead to an inhomogeneity and fine cracks on the dielectric layer. This specially occurs because of the different thermal expansion coefficients of the atom chip, the glass or quartz substrate and the dielectric layers. Using a more viscous epoxy has an additional advantage of producing a thicker epoxy layer between the science chip and the mirror. This reduces the inhomogeneity of the reflective surface due to the wire structure on the science chip. The recipe of this process is described in the following.

First, the chip assembly and the mirror substrate are heated to 100°C and the epoxy is heated to 75°C. A drop of the glue is applied and the pre-cut dielectric mirror is pressed on the surface. The cure program starts after 4 hours of waiting time. Afterwards, the assembly is heated to 100°C with small temperature gradients of 2°C per hour. After the cure, the substrate is removed. The surface quality is measured using a Leica DCM 3D and the height measurement is performed with a profilometer (Dektak 6M). The result of these measurements are presented in section 3.4.1.

A.4 Bounding of the wires

The electrical contacts of the science chip wires are provided through their connection to the base chip wires. This is accomplished using 25.4 μm thick wire ribbons with a width of 381 μm (Materion). Parallel gap welding process (Miyachi Unitek) is used to bond the ribbons to the chip wires. For this, the gold ribbons are pressed by the two parts of the anodes from the welding tip (Unitip UTM224C Miyachi Unitek) and a weld pulse with a power of 110 W flows for 17 ms from one electrode to the other through the gold ribbon. Melting of the surface in these points due to the produced heat bonds the ribbon to the wire. This process is repeated twice at each point. On the wire structure of the base chip, small holes with a diameter of 1 mm are cut. Kapton isolated wires with a core diameter 0.75 mm are glued to these points using electrical conductive HUV-compatible epoxy (Epotek H21D). This epoxy is cured at a temperature of 100°C. The connections are described in section 3.4.1.

After the chip assembly is constructed, the copper mount is placed inside the titanium chip flange with a tight contact for a high heat dissipation. Eight titanium screws are used to fix the atom-chip assembly to the titanium mount.

List of Figures

List of Tables

Acronyms

Notation	Description
ALP	Afocal lens pair
AOM	Acousto optic modulator
AQG	Absolute quantum gravimeter
AR	Anti-reflective
ARP	Adiabatic rapid passage
BEC	Bose-Einstein condensate
CAD	Computer-aided design
CAG	Cold atom gravimeter
CCD	Charge-coupled device
CF	Conflat flange
cMOT	Compressed magneto-optical trap
DC	Directional coupler
DDS	Direct digital synthesizer
DFB	Distributed feedback
DKC	Delta-kick collimation
ECDL	External cavity diode laser
EOM	Electro optic modulator
FA	Fiber amplifier
FET	Field-effect transistor
FOV	Field of view
FPGA	Field programmable gate array
GAIN	Gravimetric atom interferometer
geo-Q	Geodesy with Quantum sensors
HPF	High pass filter
HR	High-reflective

Notation	Description
IFE	Institut für Erdmessung
IGP	Ion getter pump
IQ	Institut für Quantenoptik
LED	Light-emitting diode
LIAD	Light induced atom desorption
LUH	Leibniz Universität Hannover
MAIUS	Materiewellen-Interferometrie unter Schwerelosigkeit
MOT	Magneto-optical trap
MTS	Modulation transfer spectroscopy
ND	Neutral-density
NEG	Non evaporable getter
OI	Optical isolator
PBS	Polarizing beam splitter
PD	Photodiode
PGC	Polarization gradient cooling
PID	Proportional-integral-derivative
PLL	Phase-locked loop
PM	Polarization maintaining
PPLN	Periodically poled lithium niobate
PSD	Phase-space density
QG-1	Quantum gravimeter-1
QPN	Quantum projection noise
QUANTUS	Quantensysteme unter Schwerelosigkeit
QUIC	Quadrupole-Ioffe-configuration
rf	Radio frequency

Notation	Description
SHG	Second harmonic generation
SMA	Subminiature version A
SNR	Signal-to-noise-ratio
TA	Tapered amplifier
TOF	Time-of-flight
TOP	Time-averaged-orbiting-potential
TSP	Titanium sublimation pump
UHV	Ultra-high vacuum
UV	Ultraviolet
VCO	Voltage controlled oscillator
VI	Virtual instrumentation

Acknowledgments

Here I wish to thank all the people who have been directly or indirectly influenced the work of this thesis. First I want to thank Ernst Rasel for the opportunity to join the group from far away and that he put the trust on me to start the QG-1 experiment from scratch. Also, for the chance to visit some beneficial international conferences. Second I want to thank my ancillary supervisor Silke Ospelkaus. I want to thank my additional thesis referees Rainer Dumke and Dennis Schlippert for reading this thesis. To thank Waldemar Herr for his scientific support and help since when I joined the team and for putting the faith in me. To thank the QG-1 team, specially Jonas Matthias who has started the journey on the experiment with me, Nina Heine for her awesome contributions both as a master and now as a PhD student. May the $3\,\mathrm{nm/s^2}$ actualize by you. Philipp Barbey for being a great master student and simulating our chip trap. The former members, Gunnar Tackmann, Jannik Wesche and Janina Molkenthin for pushing things forward. To Sven Abend, Christian Schubert, Sebastian Bode, Baptist Piest, Dipankar Natt, Maike Lachmann, Manuel Popp, Holger Ahlers, Dennis Becker and Thijs Wendrich for the scientific discussions and that they always suggested their help when I asked for. To Matthias Gersemann, Hendrik Heine and Melanie Le Gonidec for being the greatest people we could share a lab with. To Étienne Wodey, Christian Meiners and Dorothee Tell for being the best neighbors. To Jung-Bin Wang for the time we spent together making the QG-1 and MAIUS-B atom chips. Thanks to Martina Wahnschaffe, Amado Bautista and Stephan Seidel for their patience and time to teach us how to fabricate a chip and to Christian Ospelkaus for making this possible. To the PTB and LNQE staffs for letting me use their clean rooms and facilities. To everyone who were great friends making the work fun in all these years, Dominika Fim, Logan Richardson, Henning Albers, Felix Kösel, Robin Corgier, Sina Loriani, Naceur Gaaloul, Sirine Amri, Kai Frye, Torben Schulze, Maraike Hetzel, Wuying She, Mariia Stepanova, Kai Voges, Erik Schwanke, Paul Kaebert and Philipp Gersema. Thanks for all the several and fun events.

I want to thank Miss Göldner-Pauer, Miss Hünitzsch, Miss Pfennig, Miss Ohlendorf and Miss Thiele-Bode for organizing basically everything. Also, to the staffs of the mechanical workshop specially Mathias and Alex that always built anything I asked for. Without them this experiment would stay on paper. To Kai-Martin Knaak who always patiently answered all my questions regarding to electronics even the very basic ones. To the whole IQ team and the ones I have not put their names here. I thank the SFB 1128 geo-Q for the finance of the experiment and the scientific workshops.

Finally, I want to thank my family specially my parents for always being there for me and supporting me throughout everything. Also, to my friends for making life happy. I want to give a special thank to Mirco Siercke for being a great partner and a wonderful friend, who has always been cheerful in all my decisions in the last seven years. Thanks for all your scientific and non-scientific supports and even reading many parts of this thesis.